

INTERNATIONAL JOURNAL OF MODERN ENGINEERING

The Leading Journal of Engineering, Applied Science and Technology

Industrial

Electronics

Biomedical

Civil

Aerospace

Computer

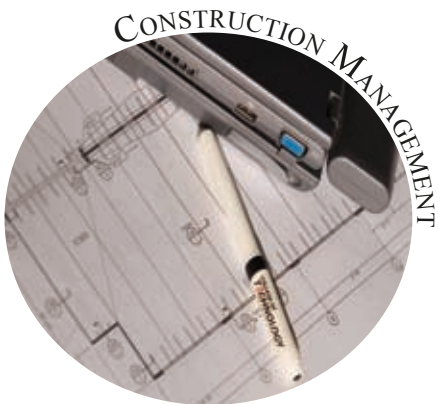
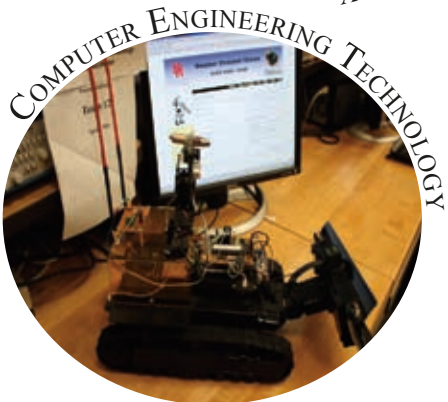
Electrical

Chemical

Mechanical



ENGINEERING



Engineering Technology Opens the Door to a World of Opportunity

We Create Opportunities All Over the World

The University of Houston's College of Technology is leading the future of innovation through the advancements of its Department of Engineering Technology.

- Initiatives including courses in biotechnology and petroleum engineering technology
- In the 2006 ASEE list of 50 schools that offer B.S. degrees in engineering technology, UH ranked 8th in the number of degrees awarded and 5th in the number of degrees awarded to women
- Six state-of-the-art engineering technology research labs including the AT&T Technology Lab
- Exceptional growth in the construction management technology and network communications master's degree programs
- Over \$1M in expenditures from external grants and contracts
- Robotics community outreach via Coordination of Robotics Education (CORE)
- Student internships and other opportunities through the Texas Manufacturing Assistance Center (TMAC)
- Over 750 students and 33 faculty and staff

COLLEGE OF
TECHNOLOGY
University of Houston

www.tech.uh.edu

ENGINEERING TECHNOLOGY / 304 TECHNOLOGY 2 BUILDING / HOUSTON, TX 77204-4021
713-743-4100



UNIVERSITY OF HOUSTON
Learning. Leading.

The University of Houston is an EEO/AA institution.

INTERNATIONAL JOURNAL OF MODERN ENGINEERING

INTERNATIONAL JOURNAL OF MODERN ENGINEERING (IJME) is an independent and nonprofit publication which aims to provide the engineering community with a resource and forum for scholarly expression and reflection.

IJME is published twice annually (Fall and Spring issues) and includes peer-reviewed articles, book and software reviews, editorials, and commentary that contribute to our understanding of the issues, problems, research associated with the engineering and related fields. The journal encourages the submission of manuscripts from private, public, and academic sectors. The views expressed are those of the authors, and do not necessarily reflect the opinions of the IJME or its editors.

EDITORIAL OFFICE:

Mark Rajai, Ph.D.
Editor-In-Chief
Office: (818) 677-2167
Email: ijmeeditor@iajc.org
Dept. of Manufacturing Systems
Engineering & Management
California State University
Northridge
18111 Nordhoff Street
Northridge, CA 91330-8332

THE INTERNATIONAL JOURNAL OF MODERN ENGINEERING EDITORS

Editor-In-Chief:

Mark Rajai

California State University-Northridge

Associate Editors:

Alok Verma

Old Dominion University

Vivay Vaidyanathan

University of North Texas

Production Editor:

Robert Canter

Virginia Tech.

Subscription Editor:

Morteza Sadat-Hossieny

Northern Kentucky University

Financial Editor:

Li Tan

Purdue University North Central

Executive Editor:

Sohail Anwar

Penn State University

Manuscript Editor:

Philip D. Weinsier

Bowling Green State University -Firelands

Copy Editors:

Victor J. Gallardo

University of Houston

Li Tan

Purdue University North Central

Publishers:

Jerry Waite

University of Houston

Hisham Alnajjar

University of Hartford

Web Administrator:

Saeed Namyar

Namyar Computer Solutions

TABLE OF CONTENTS

<i>Editor's Note: IAJC New Journal-The International Journal of Engineering Research and Innovation</i>	3
<i>Mark Rajai, IJME Editor and IAJC President</i>	
<i>A Low-Power Instrumentation and Recording System for Swing Door Usage Analysis</i>	5
<i>Dale H. Litwhiler, Penn State Berks; Thomas H. Gavigan, Penn State Berks</i>	
<i>Biotechnology Gearing Up to Manufacture Biofuels Including Ethanol and Biodiesel</i>	13
<i>Alton L. Kornegay, North Carolina Agricultural & Technical (A&T) State University; Dominick E. Fazarro, Sam Houston State University; David W. Hoffa, Alexandria Technical College</i>	
<i>Design Coordination of Pre-amp EDFAs and PIN Photon Detectors for Use in Optical Telecommunications Receivers</i>	17
<i>Akram Abu-aisheh, University of Hartford; Hisham Alnajjar, University of Hartford</i>	
<i>A Comparative Analysis and Evaluation of Different Approaches of Globalization of Engineering Curriculum in the USA</i>	23
<i>Quamrul H. Mazumder, University of Michigan-Flint</i>	
<i>Active Noise Control Using the Filtered-X RLS Algorithm with Sequential Updates</i>	29
<i>Li Tan, Purdue University North Central; Jean Jiang, Purdue University North Central</i>	
<i>Incorporating System-Level Design Tools into Upper-Level Electrical Engineering Courses</i>	35
<i>Wagdy H Mahmoud, University of the District of Columbia</i>	
<i>Teaching Electromagnetic Fields with Computer Visualization</i>	43
<i>Yeqin Huang, Bill W. Yang, Robert Adams, Brian Howell, James Z. Zhang, and Kenneth Burbank, Western Carolina University</i>	
<i>Application of a Software Configurable Digital Servo Amplifier to an Electric Machine Control Course</i>	49
<i>Shiyong Lee, Pennsylvania State University Berks Campus</i>	
<i>Design and Testing of a Permanent Magnet Axial Flux Wind Power Generator</i>	59
<i>Garrison F. Price, Penn State Altoona; Todd D. Batzel, Penn State Altoona; Mihai Comanescu, Penn State Altoona; Bruce A. Muller, Penn State Altoona</i>	
<i>A Deterministic and Stochastic Model for Production Lot Size as a Function of Storage Cost</i>	67
<i>Ahmad R. Sarfaraz, California State University, Northridge</i>	
<i>Localization of Topographic GPS Surveys with TOPSURV PC (Software Review)</i>	73
<i>Tarig Ali and Ali Mehrabian, University of Central Florida</i>	
<i>Fundamentals of Nanotechnology (Book Review)</i>	75
<i>Sohail Anwar, Pennsylvania State University, Altoona College</i>	
<i>Instructions for Authors</i>	76

EDITOR'S NOTE: IAJC NEW JOURNAL THE INTERNATIONAL JOURNAL OF ENGINEERING RESEARCH AND INNOVATION



Mark Rajai, IJME Editor and IAJC President

IAJC New Journal

The great success of the 2008 IAJC-IJME International Conference and the broad topics of the published articles was the motivation for the International Association of Journals and Conferences (IAJC) to launch its second official and flagship journal to meet the growing demand. The new journal is titled *International Journal of Engineering Research and Innovation (IJERI)*.

The aim of the journal is to emphasize the use of research and innovation in all engineering fields and to strike a balance between research and application as well as decimation of information to both researchers and practitioners. The journal encourages submission of innovative and original articles in all fields of engineering and applied sciences. The new journal follows the same successful platform of its sister journal, IJME.

The *International Journal of Engineering Research & Innovation (IJERI)* is now the official and second flagship journal of the IAJC. IJERI, like IJME, is a highly-selective, peer-reviewed print journal which publishes top-level research work from all areas of engineering research, innovation, and entrepreneurship.

IJERI is steered by IAJC's distinguished board of directors and is supported by an international review board consisting of prominent individuals representing many well-known universities, colleges, and corporations in the United States and abroad.

To maintain a high-quality journal, manuscripts that appear in the IJERI *Articles* section have been subjected to a rigorous review process. This includes blind reviews by three or more members of the international editorial review board, followed by a detailed review by the IJERI editors.

IAJC, the parent organization of IJME and IJERI, is a first-of-its-kind, pioneering organization acting as a global, multilayered umbrella consortium of academic journals, conferences, organizations, and individuals committed to advancing excellence in all aspects of technology-related education.

Current Issue

IJME's current issue includes ten high-quality papers (eight are selected papers from our 2008 conference) and a book review and software review. We hope you enjoy this special issue and continue to support the journal and its parent organization.

A LOW-POWER INSTRUMENTATION AND RECORDING SYSTEM FOR SWING DOOR USAGE ANALYSIS

Dale H. Litwhiler, Penn State Berks; Thomas H. Gavigan, Penn State Berks

Abstract

As part of an energy harvesting investigation, a custom monitoring device was designed, constructed and implemented to measure and record the characteristics of human-operated swing door usage in a typical public building setting. The device was designed to be portable, battery-powered, easily installed without damaging the door, inconspicuous, and non-interfering with normal door operation. The dynamic position of the door is measured and stored in on-board non-volatile memory that is later uploaded for analysis. A real-time clock is used to timestamp each door opening event. The system is easily calibrated when installed on the door. In this paper, the electrical, mechanical, and software designs are presented and discussed. System calibration and resolution is also presented. Data formatting and analysis is described, and experimental results from the system are presented.

Introduction and Motivation

Energy harvesting (which here may also be called *energy scavenging*) is the process of capturing forms of energy that might otherwise be neglected or wasted for the purpose of powering electronic systems such as environmental monitors or other remotely located, mobile and/or wireless systems [1-3]. This type of energy capturing is particularly useful in systems where the power demand or duty ratio is small. Investigations into capturing the energy generated by humans have been presented [4]. Systems that harvest wasted energy expended while walking have been extensively investigated [5,6].

The energy source being studied here is that of humans pushing or pulling open the doors (swing doors) of public buildings. The doors studied are those that are typically found in hallways or building entrances. The doors have a closure mechanism that provides the spring force to close the door as well as some level of damping to limit the opening and closing velocities for safety and to prevent the door from slamming shut. The static and dynamic characteristics of the doors under test have been previously identified [7]. These characteristics are then used together with the long-term monitor data to quantify the energy potential.

In public buildings, the doors can be opened several hundred times each day, thus the potential exists for a significant amount of energy being expended by humans. There are many possible uses for the energy harvested from human powered mechanisms such as doors. Measurement of the door usage characteristics in its natural (non-laboratory) environment is the focus of the system presented here. This information can later be used to evaluate the human energy potential of the door operation.

By using low-power electronic devices and smart power management, a portable battery-operated system to measure the door usage characteristics and patterns can be realized. Custom portable monitoring systems have been used in biomedical applications [8,9]. The hardware and software design considerations for the unique application of monitoring swing door usage are presented and discussed here.

System Design Goals

Although swing doors have a wide range of hinge and closure mechanisms, the instrumentation concepts remain the same. To properly assess the true energy potential of human-operated swing doors, the motion of the door must be monitored over an extended period of time and in a non-intrusive manner. That is, the monitor hardware must not interfere with the operation of the door and must not be so noticeable as to make users avoid opening the door.

Mechanically, the monitor design goals are as follows:

- Easily mounted and removed from door frame or hinge without damage to the structure
- Small enough to be unobvious to door users
- Durable enough for prolonged use (indoor only)
- Position sensing arm shall be self-returning and not interfere with normal door operation
- External serial port connector for easy data access

Electrically, the monitor design goals are as follows:

- Battery powered
- Low power consumption
- Position resolution of 5° or better
- Sample fast enough to provide dynamic position accuracy of 5° or better

- Enough memory to store at least one day's worth of data
- Timestamp door activity
- Serial port for data upload to computer
- Easy calibration
- Adjustable start/stop threshold position

Another design criterion is the ability to sense when the door has been propped open and to stop acquiring data during this condition. Also, the system must not overwrite stored data in the event that the memory becomes full. These requirements are handled in the software of the on-board microcontroller processor and will be discussed later.

Methods and Materials

Hardware

Figure 1 shows the assembly drawing of the door monitor system. The project box contains the circuit board and batteries (3 - AAA size) to power the system. In practice, the project box enclosure is rigidly mounted to the doorframe of the door under test, typically on the hinge hardware, with the fixed and movable clamping bars. Figure 2 shows a photograph of the device mounted to the protruding door hinge hardware with the clamping bars secured with machine screws. Both right hand and left hand swinging doors can be accommodated.

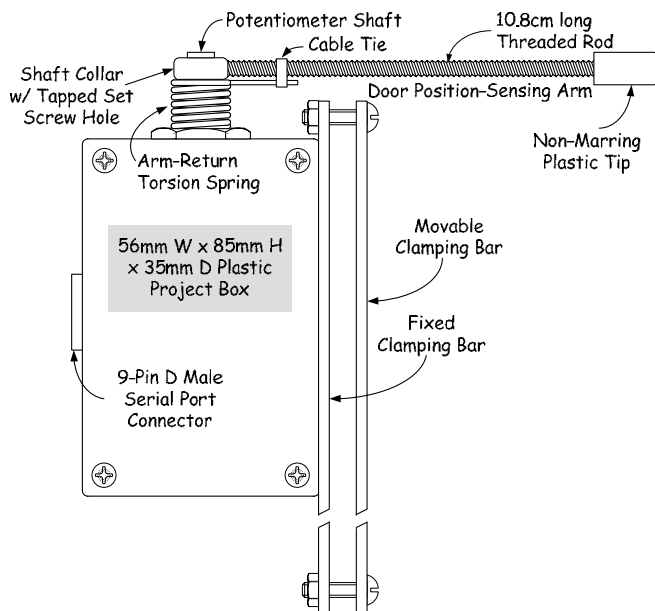


Figure 1. Door monitor assembly drawing

The shaft of the door position - sensing potentiometer extends out of the top of the enclosure. The sensing arm

(threaded rod) is attached using a simple tapped collar as shown in Figure 1. A small torsion spring is used to return the sensing arm and keep it in contact with the swinging door surface. A plastic tip is mounted to the end of the threaded rod to produce a non-marring, low-friction contact area.

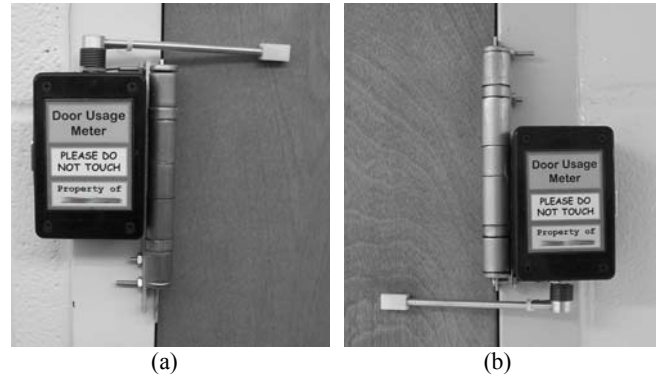


Figure 2. Door monitor system installation on right-hand (a) and left-hand (b) swinging doors

The required length of the position - sensing arm is primarily determined by the desired angular position resolution. Figure 3 shows a top view of the door monitor position sensing components and door hinging configuration. The center of rotation of the potentiometer shaft is not coaxial with the center of rotation for the door. Therefore, the length of the sensing arm is an integral part of the angular position resolution.

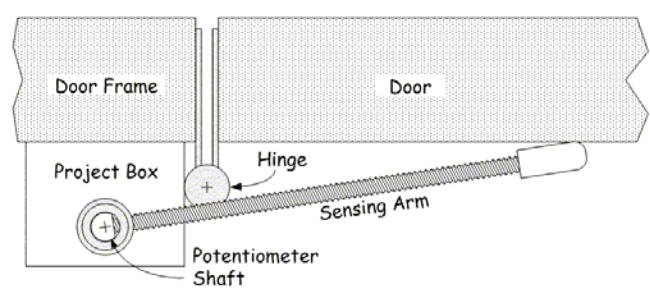


Figure 3. Sensing arm and door position diagram, top view

Because the potentiometer shaft is off-axis with the door rotation axis, its rotation is not linearly related to door rotation. The relationship is however predictable, and through careful design and calibration, the door position can be measured accurately without the need for aligning these axes. This keeps the system flexible for use on many types of door/hinge arrangements.

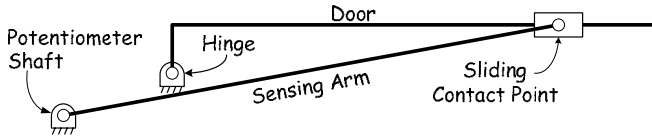


Figure 4. Linkage model of sensing arm and door

The sensing arm arrangement in Figure 3 can be modeled as a linkage system as shown in Figure 4 where the system is shown in its initial position, that is when the door is closed.

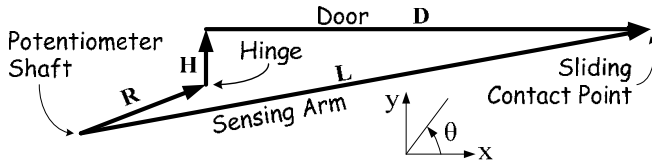


Figure 5. Vector model of sensing arm and door

Figure 5 consists of a vector diagram specifying the positions of the components of the door/potentiometer linkage system given in Figure 4. The vectors are defined as follows:

\mathbf{R} = the position of the door hinge with respect to the potentiometer shaft.

$\mathbf{H} + \mathbf{D}$ = the position of the contact point on the door surface with respect to the door hinge.

\mathbf{L} = the position of the sliding contact point with respect to the potentiometer shaft.

The following vector equation relates the positions of the system components as given in Figure 5.

$$\mathbf{R} + \mathbf{H} + \mathbf{D} = \mathbf{L} \quad (1)$$

By resolving the vectors in (1) into their rectangular or x and y components, the following scalar equations can be written as (2). The angles for each of the components positions given in (2) are measured from the horizontal in a counter-clockwise direction.

$$\begin{aligned} R \cos \theta_R + H \cos \theta_H + D \cos \theta_D &= L \cos \theta_L \\ R \sin \theta_R + H \sin \theta_H + D \sin \theta_D &= L \sin \theta_L \end{aligned} \quad (2)$$

Several of the parameters of (2) are known or are related by constants. The positions of the potentiometer axis and door hinge axis are fixed at installation; therefore, R is known. The distance of the hinge axis from the door surface is also fixed, thus the distance $|\mathbf{H}| = H$ is also known. The hinge plate angle, θ_H , always forms a right angle with the door angle, θ_D , such that $\theta_H = \theta_D + 90^\circ$. Using the trigonometric

identities, $\cos(\theta + 90^\circ) = -\sin(\theta)$ and $\sin(\theta + 90^\circ) = \cos(\theta)$, (2) can now be written as,

$$\begin{aligned} R_x - H \sin \theta_D + D \cos \theta_D &= L \cos \theta_L \\ R_y + H \cos \theta_D + D \sin \theta_D &= L \sin \theta_L \end{aligned} \quad (3)$$

The unknowns in (3) are now D , θ_D , and θ_L . The desired relationship is the angle of the sensing arm, θ_L as a function of the angle of the door, θ_D . By solving each of the component equations for D and setting them equal to each other, a transcendental equation in the desired variables results:

$$\begin{aligned} [L \cos \theta_L - R_x + H \sin \theta_D] \sin \theta_D &= \\ [L \sin \theta_L - R_y - H \cos \theta_D] \cos \theta_D \end{aligned} \quad (4)$$

With the system constructed as shown in Figure 1 and mounted as shown in Figure 2, the known dimensional values are $R_x = 3.97\text{cm}$, $R_y = 0.317\text{cm}$ and $H = 1.75\text{cm}$. Using these values, (4) can be numerically solved for θ_L as a function of θ_D for various sensing arm lengths, L . Figure 6 shows a plot of these functions.

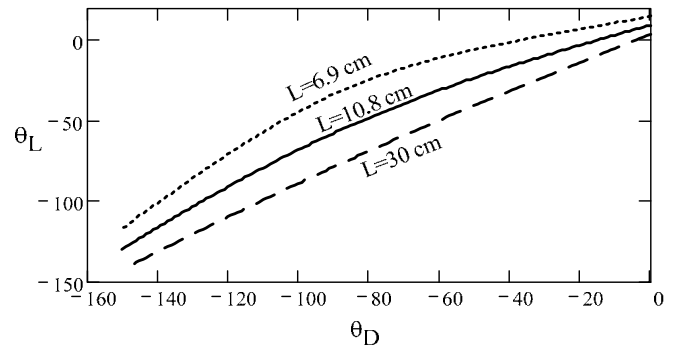


Figure 6. θ_L versus θ_D for various arm lengths, L

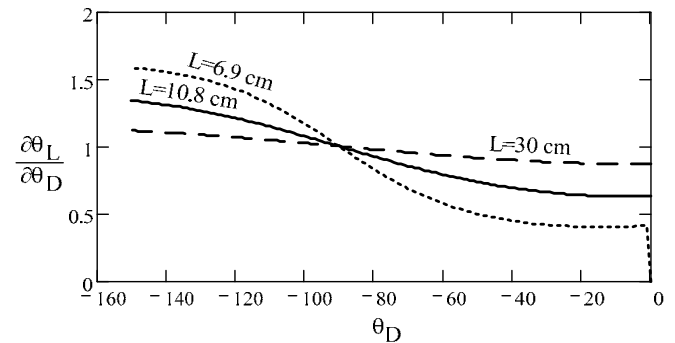


Figure 7. θ_L sensitivity versus θ_D for various arm lengths, L

To determine the resolution of the overall door angle measurement, the static sensitivity of the sensing arm angle, θ_L , to door angle, θ_D , is required. This can again be numeri-

cally determined from the functions plotted in Figure 6. Figure 7 shows the plots of $\partial\theta_1/\partial\theta_D$ for various sensing arm lengths, L . For very long arm lengths, the static sensitivity is nearly unity as expected. As the arm length becomes short, the sensitivity varies greatly from less than one to greater than one over the swing arc of the door. If the arm were made too short it would actually lose contact with the door at some angle. For the configuration used here, this loss of contact occurs for sensing arm lengths less than about 6.9cm.

The transfer function of the potentiometer can be determined using the effective electrical angle of the device. The effective electrical angle of a potentiometer is the angle over which the wiper voltage changes as the shaft is rotated. This angle is usually less than the full range mechanical angle. For the door position sensing potentiometer used here (Bourms part number 81A1AB28B25), the effective electrical angle is 240° while the mechanical range of rotation is 300° . The transfer function is ratiometric with the supply voltage, V_S . The potentiometer wiper voltage, V_w , with respect to circuit ground increases from 0V when $\varphi_E = 0$ to V_S when $\varphi_E = 240^\circ$. The resulting transfer function is then,

$$\frac{V_w}{\varphi_{E \max}} = \frac{V_S}{240^\circ} \text{ Volts/deg} \quad (5)$$

The potentiometer voltage is measured with an 8-bit analog to digital converter. The reference voltage for the A/D is also the potentiometer excitation voltage, V_S , and therefore the measurement is insensitive to changes in this voltage. The resolution for the combined potentiometer and A/D converter is then,

$$\text{Resolution} = \frac{V_S}{2^8} \frac{240^\circ}{V_S} = 0.94 \text{ deg/bit} \quad (6)$$

The overall resolution of the sensing system can now be estimated by combining the resolution of the potentiometer and A/D converter from (6) with the sensitivity of the sensing arm shown in Figure 7. From Figure 7, the minimum resolution occurs with the shortest sensing arm length and for door angles near zero degrees. Here, the sensitivity is approximately $0.4^\circ/\text{deg}$ which results in an overall resolution of $2.34^\circ/\text{bit}$. The design goal was a resolution of $5^\circ/\text{bit}$ and therefore an arm length of 6.9cm would be adequate for the mounting configuration presented. In the application to ensure that the sensing arm remained in contact with the door for several mounting configurations, the slightly longer length of 10.8cm was used. This length resulted in an estimated resolution of $1.51^\circ/\text{bit}$.

The door monitor system need only be active during the time when the door is not in the closed position. Therefore, the system can be placed into a low power sleep mode between door opening events to conserve battery energy. The sleep mode power is primarily that of the system microcontroller. The door position sensing potentiometer wiper voltage level is used to awake (and sleep) the system.

Figure 8 shows the schematic diagram of the door position potentiometer sensing circuit. R1 is the potentiometer that is connected to the door position sensing arm. A large resistance value is required for the potentiometer since it is always connected to the battery regardless of the mode of operation and therefore always consumes energy. A micro-power operational amplifier (U3, OPA347) is then used to buffer the R1 wiper voltage to reduce the source resistance presented to the microcontroller A/D input.

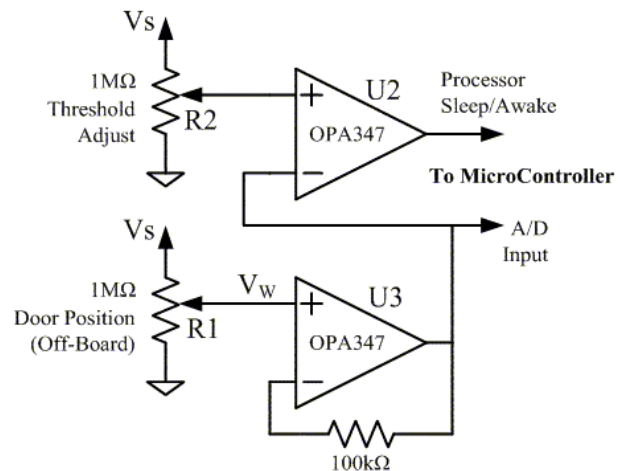


Figure 8. Buffer and comparator circuit schematic

The output of U3 is also sensed by the comparator formed with another micro-power op amp (U2) to create a Sleep/Wakeup signal for the microcontroller, which is ultimately determined by the door position. The Sleep/Awake threshold is set by adjusting the trimmer potentiometer, R2, when the system is installed on the door. The quiescent supply current for U2 and U3 is typically $34\mu\text{A}$ each [10].

When the microcontroller is awake, the microcontroller's A/D converter samples the output of U3 at a rate of 16 samples per second. This sampling rate is a compromise between dynamic resolution and system data storage memory capacity.

The use of several public building doors was observed to obtain an estimate of door opening and closing times. Typically, the doors were pushed or pulled to an open position of roughly 90° in about 2 seconds. The full cycle of door open-

ing by the user and closing by the automatic closer mechanism took approximately 5 seconds.

An average door opening rate of $90^\circ/2s$ requires a minimum sampling rate of 9 samples per second to achieve a dynamic resolution of $5^\circ/\text{bit}$. However, the sensitivity of the

potentiometer angle to door angle must also be included. When the minimum sensitivity of 0.62° for a 10.8cm sensing arm is included, the minimum sampling rate required to achieve a dynamic resolution of $5^\circ/\text{bit}$ is 14.5 samples per second. Thus a slightly higher sampling rate of 16 samples per second is implemented in the system.

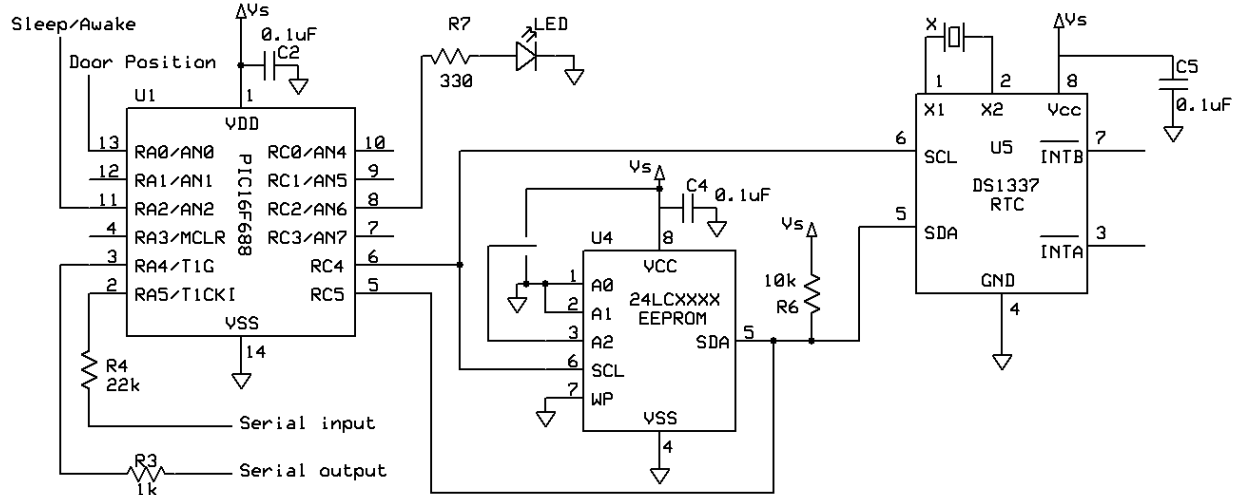


Figure 9. Microcontroller, EEPROM and real-time clock circuit schematic

At a sampling rate of 16 samples per second, a typical door opening and closing event takes 80 samples. Using an 8-bit A/D converter, one byte of memory is required for each sample; therefore, 80 bytes are needed for each event. Door use observations also determined that roughly 500 opening and closing events occurred each day thus requiring approximately 40k bytes of memory capacity. This capacity is obtained by using one 512kbit (64k x 8bit) EEPROM memory device; the 24LC512 manufactured by Microchip Technology, Inc. This device consumes very little power, has a wide operating voltage range and uses an I²C serial interface for data transfer, which is easily implemented with a microcontroller [11].

Figure 9 shows the electrical schematic for the microcontroller, data storage memory (EEPROM) and real-time clock (RTC) circuit of the door monitor system. The RTC, DS1337 manufactured by Maxim Integrated Products, communicates with the microcontroller via the same I²C serial bus used by the EEPROM and has a typical quiescent supply current of 500nA at 4.8V [12]. The RTC is used to provide a data/time stamp for each door opening event.

The PIC16F688 microcontroller manufactured by Microchip Technology, Inc. is used as the controlling processor for the system. This microcontroller contains a multiplexed

A/D converter that is software configurable for up to 10-bits of resolution (only 8-bits are used here). The PIC16F688 consumes very little supply current during operation (typically 0.8mA at 5V), has a very low sleep current level (nominally 3nA at 5V), and has a wide operating voltage range (2V – 5.5V), all of which make it ideal for battery operated equipment [13].

The estimated power budget for the system based on manufacturer supplied data is shown in Table I for both sleep mode and active mode. On the prototype unit at 4.6VDC, the sleep mode current was measured to be 42μADC and the active current was 670μADC.

The power budget numbers are used to determine the battery size and expected lifetime. To satisfy the voltage requirements of the devices with a comfortable margin for battery droop, three alkaline cells are used. This arrangement produces a nominal voltage of 4.5VDC. To avoid special purpose batteries, only readily available standard cells are considered (AAA, AA, C, etc.).

Table 1. System Power Budget

Device	Sleep (μA)	Active (μA)
MicroController (4MHz)	0.003	800
EEPROM	1.0	50*
Real-Time Clock	0.5	150
Op-Amps (Total for 2 devices)	68	68
Potentiometers (Total)	10	10
Totals	79.5	1078

* 5mA write current at 1% duty ratio

The charge required for one day of operation with 500 door openings can be estimated as shown in (7) using the quiescent current values shown in Table 1.

$$\begin{aligned}
 Q_{\text{Active}} &= \left(\frac{500 \text{ openings}}{\text{day}} \right) \left(\frac{5 \text{ s}}{\text{opening}} \right) \left(\frac{1 \text{ h}}{3600 \text{ s}} \right) 1.078 \text{ mA} \\
 &= 0.75 \text{ mAh / day} \\
 Q_{\text{Sleep}} &= \left\{ 24 \text{ h} - \left[\left(\frac{500 \text{ openings}}{\text{day}} \right) \left(\frac{5 \text{ s}}{\text{opening}} \right) \left(\frac{1 \text{ h}}{3600 \text{ s}} \right) \right] \right\} 0.0795 \text{ mA} \\
 &= 1.85 \text{ mAh / day} \\
 Q_{\text{Total}} &= 2.6 \text{ mAh / day}
 \end{aligned} \tag{7}$$

An alkaline (zinc / manganese dioxide) AAA size cell has a nominal charge capacity of 1250mAh for small discharge rates [14]. The system could therefore be powered for approximately 480 days using AAA cells. Three AAA cells connected in series to produce a nominal voltage of 4.5V are used in the door usage measurement system.

Software

The microcontroller software is written using PICBASIC but could be performed in any suitable programming language. Many features have been designed into the software for system calibration, housekeeping (setting RTC, etc.), and downloading of stored data.

The microcontroller starting state is in the sleep mode (low-power standby). In this mode, the system consumes the least battery power. When the door is opened slightly such that the potentiometer wiper voltage, V_w , exceeds the threshold voltage, the microcontroller wakes up and begins executing the active routine.

Once awake, the microcontroller immediately reads the current date and time from the RTC and stores this information in EEPROM. The date and time data is read from the

RTC registers as seven 8-bit bytes in binary coded decimal format [12]. These seven bytes plus a trailing eighth byte set to a value of 255 are written to the EEPROM. The 255-value byte is used as a delimiter to tag each door opening event in memory.

After the RTC data and delimiter values are stored, the microcontroller begins to sample the door position potentiometer voltage at a 16 Hz rate. The voltage is measured using 8-bits of A/D resolution therefore one byte per sample is stored. After each voltage sample, the status of the door is checked to see if the door is still open. If the door is closed, the microcontroller returns to the sleep state.

The measurement system communicates with an external computer via an RS232 serial port. The system responds to serial commands to perform various housekeeping tasks. These tasks include reading the EEPROM data, synchronizing the RTC with the clock of the external computer, and resetting the memory counter to prepare for taking more data. Figure 10 shows the graphical user interface (GUI) of the external computer (handheld) application used to communicate with the measurement system.

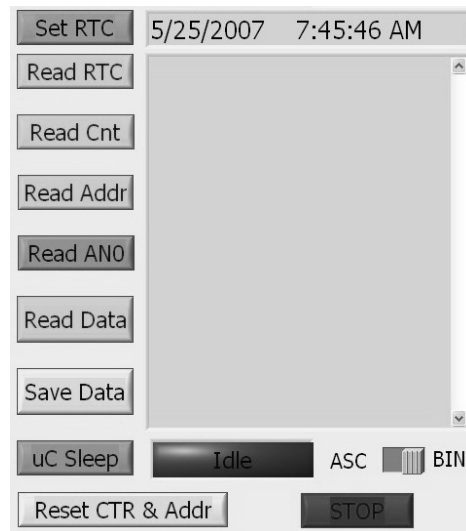


Figure 10. Graphical User Interface for handheld PC

The stored data is transmitted to the external PC via the serial port at 9600 baud in 8N1 format. Each byte of data is sent as an ASCII character, which is then decoded by the external PC software. The ASCII decimal 255 character that was formatted into the last byte of the date/time stamp string serves as the marker to denote the start of each door opening event's data.

System Calibration

The door usage measurement system is calibrated after installation on the door under test. A template is placed on the floor over which the door swings. The template is essentially a large protractor and contains radial lines in 5 degree increments with the origin located directly beneath the door hinge. The measurement system is placed in its normal mode of operation while the door is manually moved through its full range of swing, stopping at each 5 degree mark for a few seconds. The stored data is then downloaded and analyzed to create a table to map the door potentiometer voltage to the position of the door. Voltages between the table values can then be linearly interpolated. Table 2 contains typical calibration data for door positions from -15° (wakeup threshold) to -135° (door stop) in 5° steps.

Table 2. Calibration lookup table data

Door Angle ($^\circ$)	Digital Value	Door Angle ($^\circ$)	Digital Value
-15	42	-80	93
-20	46	-85	98
-25	50	-90	104
-30	53	-95	109
-35	57	-100	114
-40	60	-105	120
-45	64	-110	126
-50	68	-115	133
-55	72	-120	139
-60	76	-125	145
-65	80	-130	151
-70	84	-135	158
-75	89		

Example Results

The calibration data of Table 2 was used together with the spatial orientation of the door position sensing potentiometer, R1, to determine the actual sensing arm angle, θ_L , as a function of door angle, θ_D . These measured values are plotted together with the predicted values (the curve for $L = 10.8\text{cm}$ shown earlier in Figure 6) in Figure 11. The actual values correspond very well with those predicted by (4). Much of the variation in the measured values is due to the quantization error of the A/D converter.

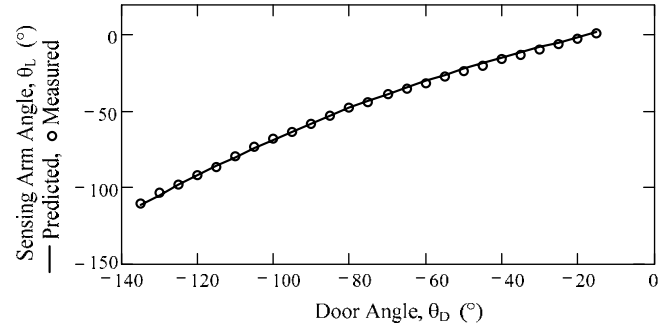


Figure 11. Predicted and measured sensing arm angle as a function of door angle for $L = 10.8\text{cm}$

The door monitor system was mounted to a hallway swing door in a college classroom building as shown in Figure 2. Door usage data was recorded over a period of one week. The recorded data was uploaded to the handheld PC each day. Figure 12 shows a plot of the recorded data for two typical consecutive door opening events. From the recorded data, the door position at any given point can be determined by using the calibration data in Table 2.

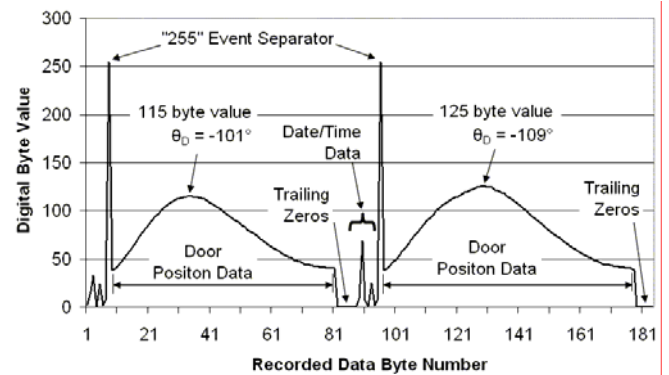


Figure 12. Plot of recorded door usage data for two consecutive door opening events

From Figure 12 it can be seen that the door was opened to positions of -101° and -109° on the two consecutive openings. In each opening, the user pushed or pulled the door to its respective maximum position in 1.6s and 2.0s. The door closer mechanism returned the door to the closed position with a damped, tapered velocity motion to prevent slamming.

The date/timestamp information for each door opening event is also useful in energy harvesting applications. Figure 13 shows a histogram for door openings over a typical 24 hour period. This data shows the hours over which the majority of the energy is produced by the users. Such data is also useful for other applications such as maintenance and room/building use scheduling and planning.

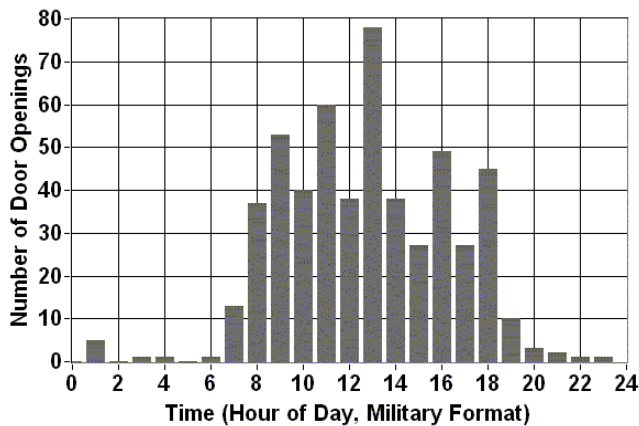


Figure 13. Histogram of door opening events for one day

Conclusions

A low-power system for measuring and recording the usage of a swing door was designed, constructed, calibrated, and implemented. The system electrical and mechanical design goals were achieved through careful analysis and software design as presented and discussed. The design is simple, effective and flexible, yet meets the stringent performance requirements. System installation and calibration can easily be performed on many door hinge arrangements. The door monitor system, together with the door/closer mechanism characterization data, allows the stored energy at any door position to be determined. This stored energy, which is generated by human users, can then be quantified without special loading or testing of the human subjects.

References

- [1] Ottman, G.K., Hoffmann, H.F., Bhatt, A.C., and Lesieutre, G.A., Adaptive piezoelectric energy harvesting circuit for wireless remote power supply. *IEEE Trans. Power Electron.*, vol. 17, no. 5, pp. 669-676, Sep. 2002.
- [2] Paradiso, J.A. and Starner, T., Energy Scavenging for Mobile and Wireless Electronics. *IEEE Pervasive Computing*, Vol. 4, No. 1, February 2005, pp. 18-27.
- [3] Poulin, G., Sarraute, E., and Costa, F., Generation of electrical energy for portable devices: Comparative study of an electromagnetic and a piezoelectric system. *Sens. Actuators A*, vol.116, pp.461-471, 2004.
- [4] Paradiso, J.A., Systems for Human-Powered Mobile Computing. *Proc. of the IEEE Design Automation Conference (DAC2006)*, San Francisco, CA, July 24-26, 2006, pp. 645-650.

- [5] Shenck, N.S. and Paradiso, J.A., Energy Scavenging with Shoe-Mounted Piezoelectrics. *IEEE Micro*, Vol. 21, No. 3, May-June 2001, pp. 30-42.
- [6] Kymisis, J, Kendall, C., Paradiso, J., and Gershenfeld, N., Parasitic Power Harvesting in Shoes. *Proc. of the Second IEEE International Conference on Wearable Computing, (ISWC)*, IEEE Computer Society Press, pp. 132-139, October 1998.
- [7] Litwhiler, D. H. and Gavigan, T. H., "Energy Harvesting: Measurement and Analysis of Swing Doors," *Journal of Engineering Technology*, Vol. 25, No. 2, Fall 2008, pp 26-31.
- [8] Cifrek, M., Mrvos, S., and Zufic, P., Portable Data Logging System for Long-Term Continuous Monitoring of Biomedical Signals. *Proc. of IEEE MELECON 2004*, May 12-15, 2004.
- [9] Luharuka, R., Gao, G., and Krishnamurty, S., Design and Realization of a Portable Data Logger for Physiological Sensing. *IEEE Trans. Instrum. Meas.*, vol. 52, no. 4, 2003.
- [10] Texas Instruments/Burr-Brown datasheet for OPA347 <http://focus.ti.com/docs/prod/folders/print/opa347.html>.
- [11] Microchip datasheet for 24LC512 <http://www.microchip.com>.
- [12] Maxim datasheet for DS1337 <http://www.maxim-ic.com>.
- [13] Microchip datasheet for PIC16F688 <http://www.microchip.com>.
- [14] Eveready Energizer battery datasheet <http://data.energizer.com/PDFs/E92.pdf>.

Biographies

DALE H. LITWHILER is an Associate Professor at Penn State, Berks Campus in Reading, PA. He received his B.S. from Penn State University (1984), his M.S. from Syracuse University (1989) and his Ph.D. from Lehigh University (2000) all in electrical engineering. Prior to beginning his academic career in 2002, he worked with IBM Federal Systems and Lockheed Martin Commercial Space Systems as a hardware and software design engineer. Dr. Litwhiler may be reached at dale.litwhiler@psu.edu

THOMAS H. GAVIGAN is an Assistant Professor at Penn State, Berks Campus in Reading, PA. He received his B.S. in Mechanical Engineering from Drexel University in 1970 and his M.S. in Engineering Mechanics from Penn State in 1977. Mr. Gavigan teaches in the areas of Engineering Mechanics and Engineering Design. Professor Gavigan may be reached at thg2@psu.edu

BIOTECHNOLOGY GEARING UP TO MANUFACTURE BIOFUELS INCLUDING ETHANOL AND BIODIESEL

Alton L. Kornegay, North Carolina Agricultural & Technical (A&T) State University;
Dominick E. Fazarro, Sam Houston State University; David W. Hoffa, Alexandria Technical College

Abstract

With global demands recently causing United States (U.S.) gasoline prices to exceed \$4.00 per gallon, and the average price of diesel fuel to sell at approximately \$4.70 per gallon, renewable alternative auto fuels, or biofuels, have not only become feasible but desirable. The “corn rush” is creating a tremendous shortage of trained factory workers to convert natural resources into usable fuels. The Apollo Alliance and the Urban Habitat Institute have reported that “an average ethanol plant produces about 40 million gallons of ethanol a year and employs around 35 people in the following types of jobs: general manager, plant manager, maintenance supervisor, plant operators, purchasing manager, lab manager and technicians, craftsmen, laborers, and instrument technicians. Biodiesel plants employ fewer people; around 28 workers for an average plant making 30 million gallons per year” [1]. The purpose of this paper is to propose a solution to the biofuel personnel education shortage problem. Designed primarily by collaboration between four departments in the School of Technology at North Carolina Agricultural and Technical (A&T) State University and various other disciplines across the campus, this paper describes an interdisciplinary-designed master’s degree program in biotechnology geared specifically toward the needs of the technologists, managers, and laborers employed in biofuel manufacturing plants.

Introduction

A graduate program is being designed by collaborative efforts of a blue-ribbon focus group. The proposed curriculum provides three integrated segments of potential trainees: traditional four-year higher education students, community college transfer students, and displaced factory workers. As part of curriculum development two members of the focus group attended a seminar sponsored by the North Carolina Community College Systems (NCCCS). “College that really works” is the motto of NCCCS, the state’s 58-campus community college system [2]. The BioNetwork, which began in 2004, is a system of community colleges that banded together and formed NCCCS BioNetwork, a statewide initiative that connects community colleges across North Carolina, providing specialized training, curricula and equipment to develop a world-class workforce for the biotechnology, pharmaceutical, and life sciences industries. Our purpose for

attending these seminars is to gain further insight into the NCCCS’ biotechnology system to aid our initiative to develop an interdisciplinary biotechnology graduate degree program at North Carolina A&T State University.

Industry and Academia Collaboration

To meet U. S. demand, major oil companies say that easily attainable global oil supplies are nearing exhaustion, forcing them to explore drilling deeper or drilling in areas that have been termed ecologically off limits, i.e., the Arctic National Wildlife Refuge (ANWR). Environmentally, the Environmental Protection Agency (EPA) has declared methyl tertiary butyl ether (MTBE), which was touted by industry experts earlier, to be unsafe because of its propensity to contaminate underground water [3]. Corn, soybeans, sugar cane, switch grass, wood, crop residue, and other renewable biological energy products have now become viable alternative fuel sources. Together, these and other factors open the door for ethanol, biodiesel, and other renewable fuels to become part of America’s alternative fuels of choice. This paper uses the collaboration between Columbia Basin College, Washington State University Extension, and Port of Walla Walla as an example to demonstrate how three entities successfully collaborated to build and staff a biofuels manufacturing facility. When this graduate project is complete, it will provide tremendous insight into how academia and industries collaborate to maximize the potential of both entities.



Figure 1. Bio-Diesel Project Walla Walla County, Washington (2006)

Quick Facts

- \$40 million investment.
- 100K metric tons or 31million gallons of biodiesel annually.
- 20 FTE—Average wage \$40K+ benefits.
- 2003: The Washington State Legislature approved legislation that provides biodiesel plants with a six-year property tax exemption, sales tax exemption for equipment and new construction, and reduction in the Business and Occupation (B&O) tax rate.

Quick Facts

- \$150 million Investment.
- 100 million gallons of ethanol annually.
- 35–50 FTE—Average wage \$35K+ benefits.
- 2003: The Washington State Legislature approved legislation that provides biodiesel plants with a six-year property tax exemption, sales tax exemption for equipment and new construction, and reduction in the B&O tax rate.

The Program Kickoff

This program started with an interdisciplinary meeting of various departments from across the university campus. Personnel as diverse as the chairpersons from the nursing department and the department of agriculture to engineering and technology faculty, as well as undergraduate and graduate students in the school of technology were all present to kick off the collaborative degree effort. Agricultural engineering made it clear that they were not interested in manufacturing biofuels. The nursing department asserted that there is definitely a divide between safety and first-aid. Undergraduate and graduate students wanted to be included in the research arm of biotechnology.

Program Coordination with the Companies

Even though the committee is currently identifying private companies with which it plans to collaborate and coordinate the master's degree curriculum, thus far no biofuel manufacturing companies have been contacted. Several community colleges and biodiesel companies were present at the April 2008 biodiesel seminar in Clayton, NC. Several of the community colleges were receptive to an articulated degree program with North Carolina A&T State University in the biodiesel program. Several companies expressed interest in working with North Carolina A&T State University to develop curriculum, as well as in hiring graduates of the biotechnology master's degree program.

Table 1: Curriculum Content Courses for the Masters of Biotechnology Program

<u>MANUFACTURING SYSTEMS</u>
Introduction to Manufacturing Processes (3)
Industrial Materials and Processes (3)
Introduction to PLC and Robotics (3)
Manufacturing Planning and Management (3)
Statistical Processes/Quality Control (3)
Production and Control (3)
Six Sigma (3)
Lean Manufacturing (3)
Problem Solving in Industrial Technology (3)
Concepts of Technological Innovation (3)
Leadership Development Seminar (3)
Manufacturing Organization and Management (3)
Statistical Research in Industrial Technology (3)
Industrial Productivity and Management (3)
Strategic Concepts in Quality (3)
Advance Automation and Control (3)
Advanced Manufacturing Processes/CNC (3)
Applied Computer Integrated Manufacturing (3)

The Collaboration on the Final Projects

Collaboration on the final projects will involve input from biofuel industry experts not only from across North Carolina but the U.S. and around the world. The program at North Carolina A&T State University will be a premier program, using the most current ideology and cutting edge technology.

The School of Technology's contribution:

- A Master of Biotechnology degree program, identifying course curriculum, scheduling, and all requirements toward receiving a master's degree from the School of Technology.
- The school would provide core courses in each discipline, much as it already does for other undergraduate and graduate programs.

- The degree curriculum would be designed so new freshmen, community college transfer students, and displaced factory workers could join the program at any time.
- Third and fourth year lectures and labs would be conducted at community colleges of choice. Curriculum would be designed by North Carolina A & T State University.
- All classes would be coordinated from the North Carolina A&T State University campus. Community college classes would be conducted at the partnering institutions. Displaced workers could attend the first four years of classes at the community college or in another discipline at North Carolina A&T State University. After the first two years, the remainder of the degree would be completed as a part of North Carolina A&T State University.
- The department would allow students to base their class projects on projects that they are involved in at their current companies. Departmental class projects would need to be related to the biofuel manufacturing initiative. However, they could be work related if they meet the above criteria and are approved by departmental faculty.

The Manufacturing System Department’s contribution:

- This department would house the Master of Biotechnology degree.
- The Manufacturing Systems department would provide access to faculty and students working on projects, completing class projects, or for the student’s final project to participating community colleges and companies.
- The department, along with the School of Technology, would also raise money to build a traveling operations display model for conferences and seminars at various sites. This joint association would raise money to build a stationary working model on the North Carolina A&T State University campus, which would actually manufacture fuel to help supply fuel needs for the campus motor fleet.

Summary

The impending global crisis created by depleting energy supplies and petroleum reserves has enlarged the market for renewable energy. Converting biological matter to much needed energy requires a workforce trained in biotechnology. The Biotechnology master’s degree program at North Carolina A&T State University is expected to educate potential biofuel industry employees who are able to step into all roles of biofuel manufacturing processes with minimal on-

the-job training, while bringing immediate substantial contributions to the biofuels manufacturing industry. All of this helps reduce America’s dependence on foreign oil and provides a much needed boost for American manufacturing work forces. “What started out to be a large ethanol producing plant in Aurora, NC, recently became a huge ethanol producing plant with the announcement that the facility will be doubled in size from 54 million gallons per year to 108 million gallons per year” [4].



Figure 2: North Carolina corn

Table 2: List of Various Projects at Different Companies and Universities

1.	“Biotech Develops Formula That Nurtures Job Growth,” BusinessNC.com.
2.	“Community Jobs in the Green Environment,” Apollo Alliance and Urban Habitat.
3.	“Biofuels Summit I,” Columbia Basin College, Port of Walla Walla, Washington.
4.	“Building an Innovation Economy,” The University of Rhode Island.
5.	“Industrial Biotechnology and the Future of Ethanol Production,” Biotechnology Industry Organization, Washington, D.C.
6.	“North Carolina Ethanol Plant Creates New Market for Corn,” Southeast Farm Press, North Carolina.
7.	“Switchgrass Profile,” Iowa State University, Iowa.
8.	“One-Step for American Biodiesel, Inc. DBA Community Fuels,” State of California.
9.	“O.H. Kruse Family Makes \$2 Million Commitment to Kansas State University Pilot Feed Mill,” Kansas.
10.	“Biotechnology Curriculum Units,” Iowa State University, Iowa.
11.	“Is Indiana Ready to Be an Emerging Leader in the Biofuels Industry?” Indiana.
12.	“ Using All the Corn and Making Ethanol ,” Iowa.
13.	“Mercedes Wants to Eliminate Petroleum from its Lineup by 2015,” Germany.
14.	“Research into Desert Plant Could Help Development of Energy Crops for Arid Regions,” Liverpool, UK.
15.	“Biodiesel Products,” Extreme Biodiesel-Corona, CA.
16.	“Biofuels for Oregon,” Oregon.

References

- [1] Apollo Alliance and Urban Habitat, "Community Jobs in the Green Economy," 2007.
- [2] North Carolina Community College System, "Preparing North Carolina's World-Class Workforce - Celebrating 40 years of "College That Really Works" for North Carolina," <http://198.85.71.234/alsbrookls/itn160/ncccs/ncccs2.html>, September 7, 2008.
- [3] "Methyl Tertiary Butyl Ether (MTBE): Overview," *MTBE in Fuels*, <http://www.epa.gov/MTBE/faq.htm>, September 7, 2008.
- [4] Roberson, R., "North Carolina Ethanol Plant Creates New Market for Corn," *Southeast Farm Press*, June 13, 2006, <http://southeastfarmpress.com/news/061306-Aurora-ethanol/>, June 16, 2008.

(ACTE). He is the President-Elect of the Industry Division of the ATMAE, formerly NAIT. Dr. Fazarro may be reached at df003@shsu.edu

DAVID HOFFA is an Automation Specialist in the Customized Training Center at Alexandria Technical College in Alexandria, MN. His industrial automation interests are in the areas of robot and PLC installation, programming, cost justification; and troubleshooting, system design, sensor utilization, and systems integration. He is the recipient of the 2005 NAIT Foundation Dr. Clois E. Kicklighter Doctoral Student Scholarship Award. He is the President of the Industry Division of ATMAE, formerly NAIT. Dr. Hoffa may be reached at davidh@alextech.edu

Acknowledgments

The authors are thankful to IJME Journal for the support to develop this document.

Biographies

ALTON KORNEGAY is an assistant professor in the Manufacturing Systems Department, School of Technology at North Carolina Agricultural & Technical (A&T) State University. He instructs undergraduate and graduate manufacturing systems courses and performs research in integrated manufacturing systems and biomanufacturing. Dr. Kornegay brings to the academy four years of military avionics technician experience and more than 30 years of manufacturing work experience in corporate America. After retirement from the John Deere Corporation, he embarked on a career in higher education. Dr. Kornegay is a Certified Senior Industrial Technologist (CSIT) in the Association of Technology, Management, and Applied Engineering (ATMAE), formerly the National Association of Industrial Technology (NAIT). He is the immediate national Past President of the Industry Division of NAIT. Dr. Kornegay may be reached at alkorneg@ncat.edu

DOMINICK FAZARRO is an associate professor in the Department of Agricultural and Industrial Sciences at Sam Houston State University. His interests are learning styles and nanotechnology/nanosafety as they apply to workforce education and development. He received the 2004 and 2007 Service Award in the Technology Education Division/Association for Career and Technical Education

DESIGN COORDINATION OF PRE-AMP EDFAS AND PIN PHOTON DETECTORS FOR USE IN OPTICAL TELECOMMUNICATIONS RECEIVERS

Akram Abu-aisheh, University of Hartford; Hisham Alnajjar, University of Hartford

Abstract

The pre-amp Erbium-Doped Fiber Amplifier (EDFA) is becoming an integral part of optical receivers, and consequently, pre-amp performance is interrelated to the performance of the receiver photon detector. For optimal optical receiver transmission performance, the pre-amp EDFA design must be coordinated with the photon detector design in order to minimize amplified spontaneous emission (ASE) noise mitigation from the pre-amp EDFA to the photon detector. The EDFA output power and laser pump power should be fine-tuned at the optical receiver level to determine the best output power/laser pump power combination to minimize ASE noise at the output of the pre-amp EDFA.

In this work, the pre-amp EDFA noise performance was characterized first at the pre-amp level through modeling, using computer simulations. Then, pre-amp noise performance was characterized experimentally at the optical receiver level. The experimental work focused on the pre-amp EDFA noise performance characterization and analysis at the optical receiver level. This is the ultimate performance characterization method for the EDFA, and it was performed through testing the optical receiver transmission performance under different pre-amp EDFA operating conditions.

Introduction

Pre-amp Erbium-Doped Fiber Amplifiers (EDFAs) are becoming integral parts of long-haul telecommunication optical receivers, and pre-amp EDFA performance is becoming a main factor influencing optical receiver photon detector performance. Based on that fact, the pre-amp EDFA design needs to be coordinated with the photon detector design and the optical receiver design in order to reduce amplified spontaneous emission and improve the optical receiver transmission performance. Pre-amp EDFA laser pump power needs to be optimized first at the pre-amp EDFA design level. This can be done using computer simulation. Then, pre-amp EDFA output power should be fine-tuned at the optical receiver level to achieve the best output power/laser pump power to minimize ASE at the output of the pre-amp EDFA.

Optical receiver transmission performance, commonly known as bit error rate (BER), is the gauge by which optical receivers are characterized. It is used to characterize the ability of the receiver to perform up to the transmission performance specifications when operating under the same conditions as the operating conditions present in the field. In this paper, the test results of pre-amp-based optical receiver transmission performance are measured at different pre-amp EDFA operating conditions. The effects of the optical amplification in the pre-amp EDFA as a function of the pre-amp input power, output power, and input signal to noise ratio on the optical receiver transmission performance were analyzed to characterize the optical receiver transmission performance as related to the EDFA operating conditions. Since the most important factor in pre-amp performance is how well it performs in the optical receiver, optical receiver optimal transmission performance analysis under different operating conditions is the ultimate method for optimizing pre-amp EDFA performance in the optical receiver. The EDFA design needs to be optimized at two levels: the pre-amp/photon detector subsystem level and the optical receiver level.

At the optical receiver level, several characterization experiments need to be performed to analyze the effects of changing pre-amp operating conditions on optical receiver transmission performance. Then, the effects of changing the pre-amp output power setting on optical receiver transmission performance need to be analyzed in order to characterize optical receiver transmission performance.

Noise in Erbium-Doped Fiber Amplifiers

The generation of noise in doped optical pre-amplifiers is an effect of the spontaneous de-excitation of laser ions. As the electrons have a finite excited state lifetime, some of the electrons return spontaneously to the ground state, emitting a photon. This photon has no coherence characteristics with respect to the incoming light signal, as opposed to a photon generated by stimulated emission. The collection of such spontaneously generated photons, being multiplied by the fiber amplifier, forms a background noise. This background noise is known as amplified spontaneous emission, and it is the dominant noise element in pre-amp EDFAs. The optical

noise elements of a pre-amp EDFA at different input power, output power, and different signal wavelengths, and their effects on the EDFA transmission performance can be analyzed by evaluating the contributions of the EDFA ASE noise generated in the process of signal amplification. The noise instability issues that result from ASE were analyzed by different researchers [1].

Pre-amp EDFA operation is based on stimulated emission of optically pumped Er +3 ions in silica. Erbium atomic structure and the 3-level atomic level rate equations for the case of a single-stage 980 nm pumped EDFA were analyzed to help characterize the pre-amp ASE noise. The most fundamental limitation to the gain of an erbium-doped fiber amplifier is the energy conservation principle. This principle can be expressed in terms of the photon flux. The photon flux of the output signal cannot exceed the photon flux of the input signal plus the laser pump photon flux [2]. Since modern receivers use a narrow optical band pass filter at the output of their pre-amp EDFAs, the pump shot noise is filtered in this filter. So pump noise does not play a factor in the pre-amp EDFA transmission performance; however, the pump power affects transmission performance from its contribution to ASE. The most basic treatment of erbium-doped fiber amplifier noise can be performed by analyzing a 3-level erbium atomic system. So the erbium atomic structure needs to be understood to analyze pre-amp noise.

Amplified and Stimulated Emission Analysis at the Erbium Atomic level

Erbium atomic structure has three energy levels that are of interest for the study of its amplification characteristic for communication use. In the 3-level erbium atomic structure, population inversion can be achieved using laser pumping at 980 nm to excite electrons to the upper erbium atomic state. When excited to the upper state, electrons rapidly decay non-radioactively to the meta-stable state. If electrons in the meta-stable state are not stimulated within the electron lifetime in that state, electron transition to the lower states results in spontaneous emission. Spontaneous emission is a random emission that introduces noise. The behavior of this erbium-doped fiber atomic structure is described in the following level rate equations [3]:

$$\frac{dN_3}{dt} = -\frac{N_3}{\tau_{32}} + (N_1 - N_3) * \sigma_p * S_p \quad (1)$$

$$\frac{dN_2}{dt} = -\frac{N_2}{\tau_{21}} + \frac{N_3}{\tau_{32}} - (N_2 - N_1) * \sigma_s * S_s \quad (2)$$

$$\frac{dN_1}{dt} = \frac{N_2}{\tau_{21}} - (N_1 - N_3) * \sigma_p * S_p + (N_2 - N_1) * \sigma_s * S_s \quad (3)$$

Here, N is the population density at the given level [1/cm³], S is the photon flux [1/cm² * s], τ is the spontaneous lifetime [s], and σ is the transition cross section [cm²]. The first equation describes the population change rate for the upper state, the second equation describes the population change rate for the meta-stable state, and the third equation describes the population change rate for the ground state. The steady state atomic populations N1 and N2 are functions of the pumping rate, which represents the pump absorption rate between levels 1 and 3 and of the absorption and stimulated emission rates between levels 1 and 2. When laser radiation interacts with a photon in the lower energy level, the photon is transformed into the upper atomic level. If a photon in the excited state is not stimulated within the 10ms lifetime of the excited state, it will spontaneously decay to the ground state, producing ASE. When this photon travels through the erbium-doped fiber, it gets amplified, resulting in amplified spontaneous emission. All the excited electrons can spontaneously relax from the upper state to the ground state by emitting a photon that is unrelated to the signal photons. This spontaneously emitted photon can be amplified as it travels down the fiber and stimulates the emission of more photons from excited electrons. Amplified spontaneous emission can occur at any frequency within the fluorescence spectrum of the amplifier transitions.

The dominant noise source in any EDFA is ASE. This spontaneous emission reduces the amplifier gain by consuming the photons that would otherwise be used for stimulated emission of the input signal. In order to minimize ASE noise, the pump power should be just enough to achieve population inversion. Population inversion can be achieved when the population in the excited state, N2, is greater than the population in the ground state, N1. The threshold power of the pump required to achieve population inversion can be obtained by setting the rate equation of level 2 to level 0 and setting N1 to be equal to N2.

EDFA Design Optimization Using Computer Simulations

Testing and computer simulation were used to characterize a 980-nm pumped single-stage C-Band pre-amp EDFA for optimization, and the total ASE and optical noise figure (NF) were used for the pre-amp noise characterization. The modeling of amplified spontaneous emission for the computer simulation here is done by treating amplified sponta-

neous emission as an extra signal with a bandwidth corresponding to an effective bandwidth of the entire transition. Bray has experimentally used this method to test for noise figure spectra using ASE sources [4] and [5]. The noise figure defined here is the optical noise figure, and it is calculated by adding an ASE wave at the signal wavelength. So the optical noise figure at the signal wavelength calculated in these simulations is

$$NF(dB) = 10 \log_{10} \left[\left(\frac{P_{ASE}}{h\nu\Delta\nu} + 1 \right) \left(\frac{P_{sig-out}}{P_{sig-in}} \right) \right] \quad (4)$$

Where $P_{sig-out}$ is the output power in mw in the ASE wave, P_{sig-in} is the amplifier input optical powers in mw, $P_{sig-out}$ is the amplifier output optical powers in mw, and $\Delta\nu$ is the spectral band width represented by the ASE wave. At the pre-amp level optimization of pre-amp EDFA performance, the pre-amp input power, output power, and operating wavelength should be taken into account. This allows designers to choose the right erbium-doped fiber length and pump power combination, which helps minimize the amplified spontaneous emission at the output of the pre-amp EDFA.

In modeling pre-amp performance, one needs to analyze the pre-amp noise characteristics. Zhang presented an erbium-doped fiber amplifier model [6]. The parameters of the main components affecting the pre-amp performance were given by Desurvire [2]. These parameters are the erbium concentration and the doped fiber length, the pump wavelength and absorption band, the input signal power and wavelength, and the wave guide characteristics.

Computer simulations of the pre-amp noise figure and ASE at different pump power levels are given in Figures 1 and 2. The EDFA gains progress through the erbium-doped fiber and is characterized by analyzing the gain of both the pump power and the signal power through the fiber.

The small signal gain through the erbium-doped fiber can be analyzed using the erbium atomic structure rate equations. Becker has derived the equations for the signal and pump intensities through the erbium-doped fiber [4].

The change in the signal flux through the erbium-doped fiber is given by the meta-stable state rate equation

$$\frac{d\phi_s}{dz} = (N_2 - N_1) * \sigma_s * \phi_s \quad (5)$$

From the above equation, we can obtain the signal and the pump intensity through the erbium-doped fiber. Computer simulation uses these equations to calculate noise figure

through the erbium-doped fiber. Computer simulation helps in optimizing the erbium-doped fiber length to obtain the best design that minimizes the amplified spontaneous emission at the end of the erbium-doped fiber.

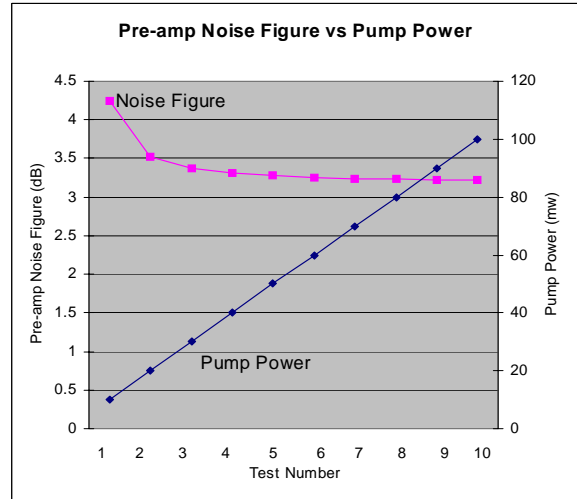


Figure 1: Pre-amp noise figure as a function of the pump power

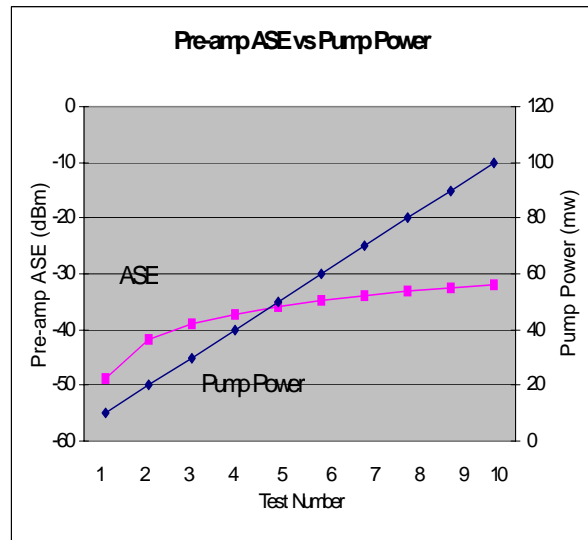


Figure 2: Pre-amp ASE as a function of the pump power

Optical receiver transmission performance analysis under different operating conditions was used to characterize the pre-amp noise performance. The pre-amp EDFA design needs to be optimized at the two levels, and the pre-amp performance should be determined by how well the pre-amp performs in the optical receiver.

Pre-Amp EDFAs and PIN Photon Detectors Design Coordination

The pre-amp EDFA design needs to be optimized at the pre-amp level and the optical receiver level. For optimal optical receiver transmission performance, the pre-amp EDFA design must be coordinated with the photon detector design in order to minimize amplified spontaneous emission noise mitigation from the pre-amp EDFA to the photon detector and the photon detector signal-spontaneous beat noise. The pre-amp input power, output power, and operating wavelength should be taken into account during those tests. This allows designers to choose the right erbium-doped fiber length and pump power combination, and it also helps in minimizing amplified spontaneous emission at the output of the pre-amp EDFA.

Pre-amp performance is measured by how well it performs in the optical receiver, so optical receiver optimal transmission performance analysis under different operating conditions is the ultimate method for optimizing pre-amp EDFA performance in the optical receiver. The EDFA-photon detector subsystem design needs to be optimized at two levels: the pre-amp/photon detector subsystem level and the optical receiver level.

Characterization and Optimization at the Optical Receiver Level

Several studies were performed to improve the transmission performance of long-haul optical receivers [7 and 8]. Since optical receiver transmission performance is the gauge by which optical receivers are characterized, BER was used in the experimental work presented here to characterize the ability of optical receivers to perform up to the transmission performance specifications under the same test conditions as those where the receiver operates in the field [5]. The setup of Figure 3 was used to perform the optical receiver tests analyzed in this paper. This setup gives users the ability and flexibility to perform optical receiver transmission performance measurement, optical input and output measurements, optical signal and noise control, and optical input SNR control [5].

In this work, several characterization experiments were performed to analyze the effects of changing the pre-amp EDFA operating conditions on the optical receiver transmission performance. Testing the pre-amp-based optical receiver at a fixed signal-to-noise ratio at 1550 nm operating

wavelength, the transmission performance was recorded at different pre-amp input/output combinations. A graphical representation of the optical system transmission performance results after normalizing BER is given in Figure 4.

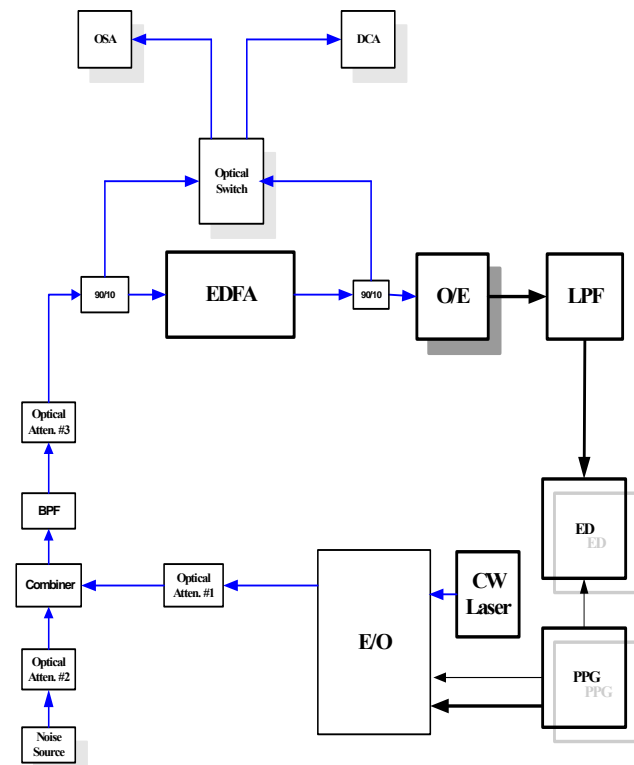


Figure 3: Optical receiver transmission performance test set-up

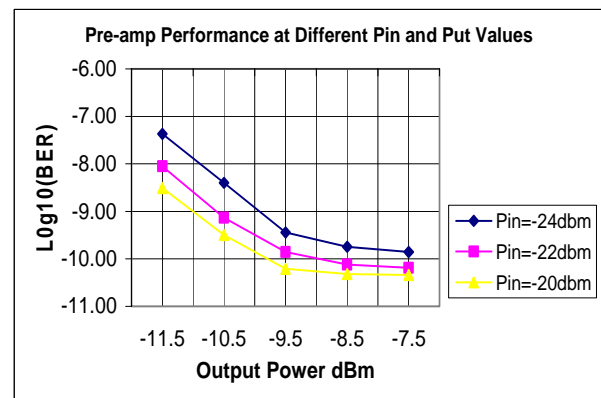


Figure 4: Optical receiver performance change at different input and output power levels

From the results in Figure 4, we see that the optical receiver transmission performance improves as the pre-amp output power is increased. This improvement is due to the fact that more output power requires more pump output, and

more output power excites more electrons to the upper state. This excitation will result in the population inversion that is needed for the amplification process.

When testing the pre-amp-based optical receiver at different input powers and at different signal to noise ratios at fixed output power, the transmission performance changes due to the changes in the operating conditions were monitored. A graphical representation of the system transmission performance, after normalizing BER, is given in Figure 5.

At the atomic structure level, an increase in the input power causes more stimulated emission of the excited electrons. This leaves fewer electrons to move to the ground state spontaneously which means that the pre-amp is generating less amplified spontaneous emission, and that reduces the signal spontaneous noise in the photon detector.

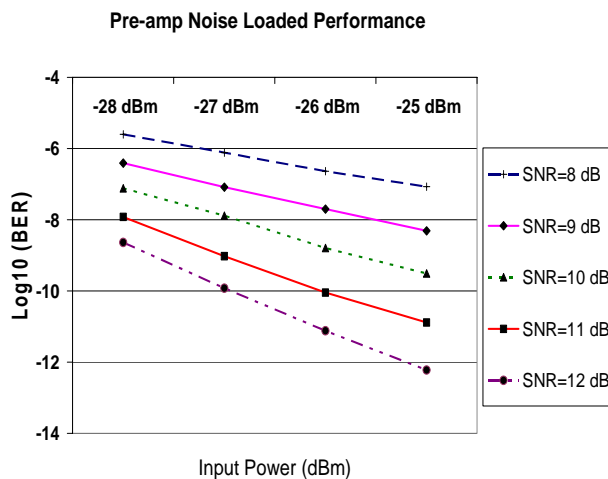


Figure 5: Receiver performance change at different input powers and different input SNR

Conclusion

The results of this work show a need for designing the pre-amp EDFA and photon detector as one subsystem, and also demonstrate that computer simulations and characterization experiments together are needed for the optimization of pre-amp EDFA performance. Then, the pre-amp EDFA needs to be fine-tuned at the optical receiver level. This was done by minimizing EDFA noise performance at the pre-amp EDFA level using computer simulations and experimentally at the optical receiver level. So, the optical receiver transmission performance should be used to characterize the EDFA performance at different operating conditions.

References

- [1] D. Dahan, A. Levy, D. Jacobian, E. Yohi, and U. Mahlab. "ASE Noise Instability Mitigation in WSS Based Closed Amplified Ring Networks". Optical Fiber Communications Conference (OFC) paper JTHA108 (2008).
- [2] A. Abu-aisheh, and S. Moslehpour, "Pre-amp EDFA ASE Noise Minimization for Optical Receiver Transmission Performance Optimization," CISSE Conference (2007).
- [3] J. T. Verdeyen, "Laser Electronics," third edition, Prentice Hall (1995).
- [4] Becker, Olsson, and Simpson, "Erbium-Doped Fiber Amplifiers, Fundamentals and Technology," Academic Press, NY, (1999).
- [5] A. Abu-aisheh, "Pre-amp EDFA Noise Characterization for Optimal Optical Receiver Transmission performance," *Ph.D. dissertation*, Dept. of Elec. Eng. Florida Institute of Technology, Melbourne, FL (2003).
- [6] Xiupu Zhang and Alan Mitchell, "A Simple Black Box Model for Erbium-Doped Fiber Amplifiers." IEEE Photonics Technology Letter, VOL., 12, NO. 1, January (2000).
- [7] M. Wada et al. "Full-WDM-Band Photodiode Modules for Optical Communications at 40 Gb/s and Beyond" OFC (2003).
- [8] P. J. Winzer, R.-J. Essiambre, "Optical Receiver Design Trade-Offs" OFC (2003).

Biographies

AKRAM ABU-AISHEH is an Assistant Professor of Electrical and Computer Engineering at the University of Hartford. He is currently the assistant chair of the Electrical and Computer Engineering Department and director of the Electronic and Computer Engineering Technology program. Dr. Abu-aisheh has a doctorate in Optical Communications from the Florida Institute of Technology and, Master of Science and Bachelor of Science degrees in Electrical Engineering from the University of Florida. Dr. Abu-aisheh may be contacted at abuaisheh@hartford.edu

HISHAM ALNAJJAR is an Associate Professor of Electrical and Computer Engineering at the University of Hartford, where he is also the Associate Dean of the College of Engineering, Technology, and Architecture. Previously, he served for nine years as the Chair of the Electrical & Computer Engineering Department at the University of Hartford. Dr. Alnajjar has a doctorate from Vanderbilt University and a Master of Science degree from Ohio University. Dr. Alnajjar may be contacted at alnajjar@hartford.edu

A COMPARATIVE ANALYSIS AND EVALUATION OF DIFFERENT APPROACHES OF GLOBALIZATION OF ENGINEERING CURRICULUM IN THE USA

Quamrul H. Mazumder, University of Michigan-Flint

Abstract

To sustain global technological leadership, the need for globalizing U.S. engineering education has been widely recognized by academic, industry, and government institutions for several decades. The world today is much flatter, requiring a wider view towards design and development of products due to socio-economic diversities of prospective customers. Engineering, manufacturing, and information technology projects require multinational teams of professionals to work together where communication skills, cultural awareness, and interpersonal skills are extremely critical.

Study abroad, student exchange, faculty exchange, foreign language study, and international collaborative projects have been used by academic institutions. A study has been conducted by the author that includes the perspectives of students, faculty, and professional engineers employed in the industry from both the United States and abroad. The study solicited input from the above group of individuals about their input regarding effective ways to globalize U.S. engineering education. In this paper, different approaches used for globalization of engineering curriculum will be examined along with the results of the study. This paper will also present the author's evaluation of effective ways of globalization and his recommendation for the improvement of engineering curriculum.

Introduction

This paper is the second and final part of a multi-stage research project. In part one, the "preparedness level" of engineering graduates from U.S. universities was presented and concluded that the prepared level was less than adequate [1]. The study was extended in an attempt to provide a solution to the problem identified in the previous paper by organizing responses regarding effective ways for globalizing engineering education.

A comprehensive survey forms the crux of this multi-stage research project. The concluding question of the survey questionnaire was a subjective one soliciting feedback on how to globalize engineering education. A wide array of responses was received from various sects of respondents. In addition, a literature survey showed various approaches

employed by educational institutions and industries in an attempt to formulate standards of globalization.

For decades, approaches used for globalization of academic curriculum and industrial practices can be categorized as student/faculty exchange programs, global study, foreign language study, and international studies and global project experience. The aforementioned list is not exhaustive, as there are other possibilities of standalone methods, which may not fit into any of the above categories. In this paper, an attempt was made to parse and subsequently cluster responses into one of the categories. Responses were used as an index of quantitative comparison of various methods. This paper is divided into four sections: brief analysis of previous work, survey respondent distribution, statistical analysis of preferred globalization approach, and conclusions with author's recommendations.

Related Studies

Student exchange programs and global study have been one of the most commonly used methods for globalization. In a typical student exchange program, students attend an overseas institution for one to two semesters where they take courses that apply towards their degree program. The Global Engineering Education Exchange (Global EEE) Program was initiated fourteen years ago, focusing on providing undergraduate engineering students international academic experiences and industrial internships. Over the years, the program developed to national stature with more than 200 exchanges annually and involving more than 80 major engineering schools throughout the world. Gerhardt et al. [2,3] provided the basic concept, philosophy, practice, progress to date, and the remaining challenges associated with the Global EEE Program [2].

The Department of Aerospace and Mechanical Engineering at the University of Notre Dame joined several other engineering departments in offering foreign study programs for undergraduates. Students have benefited by obtaining critical technical and business knowledge, making valuable contacts and developing an understanding of the host country's customs and practices [4]. Worcester Polytechnic Institute (WPI) has incorporated a project-based curriculum that provides opportunities for undergraduate students to com-

plete meaningful off-campus experiences. WPI offers students the flexibility to complete three different degree requirements away from campus under the direct supervision of WPI faculty. WPI has addressed the issues raised by ABET Engineering Criteria 2000. It focuses on aspects of the program that are clearly connected to multi-disciplinary teaming, professional and ethical responsibility, communication competence, a real understanding of the impact of solutions in a global and societal context, knowledge of contemporary issues, and the motivation for life-long learning [5]. Universities in Europe are adopting the bachelor-masters-doctoral (BMD) system as the de facto international standard for engineering education. The driving force for this dramatic change is globalization of the economy, society, industry, and education. Globalization has developed a need for European multinational companies to hire engineers with a more practical education, and for European engineering programs to better compete for graduate students from overseas institutions [6]. Engineering graduates must be competent in teamwork, communication skills, project management, and problem solving from a global perspective. The North American Free Trade Agreement (NAFTA) has further intensified the globalization of science and industry to unanticipated levels. Sadat-Hossieny et al. examined methods and practices undertaken by engineering schools across the United States to create curricular paradigms such as the Global Engineering College (GEC) or virtual engineering college [7].

The global engineering education project [8] at North Carolina A&T State University expands the activities of an on-going student exchange program and promotes a wider participation by students and faculty. The overall goal is to develop students' abilities to work effectively in a global environment. The student exchange program allows participating students to spend one semester at the host institution, attend classes, earn credits, and transfer them to the home institution. The aluminum-based design of mini Baja project used a multicultural team of student to work on a major meaningful project. A&T students and faculty worked closely with the team members from Ghana to design and develop the vehicle.

Faculty exchange programs are another approach for globalizing engineering education. Zia et al. [9] summarizes his experience in organizing a faculty exchange program as one of many elements of international cooperation, as well as the challenges associated with such programs. The objective was to present and promote the faculty exchange program as one of the many components of international cooperation in engineering education.

The Chemical Engineering Department at Iowa State University (ISU) developed several opportunities for students to

study in overseas institutions to earn credits towards their degree. Interest among both faculty and students has increased significantly since the inception of the program in the last decade. A number of faculty members have traveled to overseas institutions as well as a number of faculty members from overseas institutions have visited ISU for extended periods [10].

International studies are being used by a number of U.S. institutions as an approach for globalization. Oregon State University's innovative International Degree Program [11] allows students to earn a concurrent bachelor's degree in International Studies associated with an engineering degree. The program requires foreign language proficiency, overseas experience, courses with a cross-cultural focus, and a thesis. The program draws on campus resources such as overseas study programs, international internships, and the honors college, and it enlists engineering faculty members as thesis advisors.

A global collaboration project allows students and professionals to gain meaningful and valuable experience that is one of the most important skills required by employers. Large-scale software development requires communication and coordination among specialists from different fields. To help this generation of software developers understand the distributed, collaborative development process, Favela et al. [12] designed a course entitled the Distributed Software Engineering Laboratory. In this course, pairs of students from different countries work as a virtual organization overseeing the total software development process. In the same context, Xiaoqing [13] elaborates challenges and issues with collaborative global software development and education.

In 1990–91, WPI launched a major initiative, the Global Perspective Program [14], aimed at extending WPI's commitment to global education beyond the off-campus experience of international exchanges and project programs. The Global Perspective Program calls for globalizing all aspects of the WPI educational programs, on campus as well as off campus, by incorporating global perspectives throughout every discipline on campus, as well as within nonacademic programs. Hong Kong University of Science and Technology (HKUST) established a global collaborative educational program [15] at the Master of Science level in electronics packaging to educate skilled engineers, technical managers, and visionary leaders who can pull off the transition to the future for the electronics packaging industry. The program is based in the Mechanical Engineering (ME) Department with course contribution from the Electronics and Electrical Engineering (EEE) Department, the Chemical Engineering Department, the Industry Engineering Department, and IEEE-CMPT. Curricula of this program include traditional

engineering core courses and specialized electronic packaging courses.

Corporations and governments are challenged by a demanding global economy that requires mobility of capital and labor, organizational re-structuring across national boundaries, development, and implementation of more efficient production and manufacturing practices. Yet we know very little about how engineers understand and experience globalization, and how globalization affects their education, practices, and collaborations with non-engineers. Lucena et al. [16] collected data through ethnographic fieldwork and interviews and showed how globalization requires non-technical skills to solve complex engineering problems.

The educational experience of future manufacturing engineers should reflect the fact that manufacturing is becoming increasingly a global activity. Stephan et al. [17] showed a complex picture that implies a continuing presence for significant manufacturing in the United States as well as substantial growth abroad. A review of most current U.S. manufacturing engineering programs shows that relatively few acknowledge the international nature of manufacturing in their published course requirements. This author recommended including more material on the global aspects of manufacturing in undergraduate engineering curricula.

Survey Respondent Distribution

The survey on globalization of engineering education received 785 responses, which was conducted through the popular online surveying tool Zoomerang. Out of 785 respondents, 67 percent accounted for student responses, 25 percent of respondents were faculty members, and professional engineers working in the industry (others) made the remaining 8 percent responses.

The approximate student to faculty ratio of 3 to 1 is justified with typical student to faculty ratios in U.S. universities, which hovers around 15 to 1. The lower 8 percent professional engineer (others) respondents can be attributed to the fact that globalization of engineering education and the global work platform are current issues, and a significant part of the existing workforce are unaffected by it. From a futuristic perspective, the upcoming generation of students will be affected by rapidly evolving global engineering work platform. As such, 67 percent student respondents are justified.

Table 1. Respondents' Academic/Employment Status

		Frequency	Percent
Valid	Faculty	194.0	24.7
	Other	61.0	7.8
	Student	525.0	66.9
	Total	780.0	99.4
Missing	1	5.0	0.6
Total		785.0	100.0

Statistical Analysis

A chi-square test is a general technique for the analysis of categorical data used to test the association between two categorical variables (generally a "group" variable and a "response" variable) in a given set of data. Specifically, the null hypothesis being tested is that two variables are independent of each other, or that the distribution of categorical responses for one group will be identical to that of all other groups. In the present paper, chi-square tests were used to compare certain groups in terms of their distributions of responses to selected categorical questionnaire items (e.g., comparing respondent groups in terms of endorsement of the Student Exchange Program). For example, a chi-square test was used to test for an association between respondent groups (five levels) and endorsement of the Global Study Program (possible responses parsed into yes and no, i.e., two levels). Tables 3.1 and 3.2 show the cross-tabulation results and chi-square test for this example analysis. The chi-square statistic in this case had 4 degrees of freedom (df) and was equal to 5.615 with a p-value of 0.230. This p-value indicates that there was a more than 20 percent chance of observing an association of this magnitude or larger if these data were collected from a population where there was no association between respondent groups and endorsement of the Faculty Exchange Program (i.e., a population where the null hypothesis was true). As a result, we would accept the null hypothesis and conclude that no significant differences were observed between these five groups in terms of endorsement of global study programs.

Cross-Tabulation and Chi-Square Tests

Given the tabulated data, and the fact that respondents could indicate multiple solutions for globalization, each individual solution for globalization was analyzed separately

using chi-square analysis. Specifically, the five groups of respondents were compared in terms of the probability of endorsing a particular solution using chi-square tests.

The five respondent groups were as follows:

1. Faculty-U.S.
2. Faculty Non-U.S.
3. Student-U.S.
4. Student Non-U.S.
5. Others (professional engineers in the industry)

Of the 785 total survey respondents, 235 respondents provided an open-ended response endorsing at least one approach that can be used for globalizing engineering education. A small number of respondents did not endorse any of the above, stating that they did not feel any need for the globalization of engineering education. Their point of view was that U.S. engineering education is one of the best and highly recognized in the world and that graduates can work in a global workplace with some training that is usually provided by the employer.

Table 2. Case Processing Summary

	Cases					
	Valid		Missing		Total	
	N	Percent	N	Percent	N	Percent
group * endorse	235	100.0%	0	.0%	235	100.0%

A series of six different chi-square tests were performed using the statistical analysis software SPSS (Version 14.0) to assess the bivariate associations between respondent groups and the endorsement of different globalization approaches. The first chi-square test examined the association between respondent group and endorsement of the Global Study Programs. Tables 3, 4, and 5 and Figure 1 illustrate these cross-tabulation results and the corresponding chi-square test results.

Table 3. Cross-tabulation of Respondent Group with Global Study Endorsement

		Endorse		Total	
		No	Yes		
Group	Faculty-US	Count	56	6	62
		% within group	90.3%	9.7%	100.0%
	Faculty-Non US	Count	34	6	40
		% within group	85.0%	15.0%	100.0%
	Student-US	Count	83	15	98
		% within group	84.7%	15.3%	100.0%
	Student-Non US	Count	10	5	15
		% within group	66.7%	33.3%	100.0%
	Other	Count	16	4	20
		% within group	80.0%	20.0%	100.0%
	Total	Count	199	36	235
		% within group	84.7%	15.3%	100.0%

Table 4. Chi-Square Tests

	Value	df	Asymp. Sig. (2-sided)
Pearson Chi-Square	5.615 ^a	4	.230
Likelihood Ratio	5.020	4	.285
Linear-by-Linear Association	3.160	1	.075
N of Valid Cases	235		

a2 cells (20.0%) have expected count less than 5. The minimum expected count is 2.30.

The result of the respondents' endorsement of different approaches and their corresponding p-values from six different chi-square tests are presented in Table 4.

Table 5. Results of Chi-square Tests (p-value) and Endorsements of Globalization Approaches by Group

Globalization Approaches	Faculty US	Faculty Non US	Student US	Student Non US	Other	Chi-Square P-Value
Global Study	9.70 %	15.0 0%	15.3 0%	33.3 0%	20.0 0%	0.23
Student Exchange	11.3 0%	25.0 0%	7.10 %	13.3 0%	0.00 %	0.02
Faculty Exchange	6.50 %	27.5 0%	5.10 %	13.3 0%	0.00 %	< 0.001
Foreign Language	9.70 %	12.5 0%	28.6 0%	0.00 %	40.0 0%	0.001
Global Project	30.6 0%	12.5 0%	29.6 0%	40.0 0%	30.0 0%	0.181
No need for Globalization	12.9 0%	2.50 %	5.10 %	0.00 %	0.00 %	0.074

Among five different globalization approaches, the chi-square test p-values range from less than 0.001 to 0.230, indicating varying levels of agreement among different respondent groups regarding different approaches. The highest p-value (p=0.23) observed in the global study approach indicates a more universal agreement among the respondents groups in endorsing global study as an effective approach. About 33 percent non-U.S. students and 20 percent of engi-

neers working in the industry endorsed global study compared to only 9.7 percent of the U.S. faculty. The next highest p-value observed ($p=0.181$) was for the global project experience approach where 30 percent of the engineers working in the industry and 30 percent of U.S. faculty endorsed this approach. The lowest p-value ($p < 0.001$) was observed for the Faculty Exchange Program, which indicates a significant level of disagreement among respondent groups in terms of endorsement of the Faculty Exchange Program. About 27 percent of non-U.S. faculty endorsed this approach compared to only 6.5 percent of U.S. faculty, and no respondents representing engineers working in the industry endorsed this approach. Endorsements of different globalization approaches by different respondents groups are summarized and presented in Figure 1.

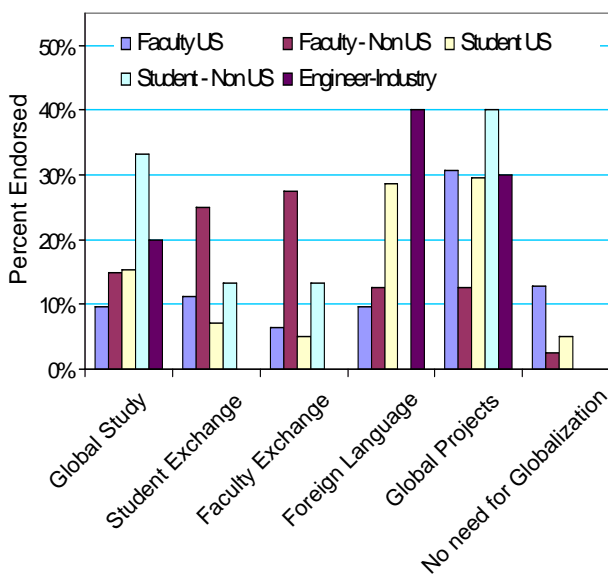


Figure 1. Endorsement of Global Study by Different Group of Respondents

Summary and Conclusion

Table 6 shows the overall summary of endorsement of different approaches by all groups indicating global projects with approximately 28 percent or highest level of endorsement followed by incorporating foreign language in U.S. engineering curriculum with 20 percent endorsement. One important parameter worth mentioning regarding foreign language is that the respondents emphasized a foreign language from a country with an emerging economy. Lowest number of endorsement was observed for faculty exchange programs without considering a small segment of the respondents who did not feel any need for globalization at all. It was interesting to observe that most of the respondents who did not feel any need for globalization are engineering

faculty from U.S. institutions. This interesting phenomenon clearly shows a difference in perception regarding globalization between U.S. engineering students and engineers working in the industry who strongly felt the need for globalization.

Table 6. Overall Summary of Endorsement of Different Approaches

Name of Program	% Endorsing
Global Study	15.30
Student Exchange	11.10
Faculty Exchange	9.40
Foreign Language	20.00
No Need for Globalization	6.00
Global Project	27.70

Although this group of respondents preferred global projects and foreign language study to be the two most effective ways for globalization of U.S. engineering education, the appropriate globalization method may depend upon the program requirements. Realizing the constraints associated with the number of credit hours and total time required for a bachelor's degree in engineering along with institutional and accreditation (ABET) criteria, requiring foreign language study may pose a challenge to curriculum redesign. This study was performed to improve our understanding of the higher education stakeholder's perspective about which approaches are most effective to further globalize U.S. engineering education.

The author recommends incorporating one or more of the above approaches in the current engineering curriculum to improve the global awareness and skill of U.S. engineering students. This may seem to be burdensome to the program and institution in the short term but will provide meaningful and valuable experiences to prepare our students to address future global challenges.

Acknowledgement

The author would like to express sincere thanks to Dhruva Baishya, an undergraduate student in computer science, engineering science, and physics, who provided assistance in this paper. The author also thanks Brady West, statistical consultant of the UM-Flint research office for the statistical analysis and interpretation of the results. Thanks to the UM-Flint Office of research for providing undergraduate student support through UROP program.

References

- [1] Mazumder, Q.; Baishya, D. Globalization of Engineering Education: Are we preparing students to succeed in the Global economy? In the proceedings of the 115th ASEE Annual Conference & Exposition 2008, AC 2008–752.
- [2] Gerhardt, L.A. The global engineering education exchange program - its history, progress, and challenges Source: In the proceedings of Frontiers in Education Conference, v 3, 2001, p S2D/13.
- [3] Gerhardt, L.A.; Martin, S. The Global Engineering Education Exchange Program - a worldwide initiative. In the proceedings of the Frontiers in Education Conference, 1999. 29th Annual Volume 1, 1999 pp 11B7/10–11B7/13.
- [4] Fortenberry, N. L. Under the jeweler’s loupe: Global engineering education. *Computer Applications in Engineering Education*, v 4, n 2, 1996, p 169–172.
- [5] Mello, N.A. How one institution provides a global perspective for Engineer? In the proceedings of the Frontiers in Education Conference, 2001 31st Annual Volume 3, 2001 pp. S1D - 1–5 vol.3.
- [6] Yeargan, J.; Hernaut, K. The globalization of European engineering education: an American observer’s perspective In the proceedings of the Frontiers in Education Conference, 2001. 31st Annual Volume 3, pp. S2D - 1–5 vol.3.
- [7] Sadat-Hossieny, M.; Allameh, S. M.; Rajai, M. Globalization of engineering curricula in the United States and abroad. In the proceedings of the ASEE Annual Conference and Exposition, 2005. pp 6937–6945.
- [8] Owusu-Ofori, S.; Klett, D.; Pai, D.; Roberts, K.; Obeng, D.; Agbeko, E. Global engineering education project at North Carolina A&T State University. In the proceedings of the Frontiers in Education Conference, 2001, volume 3, pp S1D/10–S1D/13.
- [9] Zia, O. Faculty exchange, one aspect of international co-operation in engineering education In the proceedings of the ASEE Annual Conference and Exposition, 2002, p 1475–1479.
- [10] Ulrichson, D. L. International Study program for students in engineering. In the proceedings of Frontiers in Education Conference, 1984, p 232–233.
- [11] Herling, D.; Herling, A.; Peterson, J. Integrating engineering and global competencies: a case study of Oregon State University’s International Degree Program. In the proceedings of the Frontiers in Education Conference, 2001 31st Annual Volume 2, pp: F2B - 4–7.
- [12] Favela, J.; Pena-Mora, F. An experience in collaborative software engineering education. In: *Software, IEEE Volume 18, Issue 2, March-April 2001* pp: 47–53.
- [13] Xiaoqing, L. Collaborative global software development and education. In the proceedings of the 29th Annual International Computer Software and Applications Conference, COMPSAC’05. Volume 1, pp: 371.
- [14] Hakim, H. Global Perspective Program; WPI’s response to global challenges. In the proceedings of the 21st Annual Conference Engineering Education in a New World Order, 1991, pp: 96–100.
- [15] Tong, P.; Lam, D.C.C.; Yuen, M.M.F.; Kim, J.K.; Lee, R.S.W.; Lee, S.H.K.; Chan, P. Global collaborative electronic packaging education. In the proceedings of the 49th Electronic Components and Technology Conference, 1999, pp: 907–911.
- [16] Lucena, J. C. Career paths of non-engineers into engineering practice in the midst of globalization: Implications for engineering education. In the proceedings of the ASEE Annual Conference and Exposition: *Staying in Tune with Engineering Education*, 2003, p 927–94.
- [17] Stephan, K.D.; Sriraman, V. Globalizing manufacturing engineering education. In the proceedings of the International Symposium on Technology and Society, 2004. ISTAS’04. pp: 111–117.

Biography

QUAMRUL MAZUMDER is currently the Assistant Professor of Mechanical Engineering and Engineering Science program at University of Michigan-Flint. His main area of research includes engineering education, globalization, multiphase flow, computational fluid dynamics, and alternate energy. Dr. Mazumder has more than 18 years of experience as a professional engineer and educator. Dr. Mazumder can be reached at qmazumde@umflint.edu

ACTIVE NOISE CONTROL USING THE FILTERED-X RLS ALGORITHM WITH SEQUENTIAL UPDATES

Li Tan, Purdue University North Central; Jean Jiang, Purdue University North Central

Abstract

In this paper, we develop a filtered-X recursive least square (FXRLS) algorithm with sequential updates. Although the standard FXRLS algorithm demonstrates faster convergence speed over the standard filtered-X least mean square (FXLMS) algorithm, its high computational cost hinders its applications in active noise control. The proposed method compromises its performance by using partitioned parallel sub-filters each with a reduced filter order to achieve reduction of computational complexity. The FXRLS algorithm with sequential updates may have a potential application for nonlinear active noise control (ANC) to achieve an improved performance over the standard FXLMS algorithm.

Introduction

Active noise control [1]–[5] has been an area of active engineering practice for the past few decades. The techniques used in active noise control (ANC) systems are based on the principle of superposition of the primary noise source and secondary source with the acoustic output being same amplitude and opposite phase of the primary noise source. The secondary source is provided by the adaptive linear controller using a filtered-X adaptive algorithm such as the least mean square (LMS) algorithm or recursive least square (RLS) algorithm. The ANC systems [1]–[5] have been successfully applied in actively controlling broadband noise and narrowband noise in the areas of the air conditioning system, exhaust and motor systems, headsets, and so on.

A typical ANC system for ducts implemented by a feed forward controller scheme is illustrated in Figure 1, where it consists of a reference sensor (reference microphone), a secondary source (secondary speaker), and an error sensor (error microphone).

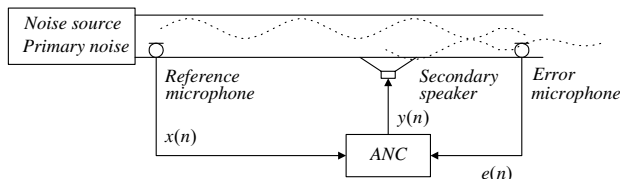


Figure 1. Feedforward ANC system in a duct

The primary noise is sensed through the reference microphone, which is located close to the noise source. The ANC system uses the sensed reference signal $x(n)$ to generate a canceling signal $y(n)$, which drives the secondary speaker to destructively attenuate the primary noise. An error microphone is used to detect the residue noise $e(n)$, which is feedback to the ANC system, to monitor the system performance. The residue noise $e(n)$ and the reference signal $x(n)$ are used together by the linear adaptive controller, whose coefficients are adjusted through an adaptive algorithm to minimize the measured error signal $e(n)$ or the residue acoustic noise.

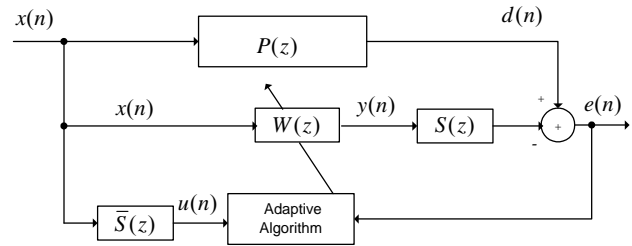


Figure 2. Block diagram of the single channel ANC system using the filtered-X adaptive algorithm

Figure 2 presents the block diagram of a single channel feedforward ANC system depicted in Figure 1 using the filtered-X adaptive algorithm, where $P(z)$ designates the primary path between the reference sensor and the error sensor, $S(z)$ the secondary path between the ANC adaptive filter output and the error sensor, and $\bar{S}(z)$ the secondary path estimate. Note that $W(z)$ denotes the transfer function of the linear adaptive control filter, while $u(n)$ is the filtered reference signal for the filtered-X adaptive algorithm. The standard FXLMS algorithm with less computational complexity has been very successfully applied for active control of the broadband and narrow band noise, particularly for reduction of low frequency noise [1]–[3].

Many successful active noise control systems use the FXLMS algorithm because of its simplicity and lesser computational complexity. A faster convergence speed can be obtained by using the FXRLS algorithm [1] and [5]. However, because the FXRLS algorithm requires a high compu-

tational cost [1], we usually prefer to use the FXLMS algorithm in a real-time implementation. To take advantage of the FXRLS algorithm, we compromise its performance by using partitioned parallel sub-filters each with a reduced filter order and then applying the FXRLS algorithm to each sub-filter independently to obtain the reduction of computational complexity. The algorithm can be adopted for a situation where the convergence speed of the algorithm is demanding, while the computational cost is also affordable. In this paper, we will focus on developing sequential update strategies for the FXRLS algorithm and demonstrate that the proposed FXRLS algorithm with sequential updates (FXRLS-SEQ) could reduce the computational cost as well as offer the flexibility for selective coefficient updates.

FXRLS Algorithm with Sequential Updates

We first derive an RLS algorithm with sequential updates and then modify it to an FXRLS algorithm with sequential updates (FXRLS-SEQ). Given a linear adaptive finite-impulse response (FIR) filter $y(n) = W(n)X^T(n)$ with its coefficient and input vectors defined as

$$W(n) = [w_0(n) \ w_1(n) \ \cdots \ w_{L-1}(n)]^T$$

and

$$X(i) = [x(i) \ x(i-1) \ \cdots \ x(i-L+1)]^T,$$

respectively, we express the exponentially weighted cost function with a forgetting factor of λ as

$$\zeta(n) = \sum_{i=1}^n \lambda^{n-i} e^2(i) \quad (1)$$

where the error at past time index i is defined as

$$e(i) = d(i) - W^T(n)X(i) \quad \text{for } 1 \leq i \leq n \quad (2)$$

Now, if we partition the filter into M parallel sub-filters, Equation (2) can be rewritten as

$$e(i) = d(i) - \sum_{k=1}^M W_k^T(n)X_k(i) \quad (3)$$

Taking the derivative of the cost function $\zeta(n)$ to the j th sub-filter coefficient vector $W_j(n)$ leads to

$$\begin{aligned} \frac{\partial \zeta(n)}{\partial W_j(n)} = & 2 \sum_{i=1}^n \lambda^{n-i} \left(d(i)X_j(i) - \sum_{k=1, k \neq j}^M X_j(i)X_k^T(i)W_k(n) \right) \\ & - 2 \sum_{i=1}^n \lambda^{n-i} \left(X_j(i)X_j^T(i)W_j(n) \right) \end{aligned} \quad (4)$$

Assuming that the filter coefficients are slow time-varying, that is, $W_k(n) \approx W_k(n-1)$ for $k \neq j$, we can develop a cross-

correlation vector based on the second line of Equation (4). It follows that

$$\begin{aligned} P_j(n) &= \sum_{i=1}^n \lambda^{n-i} \left(d(i)X_j(i) - \sum_{k=1, k \neq j}^M X_j(i)X_k^T(i)W_k(n) \right) \\ &= \lambda \sum_{i=1}^{n-1} \lambda^{n-1-i} \left(d(i)X_j(i) - \sum_{k=1, k \neq j}^M X_j(i)X_k^T(i)W_k(n-1) \right) \\ &\quad + d(n)X_j(n) - \sum_{k=1, k \neq j}^M X_j(n)X_k^T(n)W_k(n-1) \end{aligned} \quad (5)$$

Then, we can further express Equation (5) through the following recursion:

$$\begin{aligned} P_j(n) &= \lambda P_j(n-1) + d(n)X_j(n) \\ &\quad - \sum_{k=1, k \neq j}^M X_j(n)X_k^T(n)W_k(n-1) \end{aligned} \quad (6)$$

Defining an autocorrelation matrix updated as

$$R_j(n) = \lambda R_j(n-1) + X_j(n)X_j^T(n)$$

and applying the matrix inversion lemma [1],

$$A = B^{-1} + CD^{-1}C^T$$

and

$$A^{-1} = B - BC(D + C^TBC)^{-1}C^TB,$$

in which we set the following:

$$A = R_j(n),$$

$$B^{-1} = \lambda R_j(n-1),$$

$$C = X_j(n),$$

and

$$D = 1,$$

we obtain the gain vector $k_j(n)$ and the inverse of the autocorrelation matrix $Q_j(n) = R_j^{-1}(n)$ below:

$$k_j(n) = \frac{\lambda^{-1}Q_j(n-1)X_j(n)}{1 + \lambda^{-1}X_j^T(n)Q_j(n-1)X_j(n)} \quad (7)$$

$$Q_j(n) = \lambda^{-1}Q_j(n-1) - \lambda^{-1}k_j(n)X_j^T(n)Q_j(n-1) \quad (8)$$

Again, using Equations (7) and (8) yields

$$k_j(n) = Q_j(n)X_j(n) \quad (9)$$

Next, multiplying the inverse of the autocorrelation matrix by the cross-correlation vector, we can determine the Wiener solution for the filter coefficient vector $W_j(n)$ as

$$\begin{aligned} W_j(n) &= Q_j(n)P_j(n) \\ &= \lambda Q_j(n)P_j(n-1) + Q_j(n)d(n)X_j(n) \\ &\quad - \sum_{k=1, k \neq j}^M Q_j(n)X_j(n)X_k^T(n)W_k(n-1) \end{aligned} \quad (10)$$

Applying Equations (6) and (8) to Equation (10), it follows that

$$\begin{aligned}
W_j(n) &= \lambda Q_j(n) P_j(n-1) + k_j(n) d(n) \\
&- \sum_{k=1, k \neq j}^M k_j(n) X_j^T(n) W_k(n-1) \\
&= (Q_j(n-1) - k_j(n) X_j^T(n) Q_j(n-1)) P_j(n-1) \\
&+ k_j(n) d(n) - \sum_{k=1, k \neq j}^M k_j(n) X_k^T(n) W_k(n-1)
\end{aligned} \tag{11}$$

Distributing $P_j(n-1)$ in Equation (11) and using Equation (10), it leads to

$$\begin{aligned}
W_j(n) &= W_j(n-1) \\
&+ k_j(n) \left(d(n) - \sum_{k=1}^M X_k^T(n) W_k(n-1) \right)
\end{aligned} \tag{12}$$

Define the innovation $\alpha(n)$ as

$$\alpha(n) = d(n) - \sum_{k=1}^M X_k^T(n) W_k(n-1) \tag{13}$$

Substituting Equation (13) for (12), we yield the following coefficient update equation

$$W_j(n) = W_j(n-1) + k_j(n) \alpha(n) \tag{14}$$

Equations (13), (7), (14), and (8) constitute a general procedure for the FXRLS algorithm with selective coefficient updates.

For active noise control applications, we first replace the innovation in Equation (13) with an error signal $e(n)$ because it is obtained from the error sensor. Second, we shift Equation (14) by one sample to make $W_j(n)$ available for processing the next incoming sample. Finally, we use the filtered input signal $u(n)$, similar to [1], to achieve the FXRLS algorithm with sequential updates (FXRLS-SEQ) as

$$e(n) = d(n) - s(n) * y(n) \quad (\text{from the sensor}) \tag{15}$$

$$y(n) = \sum_{k=1}^M W_k^T(n) X_k(n) \tag{16}$$

$$u(n) = s(n) * x(n) \tag{17}$$

for $j = 1, 2, \dots, M$

$$k_j(n) = \frac{\lambda^{-1} Q_j(n-1) U_j(n)}{1 + \lambda^{-1} U_j^T(n) Q_j(n-1) U_j(n)} \tag{18}$$

$$W_j(n+1) = W_j(n) + k_j(n) e(n) \tag{19}$$

$$Q_j(n) = \lambda^{-1} Q_j(n-1) - \lambda^{-1} k_j(n) U_j^T(n) Q_j(n-1) \tag{20}$$

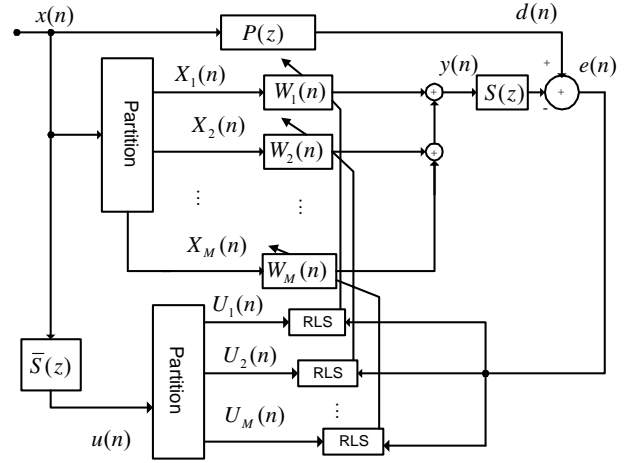


Figure 3. FXRLS algorithm with sequential updates

Figure 3 depicts the implementation of the FXRLS-SEQ algorithm, where $S(z)$ and $\bar{S}(z)$ are the secondary path and its estimate, respectively, $P(z)$ the primary path, $u(n)$ filtered input; $X_1(n)$, $X_2(n)$, and $X_M(n)$ are the partitioned input vectors for all the sub-filters, while $U_1(n)$, $U_2(n)$, and $U_M(n)$ are the partitioned filtered input vectors. Note that the computational cost of the standard RLS algorithm is proportional to the square of the filter order N^2 . Because the developed FXRLS-SEQ algorithm is sequentially applied to each sub-filter with a reduced filter order, the cost is then a sum of computations contributed by the FXRLS algorithm with a reduced size applied in each sub-filter. Table 1 lists the computational requirements counted for Equations (18)–(20) for the developed FXRLS-SEQ algorithm and the requirement for the standard FXRLS algorithm. As an example of $N = 100$ and $M = 10$ for each sample, the standard FXRLS filter requires 40,300 multiplications and 30,000 additions while the developed FXRLS-SEQ takes 4,300 multiplications and 3,000 additions. Although we focus on the most conservative way to reduce the algorithm complexity, according to the framework illustrated in Figure 3, many other possibilities for selective coefficient updates, including partial updates, could be evolved.

Table 1. Complexity Comparisons of the FXRLS and FXRLS-SEQ algorithms

Algorithm type	Multiplications	Additions
FXRLS	$4N^2 + 3N$	$3N^2$
FXRLS-SEQ	$4N^2 / M + 3N$	$3N^2 / M$

Experiments

To demonstrate the performance of the developed FXRLS-SEQ algorithm for active noise control applications, we applied MATLAB software, including its Signal Processing Toolbox, and conducted simulations by considering the following conditions. The secondary path and its estimate with minimum phases [4] were chosen as

$$S(z) = \bar{S}(z) = z^{-2} + 0.5z^{-3}$$

The primary noise at the canceling point was generated according to the following model:

$$d(n) = x(n) * p(n) + v(n),$$

where $*$ denotes linear convolution and $p(n)$ is the impulse response of the primary path [4] given as

$$P(z) = z^{-4} - 0.3z^{-5} + 0.2z^{-6}$$

The reference noise $x(n)$ was a white Gaussian process with the power of 1, and the disturbance $v(n)$ was selected as a white noise process with the Gaussian distribution. We used the signal power to noise power ratio (SNR) as 40 dB for all of our simulations. The filter memory size $N = 12$ and forgetting factor $\lambda = 0.996$ were chosen for all FXRLS algorithms. We examined two different types of partitions. The first choice was to simply split the filter coefficients into two groups to form two sub-filters (we refer to the algorithm as the FXRLS-SEQ-2). For comparisons of performance degradation, we could also divide the filter coefficients into four portions to obtain four sub-filters (we call the algorithm the FXRLS-SEQ-4). In the second choice, we first applied the FXRLS-SEQ algorithm to odd-numbered coefficients and then to even-numbered coefficients (we refer to this algorithm as the FXRLS-SEQ-I2) for each input sample.

The MATLAB simulation results are shown in Figure 4, in which the normalized MSEs versus the number of iterations by each algorithm are displayed. To achieve results as shown in Figure 4, we first applied each adaptive algorithm, respectively, to our ANC system described in Figure 2. The reference noise was generated using the simulated Gaussian noise, which was fed to the ANC system and the primary path in order to create the primary noise at the canceling point. Furthermore, the primary noise was added by its disturbance noise with the SNR=40 dB. The adaptive filter using the designated algorithm produced the canceling output, which was subtracted from the noise at the canceling point. The result was the residue error whose power was minimized through the adaptive algorithm used. Each MSE value for the plot was obtained by averaging the square values of 50 past residue errors, and it was further normalized to the noise power at the canceling point. The resultant normalized MSEs using each adaptive algorithm were plotted in terms of the number of iterations in Figure 4 for comparisons of

the convergence speeds. After 5,000 iterations, all algorithms converged and achieved approximately the normalized MSE as -40 dB. As far as the convergence speed, the developed FXRLS-SEQ-2 converged faster than the FXRLS-SEQ-4 and much faster than the FXRLS-SEQ-I2. However, as we expected, the FXRLS-SEQ-2 converged slower than the standard FXRLS algorithm. The FXRLS-SEQ algorithm with interleaving coefficient partitions did not perform well when compared to direct partition algorithms such as the FXRLS-SEQ-2 and FXRLS-SEQ-4 algorithms. Figure 5 shows the noise to be controlled and the controlled output at the canceling point for each applied algorithm. The top first plot is the noise to be canceled. The second plot is the canceled noise using the standard FXRLS algorithm. The rest of plots are the canceled noise signals by each of our developed algorithms with sequential updates. Clearly, as shown in Figure 5, the FXRLS-SEQ2 shows the best performance in our developed algorithms (fastest speed of convergence).

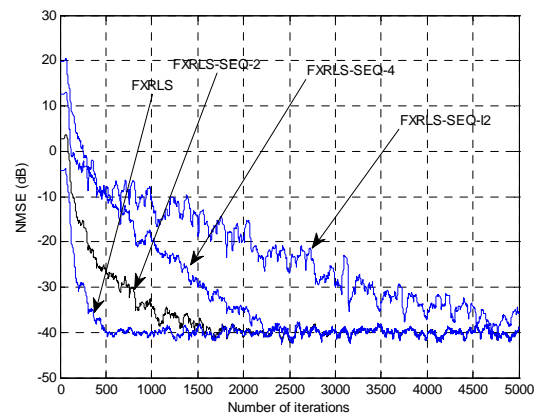


Figure 4. Performance comparisons of the FXRLS and FXRLS-SEQ algorithms

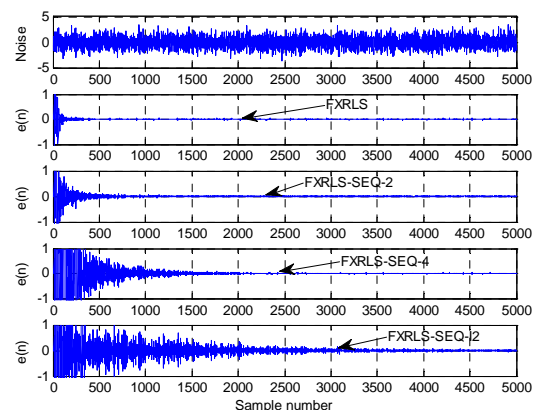


Figure 5. Noise to be controlled and controlled output using FXRLS and FXRLS-SEQ algorithms

Figure 6 lists the MATLAB sample program for the FXRLS-SQ2 algorithm. We could easily implement the other algorithms by modifying the following program.

```

order_N=12; %linear filter length
total_n=5000; %number of iterations
sigma2x = 1; %signal power
sigma2n=0.0001; % noise power
lambda=0.996;inv_lambda = 1/lambda; delta=0.005;
w1=zeros(1,order_N/2);w2=w1;
Q1 = eye(order_N/2)/delta;Q2=Q1;
SB = [ 0 0 1 0.5]; % secondary path
y_s=zeros(1,length(SB)-1);
SBE = [ 0 0 1 0.5]; % secondary path estimate
y_se =zeros(1,length(SBE)-1);
x = sqrt(sigma2x)*randn([1,total_n]); %reference noise
v = sqrt(sigma2n)*randn([1,total_n]); % disturbance

% noise at canceling point
d=filter([0 0 0 1 -0.3 0.2],1,x)+v; % noise to be canceled
% filtered input for few samples
[u(1:order_N-1),y_state_e]=...
filter(SBE,1,x(1:order_N-1),y_state_e); % filtered input

% FXRLS-SQ2 algorithm beginning at n=order_N:
for n = order_N:1:total_n
[u(n),y_se]=filter(SBE,1,x(n),y_se); %filtered input
U1(1:order_N/2) = u(n:-1:n-order_N/2+1);
U2(1:order_N/2) = u(n-order_N/2:-1:n-order_N+1);
X1 = x(n:-1:n-order_N/2+1); % input vector 1
X2 = x(n-order_N/2:-1:n-order_N+1); %input vector 2
y = [w1 w2]*[X1 X2]'; % adaptive filter output
[anc_y y_s] = filter(SB,1,y,y_s); %controlling output
e(n) = d(n) - anc_y; % controlled output =residue error

% The gain for sub-filter 1:
k1 = inv_lambda*Q1*U1'; k1 = k1/(1+U1*k1);
w1 = w1 + k1* e(n);
Q1 = inv_lambda*(Q1-k1*U1*Q1);

% The gain for sub-filter 2:
k2 = inv_lambda*Q2*U2'; k2 = k2/(1+U2*k2);
w2 = w2 + k2* e(n);
Q2 = inv_lambda*(Q2-k2*U2*Q2);
end

% compute and plot the MSE
MSE = zeros(1,total_n);
for i=51:total_n
MSE(i)=mean(e(i-1:i-50).^2);
end
logMSE = 10*log10(MSE/mean(d.*d)); % NMSE
plot(logMSE);grid;axis([0 5000 -50 30]); %plot NMSE
figure;plot(e);grid; %plot the controlled output

```

Figure 6. MATLAB sample program for the FXRLS-SEQ-2 algorithm

Figure 7 shows the performances for controlling narrow-band noise that consists of a sum of sinusoids of 400 Hz, 500 Hz, and 600 Hz components. The plots shown in Figure 7 were obtained similarly to those in Figure 5, except for the sum of sinusoids as opposed to the white Gaussian noise during the MATLAB simulations. We observed that updating strategies of splitting coefficients and interleaving coefficients received the similar performance degradation. Note that the FXRLS-SEQ-I4 algorithm partitions the coefficients by collecting one of every four coefficients to form a sub-filter.

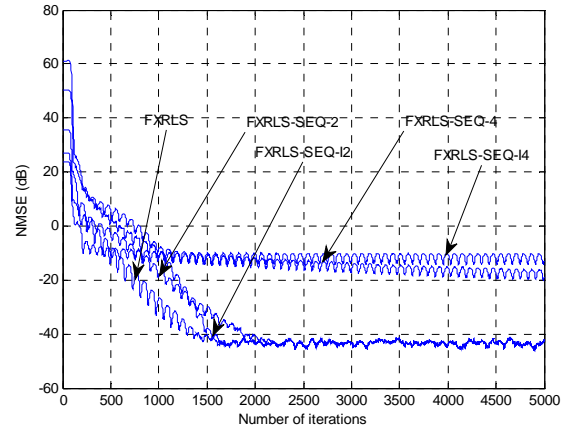


Figure 7. Performance comparisons of the FXRLS and FXRLS-SEQ algorithms

Conclusions

In this paper, we have developed a filtered-X RLS algorithm using sequential updates (FXRLS-SEQ) to reduce the computational cost with compromised performance degradation in its convergence speed. We have also derived a general frame for the FXRLS algorithm with selective coefficient updates. The FXRLS-SEQ algorithm uses partitioned parallel sub-filters and applies the standard RLS algorithm with a smaller size to each sub-filter independently to reduce the computational cost. The developed algorithms have compromised performances as compared to the standard FXRLS algorithm, but they all eventually converge to the global minimum. The developed method has the potential to be applied to the nonlinear active noise control in which adaptive polynomial filters and multi-channel structures are employed, and this research topic is currently under investigation. The algorithm could also be an alternative for applications in which a quicker speed of algorithm convergence is required and it is necessary for the computational cost to be affordable.

References

- [1] M. Kuo and D. R. Morgan, *Active noise control systems-algorithms and DSP implementations*. John Wiley & Sons, New York, 1996.
- [2] S. J. Elliott and P. A. Nelson, "Active noise control," *IEEE Sig. Process. Mag.*, pp. 12–35, 1993.
- [3] L. Tan and J. Jiang, "Filtered-X second-order Volterra adaptive algorithms," *Eletron. Lett.*, vol. 33, No. 8, pp. 671–672, Apr. 1997.
- [4] L. Tan and J. Jiang, "Adaptive Volterra filters for active control of nonlinear noise processes," *IEEE Trans. Signal Processing*, vol. 49, No. 8, pp. 1667–1676, August 2001.
- [5] G. L. Sicuranza and A. Carini, "Nonlinear multichannel active control using partial updates," *Proc. ICASSP-2005*, pp. 109–112, 2005.

Biographies

LI TAN is a faculty member with the College of Engineering and Technology at Purdue University North Central. He received his M.S. and Ph.D. degrees in Electrical Engineering from the University of New Mexico in 1989 and 1992, respectively.

Dr. Tan is a senior member of IEEE. His principal technical areas include digital signal processing, adaptive signal processing, and digital communications. He has published a number of papers in these areas. He authored and co-authored two textbooks: *Digital Signal Processing: Fundamentals and Applications*, Elsevier/Academic Press, 2007; *Fundamentals of Analog and Digital Signal Processing*, Second Edition, AuthorHouse, 2008. Dr. Tan can be reached at lizhetan@pnc.edu

JEAN JIANG is a faculty member with the College of Engineering and Technology at Purdue University North Central. She received her Ph.D. degree in Electrical Engineering from the University of New Mexico in 1992.

Dr. Jiang is a member of IEEE. Her principal technical areas include digital signal processing, adaptive signal processing, and control systems. She has published a number of papers in these areas. She co-authored a textbook: *Fundamentals of Analog and Digital Signal Processing*, Second Edition, AuthorHouse, 2008. Dr. Jiang can be contacted at jjiang@pnc.edu

INCORPORATING SYSTEM-LEVEL DESIGN TOOLS INTO UPPER-LEVEL ELECTRICAL ENGINEERING COURSES

Wagdy H Mahmoud, University of the District of Columbia

Abstract

This paper provides details of our electrical engineering efforts to vertically integrate system-level design tools with many junior, upper-level, and capstone courses. The paper also provides the details of developed laboratory exercises and projects in the areas of image processing, digital communication, and embedded processing. In addition, the paper details the challenges involved in using continually-evolving, system-level design tools and the efforts made to reduce their learning times.

Introduction

The Accreditation Board for Engineering and Technology (ABET) requires providing students with a significant hands-on interdisciplinary design experience. Graduating electrical engineering students should have the ability to design systems, subsystems, and components for real-time, application-specific hardware systems. They should also be able to implement these designs in functional hardware and test the hardware in real-world operating conditions. Students need to understand that their choices of implementation algorithm, style of functional units' implementations (serial, parallel, or pipelines), variable widths, and implementation board have a major impact on the quality of their designs.

Contemporary Electronic Design Automation (EDA) industry projects exhibit the following trends: a) increased design complexities; b) shorter time-to-market; c) increased dependency on intellectual property (IP) cores; d) hardware/software co-design; and e) system on a chip (SoC).

To improve graduating engineering students' productivities and prepare them for professional careers in the EDA industry, system-level design tools are being introduced in the upper-level and capstone design courses of the electrical engineering curriculum. To achieve such professional competence, students should be required to participate in a sequence of system-level design experiments and projects. These laboratory exercises aim at: a) familiarizing students with available design tools and implementation FPGA boards; b) sharpening students' abilities to design complex systems that include software and hardware components and to interface these designs to peripheral devices; c) exposing

students to contemporary soft-core and hard-core processors; d) preparing students to design and implement useful applications; and e) providing students with lessons that can help them become life-long learners and successful professionals. The experiments provide the framework that guide students through a top-down approach to defining the problem; devising complete design specifications; partitioning the design into cooperating hardware and software functional blocks; generating alternative forms of design for each block; and comparing the costs, area, power consumption, development time, and performances of these alternatives when implemented on real hardware (FPGA). The interdisciplinary design projects emphasize the hardware/software co-design and implementation of applications, the design and use of intellectual property (IP) core libraries, and system-on-a-chip (SoC) concept.

The system-level software packages used include MATLAB, Simulink, assortment of MATLAB toolboxes and blocksets, Xilinx Integrated System Environment (ISE), Xilinx System Generator (SysGen), Xilinx embedded design kit (EDK), Xilinx ChipScope, Xilinx AccelDSP, and ModelSim from Mentor Graphics. MATLAB toolboxes and blocksets provide commonly used design components and parameterized functions needed to model the majority of digital control, DSP, and digital communication systems. The SysGen provides a system-level design environment for FPGAs. SysGen is a toolbox that runs within the Simulink environment to produce HDL synthesizable code. SysGen also allows an HDL co-simulation and hardware-in-the-loop to verify the correctness of the produced design. The SysGen provides the resources to quantize double-precision data into a fixed-point format, which is suitable for the hardware implementation. The resource estimation utility of the SysGen provides an estimation of the hardware resources needed for the hardware implementation of the design using the target FPGA chip. The EDK allows the user to incorporate soft-core processors (Microblaze™ or PicoBlaze™) or to interface the built-in PowerPC processors with the reconfigurable FPGA resources. Such processors can also be used to interface the hardware system to a variety of input/output peripheral devices needed to supply input data to the hardware system and/or to display the results of processing. Both SysGen and EDK allow interfaces to IP core libraries. The use of IP cores allow designers to concentrate on the overall system design and performance without having to spend time to verify the correctness or performance of the system's components. The ModelSim simulation package provides

both functional and timing simulation for the hardware design. The use of system-level tools provides students with the technical skills needed for an integrative approach to real-time digital systems design, simulation, testing, and implementation. Students also acquire significant hands-on experience in design, development, and verification of complex digital systems that have potential societal benefits.

The FPGA boards include the Spartan-3, Spartan-3E Starter Kit, Spartan-3A DSP, the XUP-V2Pro, and the DO-ML403-EDKISE-PC4-US. The reconfigurable resources of the Spartan-3E FPGA chip can be used to implement PicoBlaze™ and Microblaze™ soft-core processors. The V2Pro board contains one V2pro FPGA chip with two IBM PowerPC embedded processors, Audio Codec, and connectors to gigabit serial input/output. The DO-ML403 board contains a Virtex-4 FX chip that is optimized for embedded processing and supports both the PowerPC™ hard and MicroBlaze™ soft processors. These boards allow designers to interface with pre-designed IP cores or with custom-built IP cores. They can be used to implement a configurable system-on-a-chip (CSoc) for DSP and embedded applications.

The following sections of this paper provide a brief overview of some of the tools used and present the details of some of the laboratory exercises and projects in the areas of embedded processing, digital signal processing, and communication systems.

Embedded Processing Tools and Projects

According to the 2006 annual embedded market survey, embedded processors account for more than 98 percent of the processor market, and most new embedded system designs are using 32-bit processors. Unlike general-purpose processors that are optimized for a mix of I/O and compute-intensive applications, embedded processors are low-cost processors that are optimized to perform a specific function. Embedded processors are extensively used in a wide variety of applications, such as mobile phone systems, automotive applications, office and home equipments, aerospace applications, and defense systems. Therefore, embedded system design courses are used to teach interdisciplinary designs.

The embedded design interdisciplinary capstone design projects presented in this paper emphasize the use of hardware/software co-design methodologies, the design and use of intellectual property (IP) soft-cores such as the PicoBlaze and the MicroBlaze, hardwired embedded processors such as the PowerPC 405 and system-on-a-chip (SoC) concept, and high-level languages programs for designing embedded controllers and applications.

The PicoBlaze™ Architecture

The PicoBlaze is an 8-bit RISC microcontroller soft-core that can be efficiently embedded on the fabric of a variety of Xilinx Field Programmable Gate Arrays (FPGA) chips. The PicoBlaze microcontroller is a synthesizable VHDL source code that consumes 96 slice cells when implemented on a Spartan-3 XC3200 chip (approximately 5 percent of the chip total logic capacity). The microcontroller has 16 byte-wide general-purpose registers, a byte-wide ALU, 64 byte-wide internal general-purpose scratchpad RAM, CALL/RETURN stack up to 256 input and up to 256 output ports [1]. It can execute approximately 1K sequential instructions stored in its memory within the FPGA chip, typically in a single 1K x18-block RAM. The PicoBlaze has three versions of the assembler; each is optimized for a specific set of Xilinx FPGA chips. In this effort, the Constant (K) Coded Programmable State Machine (KCPSM3) assembler is utilized. The PicoBlaze instruction set is close to the 8086/8088 instruction set. The complete instruction set for the PicoBlaze can be found in reference [1]. The microcontroller executes each instruction in two clock cycles and can deliver approximately 44 MIPS in a Spartan-3 FPGA and approximately 100 MIPS in a Virtex-4 FPGA. The PicoBlaze microcontroller is designed for non-timing control functions and managing peripheral operations.

PicoBlaze Laboratory Exercises and Projects

The following set of PicoBlaze laboratory exercises and tutorials are used to teach students the details of the PicoBlaze soft-core microcontroller and how it can be used to design an embedded application

- a. Implement 8-bit by 8-bit, multiply and divide functions using bit-wise and, add and shift instructions available in PicoBlaze KCPSM3 assembly.
- b. Use the scratchpad RAM to display data on the 7-segment LEDs available on the Spartan-3 board or LCD displays available on the Spartan-3E board.
- c. FPGA implementation of an embedded processor with multiple peripherals, each of which has a different level of priority. This exercise introduces the concept of PicoBlaze interrupts.
- d. PicoBlaze microcontroller implementation within the Xilinx System Generator environment.
- e. Implement a simple encryption algorithm or a pulse width modulation function using the PicoBlaze KCPSM3 assembly.

The MicroBlaze™ Architecture

The MicroBlaze is a 32-bit RISC Harvard soft processor core that can be embedded in the reconfigurable logic of an FPGA chip [2]. The MicroBlaze has (32) 32-bit general-purpose registers, up to 14 special-purpose registers, arithmetic and logic unit (ALU), 32-bit data bus, 32-bit address bus, 32-bit instruction words, two levels of interrupts, and a single issue pipeline that can be configured as three stages or five stages. The MicroBlaze core is parameterized to allow enabling of a set of configurable features. The MicroBlaze has an extensive instruction set, with many of the operations having large number of variants for register, immediate, constant, signed, and unsigned operands [2]. This basic design can be configured with advanced features such as barrel shifter, memory management/memory protection unit, floating-point unit (FPU), caches, exception handling, and debug logic. In addition, some of these instructions, such as floating point multiplication and division, are optional in various hardware configurations. Optional support is provided for privilege mode, memory protection, and virtual address translation. The maximum performance of the MicroBlaze processor depends on the targeted FPGA chip and on the processor configuration. The fast simplex link (FSL) of the MicroBlaze allows users to interface an embedded or external hardware co-processor to accelerate the execution of compute-intensive, time-critical functions. The MicroBlaze soft-core processor is a major component of the Xilinx Embedded Development Kit (EDK). The EDK also includes the Xilinx Platform Studio™ Tool Suite (XPS) and a library of peripheral IP soft-cores. More information about the EDK concepts, tools, and techniques are found in reference [3].

MicroBlaze Laboratory Exercises and Projects

The following set of MicroBlaze laboratory exercises aims at familiarizing students with the EDK and MicroBlaze. These exercises target the Spartan-3E and the Spartan-3AN boards. The list of exercises includes:

- a. Creating a simple hardware and software processor system using the Base System Builder (BSB) and the Xilinx Intellectual Properties (IPs) available in the EDK. This exercise familiarizes students with the EDK environment and how to use it to design a reconfigurable embedded processing system, as well as how to connect it to peripheral devices. The I/O interface uses a universal asynchronous receiver/transmitter (UART) for serial communication. The UART is designed using an IP core. Other peripheral devices are also created using an available IP core library. The MicroBlaze generates the implementation netlists of the processor and the FPGA

implementation bit stream. Downloading the implementation bit stream onto the development FPGA board, the processor system is realized.

- b. Designing an information display system to display user-defined messages and information using a hyper-terminal.
- c. Designing a MicroBlaze embedded processor with multiple peripherals using both vendor-supplied and user-created custom IP cores, each of which has a different level of priority. This exercise enables students to work with interrupt in the MicroBlaze environment. Implement the design in the FPGA board.
- d. Designing a controller for an external flash memory. The flash memory can be used to store the processor program that is used to configure the FPGA chip automatically whenever the power is turned on.

For each designed system, the HW/SW system debug using the Xilinx ChipScope tool is performed.

The PowerPC 405 Processor Architecture

The PowerPC 405 is a 32-bit embedded RISC processor core that is designed for SoC applications [4]. Multiple PowerPC 405 cores are embedded inside the Virtex-II Pro and inside the Virtex-4 FPGA devices. The PowerPC 405 processor is a Harvard architecture with (32) 32-bit general-purpose registers, five-stage data path pipeline, ALU with multiply and divide units, auxiliary processing unit (APU), 16Kb data and instruction caches, IBM CoreConnect bus architecture, embedded memory management unit, dedicated on-chip memory interface to block RAMs (BRAMs), and debug and trace support. The PowerPC 405 is a low-power consumption processor with operating frequency at approximately 450 MHz in the Vitex-4 FX and 400 MHz in the Virtex-II Pro devices.

PowerPC 405 Laboratory Exercises and Projects

The PowerPC 405 (PPC) laboratory exercises are similar to those of the MicroBlaze. The following set of PowerPC exercises aims at familiarizing students with the PowerPC 405 architecture and its instruction set. They also help students gain experience in designing useful hardware/software embedded applications that target the Virtex-II Pro or the Virtex-4 FX devices. The set of exercises include:

- a. Creating a simple PPC processor to display user-defined messages and information using a hyperterminal. A

- UART is used to send displayed data to the hyper-terminal.
- Adding multiple peripherals to the PPC processor system using both vendor-supplied and user-created custom IP cores, each of which has a different level of priority. This exercise enables students to work with the PPC interrupt. The generated netlist for the design is used to implement the design in the FPGA chip.
 - Writing a basic software application to access the IP peripheral.
 - Adding a timer to the designed system.
 - Writing a software application that uses the timer.
 - Performing HW/SW system debug using the Xilinx ChipScope debugging tool.
 - Creating a core using Xilinx System Generator and adding it to a PPC 405 using the on-chip peripheral bus (OPB) and the processor local bus (PLB) interfaces.

After completing the above exercises, students are able to implement more complex projects similar to those implemented using the MicroBlaze. The project list includes:

- Using the Virtex-II Pro board equipped with VDEC1 video decoder to design a video-decoding system. The system converts analog video signal into digital values and displays the output on a standard VGA display connected to the board's SVGA port. The PPC 405 is used for the signal conversion computations, and the MicroBlaze soft processor is used to control the entire system and its peripherals.
- Using the V2Pro board equipped with Audio Codec AC97, connectors to gigabit serial input/output, a standard VGA display connected to the board's SVGA port, audio source, and a speaker to design audio processing system. The system captures and filters audio signals and plays back the filtered signal to the user's speakers. The filtered signals are also converted from the time domain to the frequency domain using a 64-point FFT. The sampled output of the FFT is displayed on the VGA monitor.

By implementing the same project in the MicroBlaze environment and the hardcore PPC, students gain valuable experience in both hardware and software implementations. Students evaluate and compare the designed projects in terms of design effort, performance, resource utilization, and cost.

Signal Processing Design Exercises

To prepare students for digital signal processing and communication systems design projects, students need to be familiarized with the SysGen tool. A set of laboratory exercises aimed at designing a digital FIR filter are used to teach

students the capabilities of the SysGen design tool. The FIR design set of exercises includes:

- Use the filter design toolbox to compute the FIR filter coefficients.
- Use the SysGen to create a multiply-accumulate (MAC) unit, which is the basic building block of the FIR filter. This exercise familiarizes students with the process of building a subsystem using the SysGen and Simulink blocks.
- Use the SysGen to create a parameterized dual-port RAM to store the FIR coefficients and data.
- Create the necessary control logic, such as address generator, for the dual-port RAM.
- Construct the FIR filter using the created MAC unit and the parameterized dual-port RAM, and test the design using Simulink sources. Verify the results using a spectrum scope.
- Compile the design for the target FPGA chip and perform a hardware-in-the-loop verification. Figure 1 shows the hardware-in-the-loop simulation of the FIR filter.
- Generate the VHDL code and implement the filter in the FPGA board using the ISE tools.

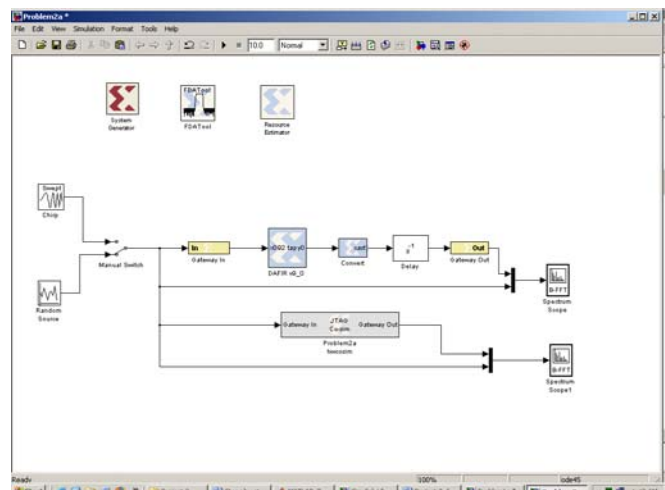


Figure 1. Hardware-in-the loop simulation of the FIR filter

By completing the above exercises, students gain substantial knowledge that enables them to implement more complex projects, such as a complex encryption algorithm, edge detection and feature extraction algorithms of images, or designing a controller for an industrial application. A description of the edge detection project follows.

The Edge-Detection Project

Edge detection algorithms are basic and essential tools used in a variety of digital signal processing applications,

such as feature extraction, target tracking, video surveillance, improving the appearance of blurred video streams, automated inspection of semiconductor chips finding the boundaries of organs in medical images, etc. MATLAB provides support for many methods for detecting edge in images such as Sobel, Prewitt, Roberts, Laplacian of Gaussian (LOG), Canny, and Zero-cross methods. Evaluating the performances of their algorithms and comparing their performances on images is beyond the scope of this paper. However, analysis of various edge-detection algorithms and their operators, the sequence of operation required for their use, and the choice of parameters can be found in references [5] and [6].

The first stage of this project involved using MATLAB coding and Simulink blocks to find the edge of an image. Figure 2 shows an original image, and Figures 3–7 details the results of these methods.

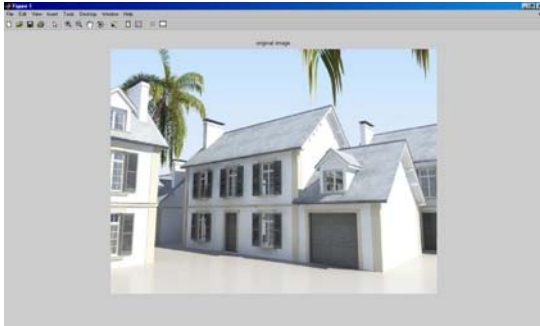


Figure 2. Original Image

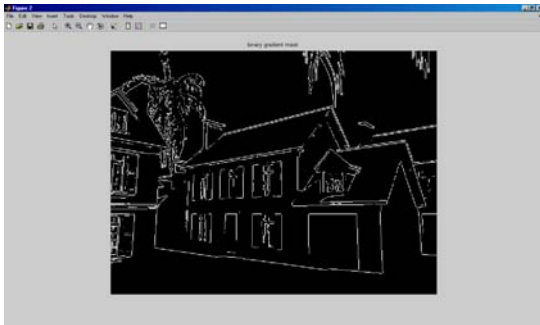


Figure 3. Edges Using Sobel Method

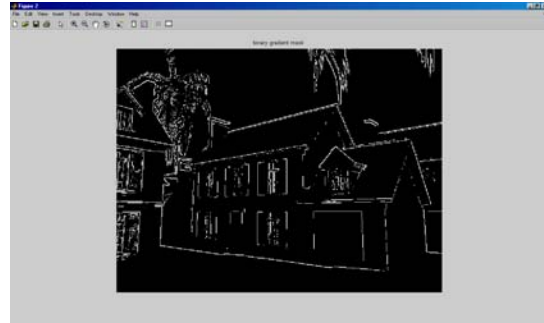


Figure 4. Edges Using Robert Method

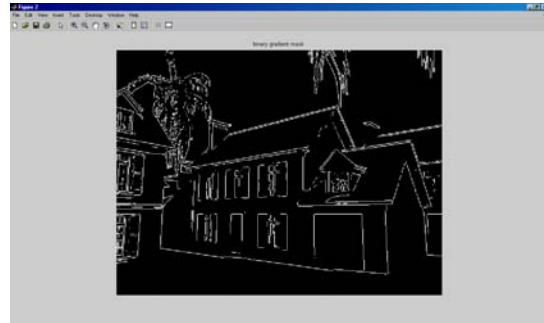


Figure 5. Edges Using Prewitt Method

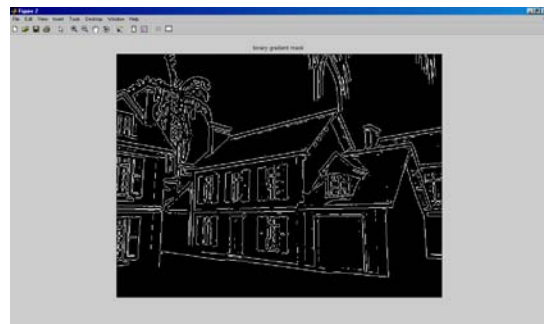


Figure 6. Edges Using LOG Method

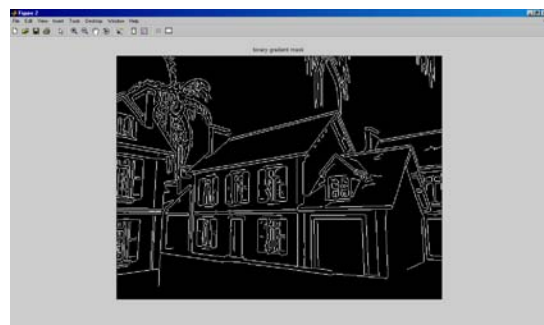


Figure 7. Edges Using Canny Method

The Simulink blocks for implementing Sobel algorithm are shown in Figure 8. The blocks for implementing Canny, Sobel, and Prewitt methods are shown in Figure 9.

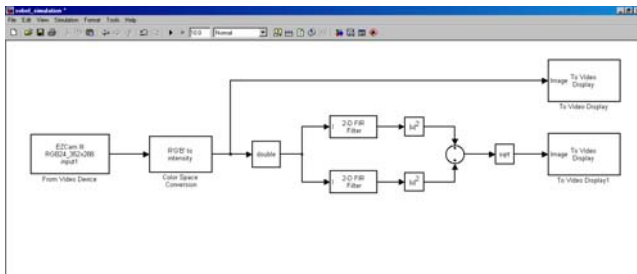


Figure 8. Simulink Blocks for Sobel Edge Detection

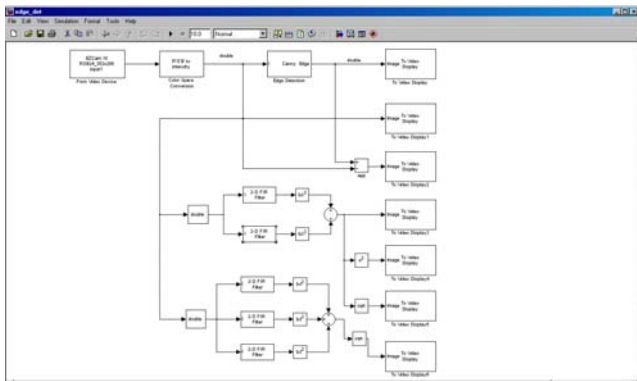


Figure 9. Simulink Implementation of Canny, Sobel, and Prewitt Methods

For real-time operation, Figure 10 shows the dialog block parameter needed to obtain live stream video from a Web-cam.

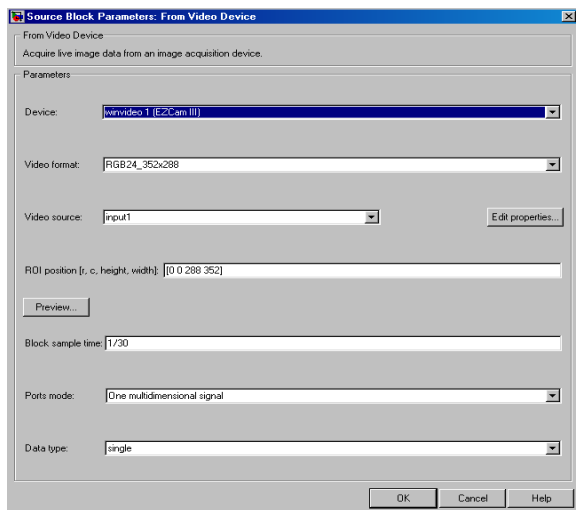


Figure 10. Block Parameter to Obtain Live Stream Video from Web-Cam

The user needs to convert the live stream video from RGB images to gray-scale images. The image noise needs to be removed using a 2-D filter. Figure 11 shows the simulation

result of processing one frame of the video stream using five different edge detection algorithms.

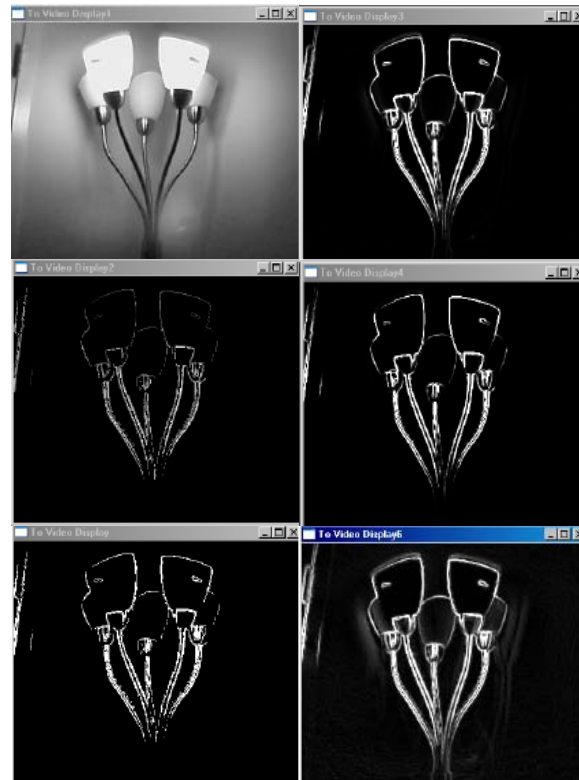


Figure 11. Simulation results.

The Digital Communication System Design project

This project familiarizes students with knowledge, tools, algorithms, and implementation platforms needed to design a communication (transceiver) subsystem. Students will be exposed to a variety of design options such as precision, quantization, sampling, and bit error rate (BER). The subsystems include matching filters, digital modulation (PSK, QAM, 4-QAM, 16-QAM, 64-QAM, 8-PSK, and 16-PSK), up/down conversion, DAC, timing and simulation, data recovery, demodulation, and BER testing. To prepare students for this project, the following set of laboratory exercises, with varying complexities, was developed. These exercises guide students in designing the components of telecommunication systems and implementation of the systems using an FPGA board. The exercise set includes the following:

- Design a matched filter, a polyphase filter for a given specification.
- Use MATLAB's bertool to compare the theoretical BER performance of various PSK and QAM modulation schemes.

- c) Build a BER testing model in Simulink, using blocks from the Communications and Signal Processing blocksets. Simulate the BER performance of 4-QAM, 16-QAM, 64-QAM, 8-PSK, and 16-PSK for a subset of signal-to-noise ratio (SNR) values.
- d) Design a Simulink demodulator.
- e) Build a system generator model that implements the 4-QAM, 16-QAM, 64-QAM, 8-PSK, and 16-PSK modulation schemes. Apply a single input of binary data bits running at a fixed sample rate to all modulation schemes. Compare the results with those obtained from the Simulink model.
- f) Parameterize the modulation schemes.
- g) Design a parameterized up-sample, and interpolate up-converter/down-converter, and digital/analog converter (DAC) units for a specific symbol rate, interpolation rate, carrier frequency, and output sample rate.
- h) Design a carrier recovery system using a phase error detector and a loop filter.
- i) Implement a timing synchronization scheme between the transmitter and receiver units.
- j) Generate the VHDL code for the transceiver system, and implement the transceiver using the FPGA board. Test the system.

After completing these exercises, students will possess the technical skills needed to design and simulate any type of digital transmitter/receiver communication system.

Major Challenges and Results

Introducing system-level and embedded processing design tools into undergraduate courses presents major challenges to the instructors of these courses. These include the following challenges:

- a) Number and functionalities of these tools: A large number of system-level and embedded processing tools and environments are used. These tools are produced by MathWorks, Xilinx, and Mentor Graphics. These tools are used for design creation; functional and timing simulation; debugging; design synthesis; and to map, route, and download the design onto the implementation FPGA device.
- b) Documentation sizes: Most of these tools have lengthy user guides, references, and getting started manuals.
- c) Frequency of tools updates and modifications: Currently, most of the software tools are being updated twice each year. FPGA chips and boards become obsolete in a few years.

The above mentioned challenges represent some of the major problems facing the instructor of courses that use these design tools. It is extremely time consuming to de-

velop good tutorials and meaningful laboratory exercises and senior design projects. Moreover, due to the high frequency of software updates and hardware advances, the developed tutorials and exercises may need to be updated each semester. In addition, instructors need to spend large amounts of time to help students with their work with these tools and to reduce their levels of anxiety and frustration.

Student Feedback and Conclusions

The author has been working on developing system-level design projects for the past few years. So far, student course evaluations have shown extremely positive responses to the materials introduced in previous capstone and digital design classes. Analysis of student responses to these newly-developed materials will be the subject of another paper.

References

- [1] *PicoBlaze user Guide*, Xilinx Inc., <http://www.xilinx.com/userguides/ug129.pdf>.
- [2] *MicroBlaze Processor Reference Guide*, Xilinx Inc., http://www.xilinx.com/ise/embedded/edk92i_docs/mb_ref_guide.pdf.
- [3] *EDK Concepts, Tools, and Techniques—A Hands-on Guide to Effective Embedded System Design*, Xilinx Inc., http://www.xilinx.com/ise/embedded/edk92i_docs/edf_ctt.pdf.
- [4] *IBM PowerPC ISS Reference Guide*, Xilinx Inc., http://www.xilinx.com/ise/embedded/edk92i_docs/osl_ib_rm.pdf.
- [5] Rangarajan, Srikanth. "Algorithms for Edge Detection." Stony Brook University. Web document link: www.ee.sunysb.edu/~cvl/ese558/s2005/Reports/Srikanth%20Rangarajan/submission.doc.
- [6] Mohsen Sharifi, Mahmoud Fathy, Maryam Tayefeh Mahmoudi. "A Classified and Comparative Study of Edge Detection Algorithms." 2002 IEEE International Conference on Information Technology, Las Vegas, NV, January 2002, PP. 117–120.

Biographies

WAGDY H MAHMOUD is an associate professor in Electrical and Computer Engineering at the University of the District of Columbia. He teaches courses in digital system design, hardware description languages, digital signal processing, digital control systems, VLSI, and digital communications. He performs research in developing reconfigurable computing systems applications. Dr. Mahmoud may be contacted at wmahmoud@udc.edu

TEACHING ELECTROMAGNETIC FIELDS WITH COMPUTER VISUALIZATION

Yeqin Huang, Bill W. Yang, Robert Adams, Brian Howell, James Z. Zhang, and Kenneth Burbank,
Western Carolina University

Abstract

Electromagnetic Fields is one of the most difficult subjects in the undergraduate curriculum of electrical engineering. Unlike mechanics that deals with concrete objects, electromagnetics deals with intangible fields distributed in space, a concept that is abstract and difficult to gain insight. Students usually feel overwhelmed by the sophistication of the theory and then lose interest in learning. It is therefore not surprising that Electromagnetic Fields has motivated a variety of developments in education techniques, designed to simplify it conceptually. In this paper, the strategy of computer visualization is explored for effective teaching. An assessment based on multiple-choice examination is done for evaluations of effectiveness of learning.

Introduction

It is a widely held and often articulated view that Electromagnetic Fields is one of the most difficult subjects in the curriculum of electrical engineering. Nevertheless, electromagnetic theory is the foundation of all electrical engineering. Electrical engineering students need a fundamental knowledge of the concepts and principles of electromagnetic fields. Therefore, intensive efforts have been made in the past years to explore effective teaching strategies [1]-[3].

Vision plays an important role in improving comprehension and perception of electromagnetic fields. One reason Electromagnetic Fields is considered by students to be a very difficult course is that electromagnetic fields, being vector functions of space and time, are conceptually abstract and hard to visualize. Invisibility is a considerable obstacle on the way to understanding physical phenomena.

The primary motivation here is to highlight physical concepts by offering students a mental image of electromagnetic phenomena. Taking advantage of computer graphics and simulations, students are exposed to the computer visualization of Electromagnetic Fields. It is observed that visual aids integrated with lectures help students develop a better conceptual understanding of electromagnetic phenomena. Meanwhile, computer simulations allow students explore the solutions in their own efforts and in every detail, hence deepen their understanding of the subject matter.

Course Outline

The course objective is to provide students an understanding of electromagnetic fields. Upon completion of the course, the students are supposed to accomplish the following goals:

- Demonstrate understanding of basic concepts of electric and magnetic fields.
- Demonstrate understanding of Coulomb's law, Gauss's law, Ampere's law and Faraday's law.
- Develop solutions to electrostatic and magnetostatic engineering problems by applying basic electromagnetic laws and mathematical concepts.

To avoid complicating matters by coping with mathematical concepts and electromagnetic laws simultaneously, the course is started with a short review of vector analysis. This approach separates mathematic theorems from physical concepts and avoids deviating students' attention from the understanding of physical laws in the flow of concepts.

After a brief review of coordinate systems and transformation, electrostatics is introduced as the first course block. The second block is devoted to magnetostatics, followed by an introduction to Faraday's law and Maxwell's equations. The list below shows the topics covered in the course:

- Coulomb's law and electric field intensity
- Gauss's law and electric flux density
- Electric potential
- Conductors and electrostatic shielding
- Dielectrics and capacitance
- Continuity equation
- Boundary conditions
- Poisson's and Laplace's equations
- Biot-Savart's law
- Ampere's law
- Magnetic flux density
- Magnetic forces, torque and moment
- Magnetic materials and inductance
- Magnetic circuits
- Faraday's law
- Displacement current
- Maxwell's equations

Computer Visualization of Electromagnetic Fields

Electromagnetic field theory is undoubtedly a subject that is elegant in structure and rigorous in formulation. However, for many students whose aptitudes do not incline them to mathematic abstraction may shy away from this course because of the abstraction and invisibility of the concepts involved in the theory. This difficulty can be alleviated by taking advantage of computer graphics and simulations.

The focus of computer visualization for the course is placed on leading students to gain insight of the fundamental concepts. Lectures on fundamental concepts are usually started with a statement of laws or principles, followed by a number of examples designed for interpretations of the physical meaning of the laws and concepts. The examples are carefully chosen in such a way that each example covers one aspect of the theory, and is easy for student to understand. All the examples, as a whole, form a complete interpretation of the theory. The COMSOL Multiphysics® solver is used for the computer simulations in a variety of electromagnetic problems. After observation of the examples, students are led to review the concepts and focus attention on the significant factors of the theory.

The advantage of this approach is to allow students to concentrate on the physical meaning of the abstract concepts, hence, to get an in-depth understanding of the theory. The approach to integrate computer visualization with the lectures, is the combination of visual aid demonstration in class and homework assignment for computer simulations. To present the shift from mathematical abstraction to computer visualization, some examples are given below.

(A) Point Charge Placed at the Center of a Conducting Shell

As an example of the applications of Gauss's law, this problem is first solved manually to show students how to calculate the electric field with existence of spherical symmetry. The field lines plotted in Figure 1 is then used to demonstrate that the field is spherically symmetric and is in radial direction. Two fundamental concepts are covered in this illustration: Gauss's law and spherical symmetry.

Figure 2 illustrates the simulation results of electrical potential in the conducting shell. The simulation is used to help students understand the concept of equipotential surface. Due to the spherical symmetry of the system in this example, the equipotential surfaces are concentric spheres.

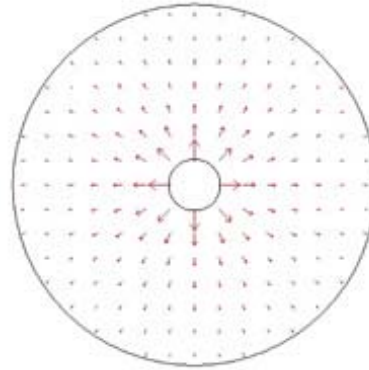


Figure 1. Electrostatic field in a spherical shell

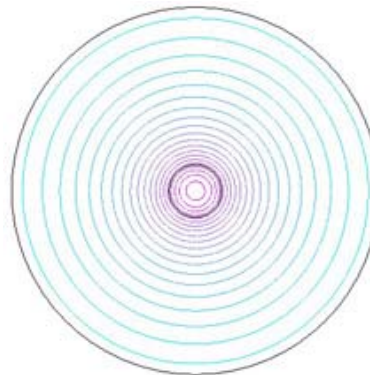


Figure 2. Electric potential in a spherical shell

(B) Boundary Value Problems

Electric potential fields within a source free region bounded by known potentials can be represented by solutions of Laplace's equation. The method of separation of variables is introduced for solving problems with canonical boundaries. A two dimensional problem with rectangular boundary is selected as a module to provide students with a fundamental knowledge of boundary value problems. In this example, the potential is positive on the right side of the rectangular boundary, and zero on the rest of the boundary. Following basic steps of the method of separation of variables, the solution is obtained in terms of an infinite series of eigenfunctions. Computer simulation as a visual aid, is introduced after mathematical manipulations of Laplace's equation.

The goal of the analytical approach is primarily to transform electromagnetic problem into mathematical expressions. For some students, this is a hard task and relies heavily on the students' mastery of mathematics. For those students whose interest is primarily in the applications of the theory, rather than in the mathematical abstraction or the beauty of the theory, the potential lines shown in Figure 3 and field lines in Figure 4 are more appealing than the deri-

vation of analytical solutions. Numerical results shown in the figures provide students with an alternative observation of boundary value problems, thereby generate their insight into the concepts.

Unlike analytical approach, in which the complexity of the problem depends heavily on the geometry of the boundary, numerical approach can be easily implemented to boundaries beyond rectangular shapes. Computer simulation of electric potential and field in a circularly bounded region with piecewise boundary conditions, shown in Figure 5 and 6 for example, is an educational outreach to the context of undergraduate EM course in which only rectangular boundary is dealt with.

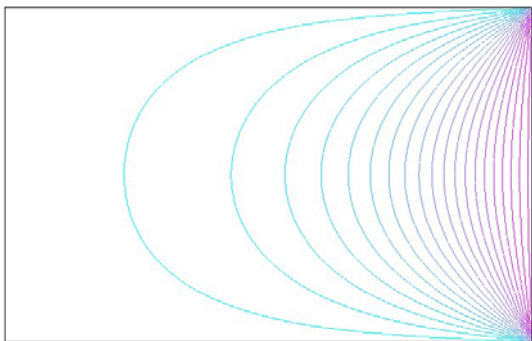


Figure 3. The electric potential in a bounded rectangular region

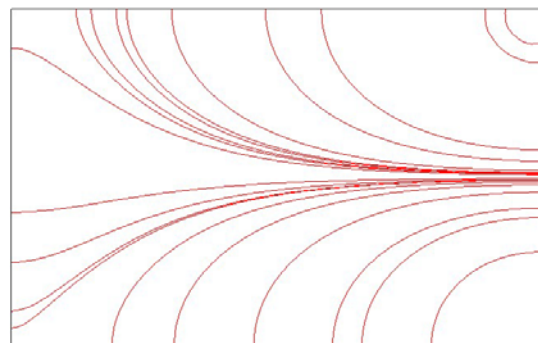


Figure 4. The electric field in a bounded rectangular region

Assessment Method

A multiple choice examination with 25 questions is used for the assessment; 12 of them are from the Electromagnetic Concepts Inventory [4]. All the questions are designed for testing whether or not students understand the fundamental concepts. No essential calculations are involved with the questions. Students are not allowed to use calculators in the examination.

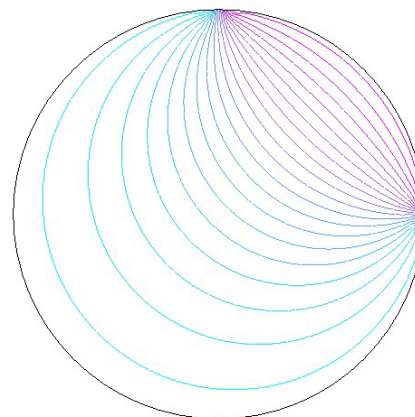


Figure 5. The electric potential in a circular region with piecewise Dirichlet boundary conditions

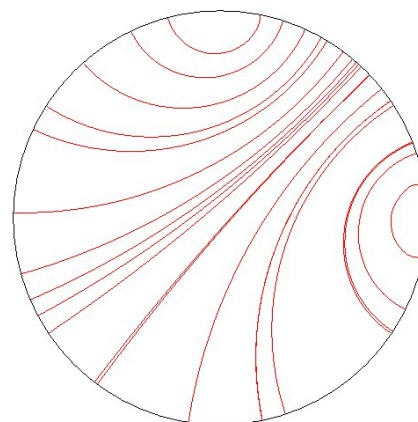


Figure 6. The electric field in a circular region with piecewise Dirichlet boundary conditions

Figure 7 shows one sample question. This question is designed to test the concept of electric flux and Gauss's law. In this question, since there is no electric charge enclosed by the surface S , by Gauss's law, the answer should be (a).

Figure 8 is another sample question for testing if students understand the connection between field and potential. It can be seen from the curve that the point at which the potential function has largest slope of decrease is point C, therefore the answer is (c).

Assessment results are presented in Figure 9 which shows the percentage of correct answers for each question. It is observed that for 15 of these 25 questions, over 70% students give correct answers; the concepts covered by these 15 questions are listed as follows:

- Coulomb's law.
- Gauss's law.

- Ampere's law.
- Faraday's law.
- Electric potential.
- Connection between field and potential.
- Boundary conditions.
- Electrostatic induction and shielding.
- Gradient of potential functions.
- Capacitance.
- Properties of conductors.
- Torque on a current loop in a magnetic field.
- Conservative nature of electrostatic field.

Question 4: Consider two parallel conducting plates, both are infinite in extent. A voltage V is applied across the plates as shown below, suppose S is a closed surface in the region between the two plates, and ϕ is the electric flux over S . Which of the following statements is true?

- (a) $\phi = 0$
- (b) ϕ is a positive constant
- (c) ϕ is a negative constant
- (d) ϕ is proportional to the area of S
- (e) ϕ is proportional to the voltage V

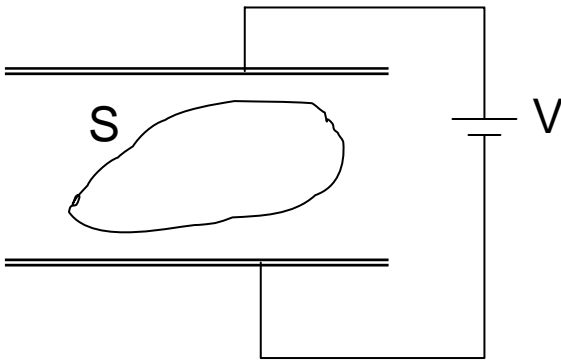


Figure 7. Sample question 4

Conclusion

The experience gained with using computer visualization in teaching Electromagnetic Fields has been described. Computer visualization of electromagnetic phenomena and introducing physical concepts, are combined to accomplish the course objectives. Assessment results indicate that desired effect on the students' learning of concepts is achieved.

Question 9: The electric potential V in a region is a function of coordinate x , and $V(x)$ is shown in the figure. Consider the electric field at points A, B, C, D, and E. The largest field intensity is at point

- (a) A, (b) B, (c) C, (d) D, (e) E.

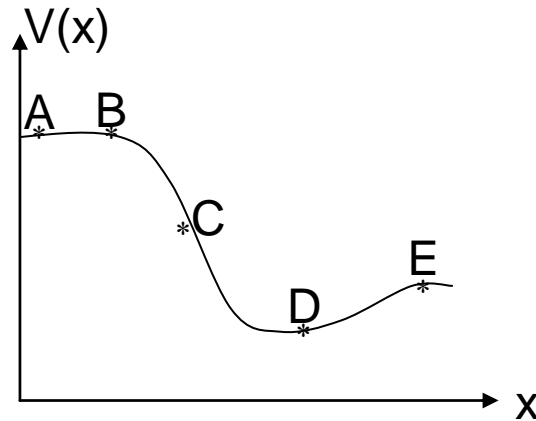


Figure 8. Sample question 9

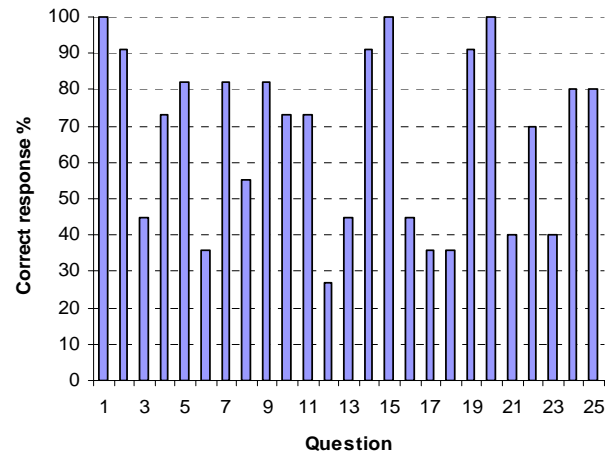


Figure 9. Results of assessment

It is observed that computer visualization integrated with examples in the lecture enhanced students' ability to transfer the concepts from the abstract level to the concrete level, thereby improving their conceptual understanding of electromagnetic phenomena. Computer aided visualization makes the study of Electromagnetic Fields more appealing.

References

- [1] D. A. Lowther and E. M. Freeman, "A new approach to using simulation software in the electromagnetics curriculum," *IEEE Trans. Educ.*, vol. 36, no. 2, pp. 219-222, May. 1993.
- [2] Peter S. Excell, "Experiments in the use of multiple-choice examinations for electromagnetics-related topics," *IEEE Trans. Educ.*, vol. 43, no. 3, pp. 250-256, Aug. 2000.
- [3] N. N. Rao, "PC-Assisted instruction of introductory electromagnetics," *IEEE Trans. Educ.*, vol. 33, no. 1, pp. 51-59, Feb. 1990.
- [4] B. M. Notaros, "Concept inventory assessment instruments for electromagnetics education," in *Proc. IEEE Antennas Propagation Society Int. Symp.*, 2002, vol. 1, pp. 684-687.

Biographies

YEQIN HUANG received a Ph.D. in electrical engineering from the University of Nebraska in Lincoln. He is an Assistant Professor in the Department of Engineering and Technology at Western Carolina University. His research interests include antennas and electromagnetic waves. He is a senior member of IEEE and a member of ASEE. Dr. Huang may be reached at yhuang@email.wcu.edu.

ROBERT ADAMS received a Ph.D. (2004) in electrical engineering from the University of Alabama in Huntsville. He has been a faculty member in the Department of Engineering and Technology at Western Carolina University since 2003. His research interests include numerical solutions to biomedical applications of electromagnetics, 3D modeling and visualization, and digital image processing. He is a member of ASEE and a senior member of IEEE. Dr. Adams may be reached at radams@email.wcu.edu.

JAMES Z. ZHANG is an Associate Professor with the Department of Engineering and Technology at Western Carolina University. His research interests include communications and DSP techniques for information processing. Dr. Zhang is a senior member of IEEE and a member of ASEE. Dr. Zhang may be reached at zhang@email.wcu.edu.

KEN BURBANK is a Professor of Electrical Engineering and Department Head of Engineering and Technology at Western Carolina University. Dr. Burbank is active with IEEE, OSA, and TAC of ABET. His current project is the testing of metamaterials at microwave frequencies. Dr. Burbank may be reached at kburbank@email.wcu.edu.

APPLICATION OF A SOFTWARE CONFIGURABLE DIGITAL SERVO AMPLIFIER TO AN ELECTRIC MACHINE CONTROL COURSE

Shiyoung Lee, Pennsylvania State University Berks Campus

Abstract

The various applications of the three-phase permanent magnet brushless dc motor (PMBDCM) in the industry are increasing. The main purpose of this paper is to describe the application of a new technology to academic electric machine control and/or power electronics drive courses. An easy method for the implementation of a fully software-configurable digital servo amplifier to drive a three-phase PMBDCM is presented in this paper. This developed servo amplifier may be suitable for an electric machine control course. The change of drive configuration requires additional development time and cost, especially in control software modification, which, in turn, depends on the specific application. The highlight of the paper is the GUI (Graphical User Interface)-based control software (Pro-Motion) setup for implementation of a software-configurable digital servo amplifier. The principle of the operation of the three-phase PMBDCM is discussed first, and then the requirement to develop three different types of servo amplifier-such as velocity, position, and torque servo amplifiers-to drive the three-phase PMBDCM, are explained. The details of a selected motor control integrated circuit (IC), MC73110 from PMD Corp., are introduced. The MC73110 IC is incorporated into the servo amplifier design, resulting in an increased ease of use with software configuration. To validate the software-configurable digital controller, a step-by-step design example to develop a velocity servo amplifier is completely explained and some of the test results are discussed. As a conclusion, suitable teaching topics based on the proposed software-configurable PMBDCM drive for electric machine control and/or power electronics drive courses are summarized.

Introduction

Today, numerous industrial applications are increasingly adopting the PMBDCM due to its inherent variable speed drive aspect. Since the electronic commutation circuit is necessary to drive the PMBDCM, it may not be easy to implement the PMBDCM drive. In most cases, it is time-consuming and expensive to build instructional components for motor drives into existing electric machine control related courses [1, 5, 6]. The implementation of hardware and

software usually takes time to complete. But many different types of development kits are available off the shelf for various types of motors [2]. These development kits are aimed mainly at the industrial sector, but they look attractive for educational application because they provide not only hardware platforms, but also dedicated setup software.

The MC73110-based development kit may be suitable for the fast and easy development of the PMBDCM drive instructional components. This paper proposes the MC73110 motor control IC-based developer's kit for this purpose. This kit was chosen for the easy and cost-effective implementation of the instructional component of the PMBDCM drive in the electric machine control course. The PMBDCM drive is increasingly popular in the industry sector, but it has not been integrated into an academic curriculum. Consequently, it is the logical choice for incorporation into an academic course that will prepare students for industry. The development kit provides a hardware platform that contains all necessary analog and digital circuits on one PCB and user-friendly GUI-based configuration software. The two-volume user manual is also a good resource to use in the design of any size and type of PMBDCM drive.

It is suitable and timely to investigate the incorporation of the PMBDCM drive into the electric machine control course. The design of the PMBDCM drive has two major tasks, one in hardware and another in software design. To accomplish both design tasks, one should understand its principle of operation. The hardware design could be classified as, but not limited to, power circuitry that includes a power switching circuit, analog and/or digital sensor circuits, and controller circuitry. The development of application-specific software for a motor drive is not always an easy task. Fortunately, the MC73110-based development kit provides user-friendly drive configuration software for easy setup of the desired type of the PMBDCM drive.

In this paper, the technical concepts of the PMBDCM and its drive are explained first to provide a fundamental background of the overall drive system suitable to the conventional electric machine control and/or power electronics courses. Second, the characteristics of the MC73110 motor control IC will be explained.

Principle of Operation of the PMBDCM Drive

The PMBDCM is an electronically commutating permanent magnet motor. The applications of this motor are growing. Because of its inherent variable-speed drive nature, it is widely used in white goods, automobile, and machine-building industries. The commutation circuit for the three-phase PMBDCM can be implemented with discrete components or dedicated control IC. The design with discrete components provides many insights on the commutation circuit for students; at the same time, it requires lots of time and effort to build the hardware and to troubleshoot. The dedicated IC approach looks promising because little or no additional circuitry is required. Some manufacturers even offer dedicated setup software to use their IC.

The mechanical structure of the PMBDCM is the reverse of the conventional permanent magnet brushed dc motor (PMDCM); the rotor contains permanent magnets, and the motor windings are mounted on the stator [7]. The PMBDCM does not have brushes that are required for commutation of the PMDCM. Therefore, a maintenance-free motor drive system is possible with the PMBDCM.

To drive the PMBDCM, an electronic commutation circuit is required. This paper is concerned only with the position sensor-based commutation; therefore, the two common position-sensing techniques are discussed. The first one is the Hall effect sensor, which is the most cost-effective method of rotor position sensing. The timing diagrams of three typical Hall sensors with 120° angle separation are shown in Figure 1. The experimental waveforms of the three Hall signals in both clockwise (CW) and counterclockwise (CCW) directions of motor rotation are shown in Figures 2(a) and 2(b). The direction of rotation is viewed at the motor shaft. The sequences of the Hall signals are Hall A-Hall B-Hall C in the CW direction and Hall B-Hall C-Hall A in the CCW direction.

The second method uses the optical encoder. The incremental encoder is widely used due to its lower cost than the absolute type. However, the optical encoder provides better

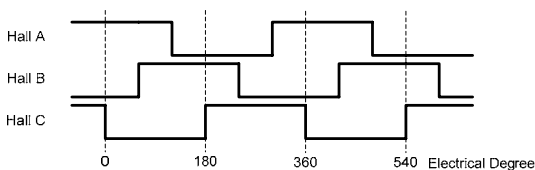


Figure 1. Three-phase Hall sensor timing chart with 120° angle separation

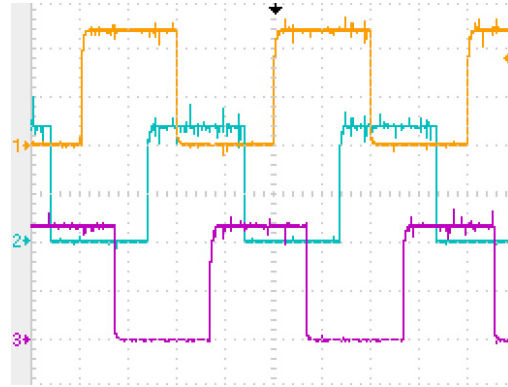


Figure 2(a). Measured Hall signals in CW direction at 1500r/min (CH1: Hall A, CH2: Hall B, CH3: Hall C) (Vertical: 2V/div, Time: 5ms/div)

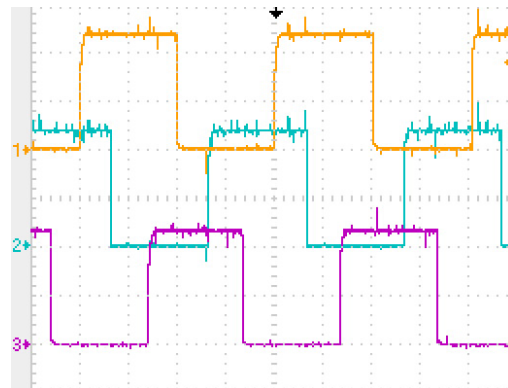


Figure 2(b). Measured Hall signals in CCW direction at 1500r/min (CH1: Hall A, CH2: Hall B, CH3: Hall C) (Vertical: 2V/div, Time: 5ms/div)

resolution of position data than the Hall sensor, therefore making precise control of the PMBDCM possible.

There are two types of permanent magnet brushless dc motors, which depend on their back- electromotive force (EMF) waveforms [7]. The PMBDCM has the trapezoidal (six-step) back-EMF waveform. The one with the sinusoidal back-EMF is called the permanent magnet synchronous motor (PMSM). The PMSM provides nearly zero torque ripples. In this paper, only the PMBDCM with Hall sensor-based commutation will be discussed.

A simplified three-phase full-bridge power circuit for the PMBDCM is shown in Figure 3. The relationships between the three-phase back-EMF, motor current, and air-gap power are shown in Figure 4 [7]. The trapezoidal back-EMF (e_a , b , and c) has a constant magnitude of E_p during 120 electrical degrees in both the positive and negative half-cycle. The air-gap power (P_a) and the electromagnetic torque are both continuous when applying motor current (i_a , b , and c) during the same period in both half-cycles as shown in Figure 4. The

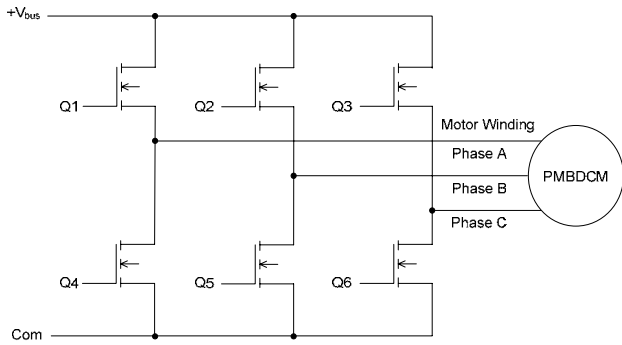


Figure 3. Three-phase full-bridge power circuit for PMBDCM drive

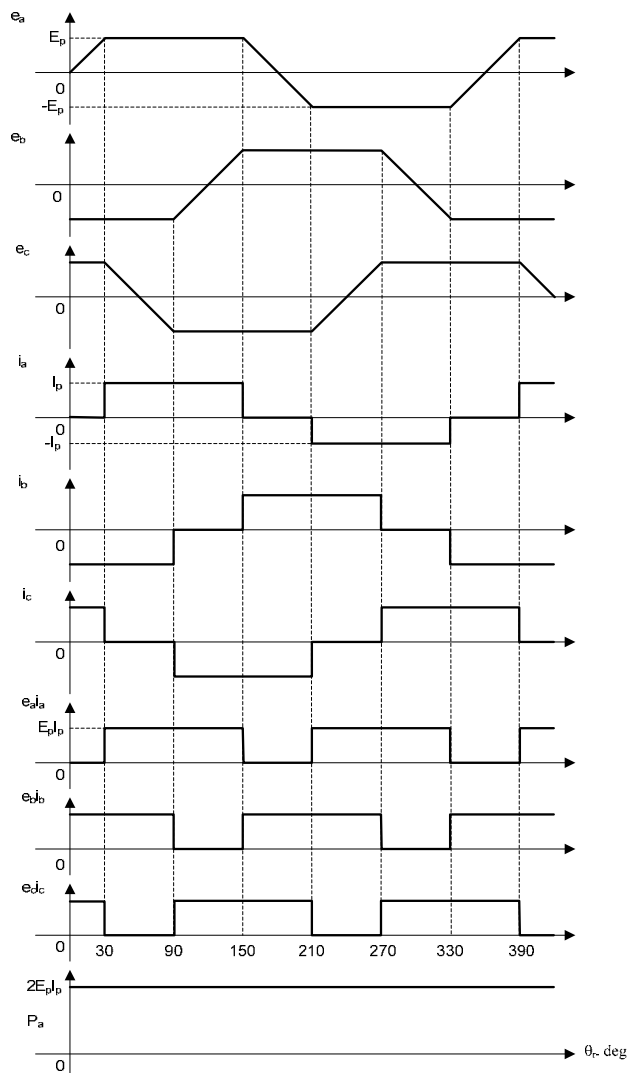


Figure 4. Relationship between back-EMF, motor current, and air-gap power for three-phase PMBDCM drive

Hall signals provide position information of the flat-top portions of the back-EMF in both half-cycles. Based on the position information, it can be seen that the pulse width modulated motor voltage; hence, the motor current is applied to generate the motor torque.

Introduction of the MC73110 Motor Control IC

For the fast-changing motor drive technology in industry, the provision of a new motor control IC was beneficial in developing a digital servo controller without time-consuming effort spent on control software development. The MC73110 motor control IC has developed into an advanced single-chip, single-axis device that can be used to implement an intelligent three-phase PMBDCM controller based on FPGA and ASIC technologies [3, 4]. It is packaged in a 64-pin thin quad flat pack (TQFP) measuring 12 mm by 12 mm and operates on 3.3V. It can be operated in internal velocity profile mode, velocity mode with an external analog, digital velocity command signal, or torque mode with an external torque command signal. It also can be operated as a standalone controller using pre-programmed parameters stored onto chip flash memory or through the RS-232 serial port using the Pro-Motion GUI setup software. The simplified functional block diagram of the MC73110 is shown in Figure 5.

The various functions useful for the development of the PMBDCM drive are embedded in the MC73110 IC. These functions include the three-phase PWM generation for three-

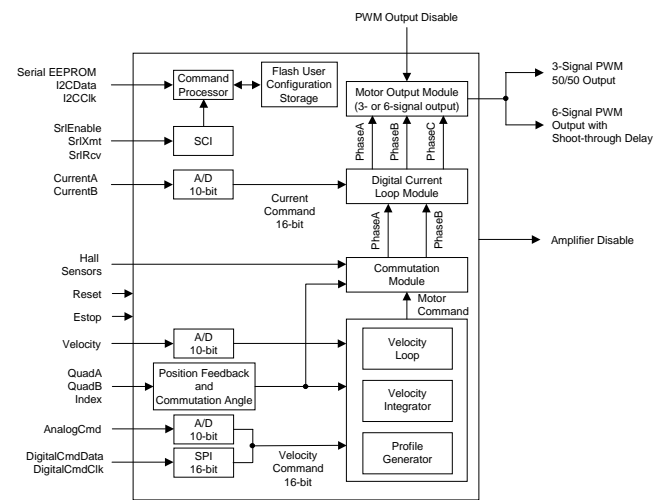


Figure 5. Simplified functional block diagram of MC73110 motor control IC

phase full-bridge power circuit and three-signal PWM for single switch per phase power circuit configuration, Hall- or quadrature encoder-based commutation, digital current and velocity loops, profile generation, emergency stop, analog velocity command, and RS-232 serial communication port, for example. Both the six-step and sinusoidal commutation methods are possible with this IC. But a quadrature encoder is required in addition to the Hall-effect sensors to implement the sinusoidal drive.

The details of the six main functional modules in the MC73110 IC are listed below [3]:

Profile Generator Module: This module generates a velocity- and acceleration-bounded profile by using the serial port commands. The instantaneous desired velocity value is put out to either the velocity integrator or the velocity loop module. A host processor (microprocessor or personal computer) is needed to utilize this module.

Velocity Integrator Module: A desired velocity value from the profile generator module, or an external analog signal (AnalogCmd), or a synchronous serial digital 16-bit word data stream, serial peripheral interface (SPI) bus, will be applied to this module. This value integrates into an instantaneous desired position, which is compared with the actual position from the encoder, to develop either desired velocity or torque.

Velocity Loop Module: Next, a desired velocity command emerges into this module. The velocity command with the current instantaneous velocity of the motor axis will be combined to determine a desired torque or voltage command in this module. The desired velocity command will be generated from the profile generator module, the velocity integrator module, the AnalogCmd, or the digital SPI data stream. The instantaneous velocity emerges from an analog signal through either the velocity pin of the chip or the quadrature encoder. The velocity estimator provides velocity feedback to the digital PI velocity loop from the encoder or Hall feedback. Users can disable this module easily with Pro-Motion GUI. In this case, the MC73110 operates in either torque or voltage mode, depending on the state of the current control module.

Commutator Module: A single-phase desired torque or voltage command will be applied to this module depending on whether the Current Loop Module explained below is enabled, and this command will be vectorized into three-phase commands-one for each motor phase connection. This module supports two commutation methods: Hall-based and sinusoidal. The Hall signals, when Hall-based is selected, must be connected through Hall1, Hall2 and Hall3 pins. When the sinusoidal commutation is selected, the quadrature encoder data must be connected through the QuadA, QuadB,

and Index pins in addition to the Hall signals. This module will remain enabled at all times.

Current Loop Module: The target current for two motor phase coils (PhaseA and PhaseB) will be applied to this module. It uses two sensed analog feedback signals, CurrentA and CurrentB, to develop three PWM output values for a three-phase PMBDCM. When the MC73110 operates the motor in the voltage mode, this module can be disabled.

Motor Output Module: The desired voltage for each of the three motor phase coils will be applied to this module. Then it generates the PWM signal in either three-signal mode (one signal per phase) or six-signal mode (high-side and low-side signals for each phase leg). The generated PWM output signals are symmetric waveforms; they are synchronized to the master PWM output switching frequency at 20kHz.

The MC73110 can be configured as different types of amplifiers, as summarized in Table 1. Most applications may fall under one of the three standard configurations explained below:

Table 1. Three different operation modes of MC73110

Operation Mode	Modules Encoded	Minimal Connections
Torque	Current Loop	Hall A, B, and C CurrentA/B QuadA/B (sinusoidal commutation only) DigitalCmdClk/Data or AnalogCmd
Velocity	Current Loop, Velocity Loop	Hall A, B, and C CurrentA/B QuadA/B (sinusoidal commutation only) or Tachometer DigitalCmdClk/Data or AnalogCmd
Intelligent Motion Controller	Current Loop, Velocity Integrator, Profile Generator	Hall A, B, and C CurrentA/B QuadA/B SrlXmt/Rcv

Torque Amplifier: The torque command will be either an analog signal or an SPI digital data stream. The typical target application of this mode may be the position servo with external position loop and position feedback. The position feedback signal can be analog with analog feedback devices or digital with a microprocessor. One example of the position feedback is the potentiometer, which provides continuously varying voltage that is proportional to the rotor position. The torque amplifier can be a standalone or can employ

a host processor. The MC73110 motor control IC has a 20 kHz digital current loop. The two motor current feedback signals (CurrentA/B) are required to close the current loop.

Velocity Amplifier: This amplifier can be another stand-alone application with the velocity loop enabled. The MC73110 has an internal digital velocity loop with a rate frequency of 10 kHz. The velocity command signal will be the same as for the torque amplifier; the difference is that the command signal represents velocity rather than torque in the torque amplifier. The Hall signal or the encoder or the tachogenerator can be used as the velocity feedback.

Intelligent Motion Controller: This configuration needs a host processor or computer to generate a command signal through the profile generator. In this case the MC73110 works as an intelligent programmable motion controller. The command signal will be applied through the RS-232 serial port.

Design Example of a Digital Velocity Servo Amplifier

To prove the capability of the MC73110, a digital velocity servo amplifier was designed. The experimental results will be discussed in this section. The major benefit of the servo amplifier design, used with the MC73110, is the flexibility of control loop configurations and the setup of its parameter values. The previously mentioned amplifier types can be software configurable by using the interactive Windows-based Pro-Motion GUI software. Since this software is royalty-free, the development of any industrial applications with MC73110 can be cost-effective.

The simplified overall block diagram of the proposed velocity servo amplifier is shown in Figure 6. In this example, the explanation of hardware connections will be omitted. Rather, the focus will be on the verification of software setup. After completion of hardware setup and successful connection between the host PC and the MC73110, the MC73110 developer’s kit will be activated, first by invoking Axis Setup Wizard on the Pro-Motion window [4].

The first page of the wizard is the signal output setting window, as shown in Figure 7. The PWM output mode can be either three-signal mode for a three-phase half-bridge power circuit or six-signal mode for a three-phase full-bridge circuit. The PWM dead time will activate only with six-signal mode to prevent a possible shoot-through fault in the phase leg. It can be set to range from 0 to 12µs.

The PWM limit allows enough off-time for charging the bootstrap capacitor in the bootstrap power supply for a high-side switch. The PWM output logic can be checked for the polarity inversion of the gate drive logic signals. The signal-sensing window provides the necessary inversion of the polarity of feedback signals from Hall sensors and/or an encoder. During normal operation, black dots in white circles blink, indicating the change of signals through feedback sensors. The default signal sense is set to “active low.”

The commutation setup window is shown in Figure 8(a). The commutation mode can be trapezoidal with Hall sensor feedback or sinusoidal with encoder feedback. The sinusoidal commutation mode may be effective with a PMSM to generate near-zero torque ripples [7].

The “Open loop start!” button can be used to check the phasing of Hall signals and motor windings in open loop mode.

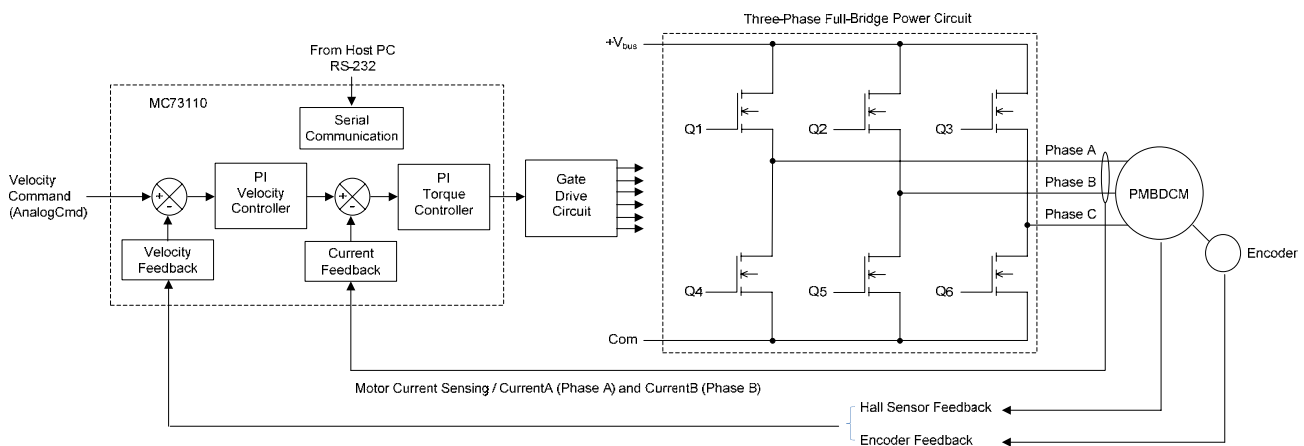


Figure 6. Block diagram of the proposed velocity servo Amplifier

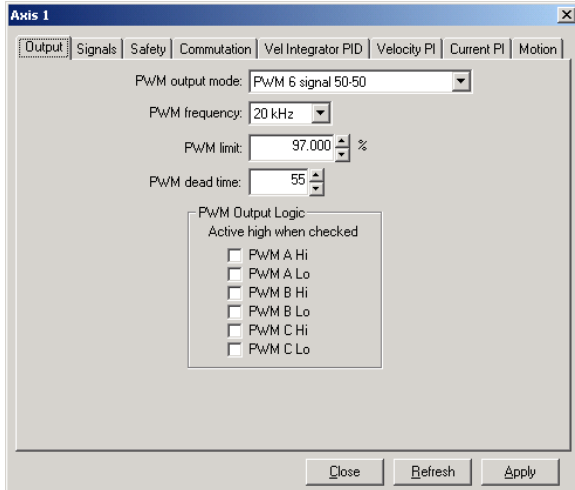


Figure 7. Signal output settings

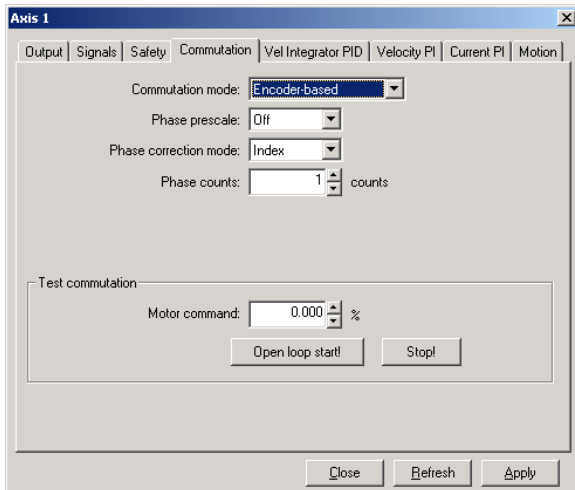


Figure 8(a). Commutation settings

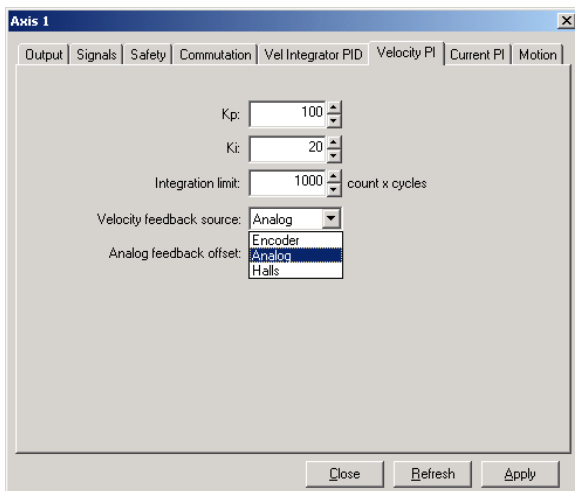


Figure 8(b). Velocity PI settings

	Motor Phase Winding				Hall Effect Sensor			
	PH A	PH B	PH C		S1	S2	S3	
1	A	B	C	}	H1	H2	H3	1
2	A	C	B		H1	H3	H2	2
3	B	A	C		H2	H1	H3	3
4	B	C	A		H2	H3	H1	4
5	C	A	B		H3	H1	H2	5
6	C	B	A		H3	H2	H1	6

Figure 9. Possible combinations of motor windings and Hall signals

When the PMBDCM commutates properly, it gives smooth motion in both CW and CCW directions of rotation. This function is very useful during initial setup of matching Hall signals with relevant motor windings. Without this function, all possible combinations of Hall signals and motor windings should be checked for correct phase matching. The 36 possible combinations are shown in Figure 9. The one combination of each group of motor phase windings and Hall signals should provide an even response for the bipolar command signal.

The setup of velocity loop parameters depends on feedback devices, as shown in Figure 8(b). The allowable velocity feedback sources are analog (tachogenerator), encoder, and Hall signals. The values of PI parameters will be selected by trial and error through the command window. The GetLoopError instruction gives the value of the velocity error. The optimum values of PI parameters can be found by observing the minimal change in the returning velocity error values in either positive or negative polarity. Since the MC73110 does not have the capability of graphical representation of error values, this procedure may be tedious and time-consuming.

The same procedure could be applied to the current loop to find out optimum PI parameter values, as shown in Figure 10(a). The motion window shown in Figure 10(b) provides for the selection of servo loops and motor dynamics. For the standalone application, such as the velocity servo amplifier example in this paper, the velocity command source should be analog. The typical analog velocity command value will be the industry standard $\pm 10V$ dc voltage.

The experimental setup is shown in Figure 11. The velocity command is $\pm 10V$ dc voltage (labeled as Analog Command in front). The communication between the MC73110 and the Pro-Motion software is performed with an RS-232 serial cable. The PMBDCM under testing is the Maxon EC-Max 30, order number 272769. A PMDCM is connected back to back with the PMBDCM to form a motor-generator set. The PMDCM and PMBDCM specifications are listed in Table 2.

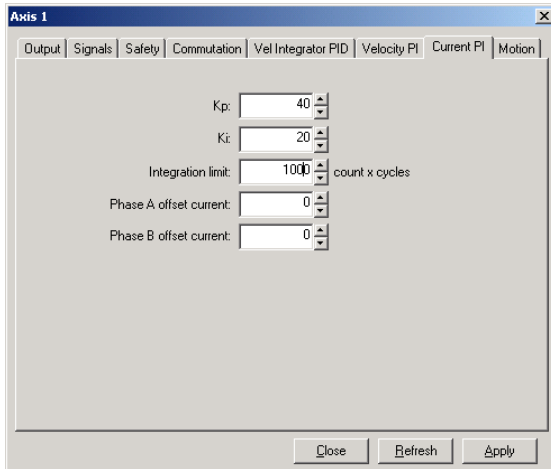


Figure 10(a). Current PI settings

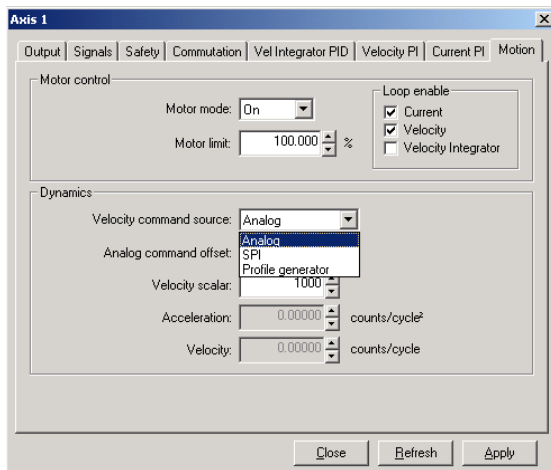


Figure 10(b). Motion settings

The pulse width modulated motor terminal voltage between Phase A and B and Phase A line current is shown in Figure 12. Since the commutation is Hall-based trapezoidal (six-step), the measured current waveform resembles the trapezoidal waveform except in the zero-crossing area and top flat portions in both half-cycles.

Teaching Components with the Proposed Servo Amplifier for the PMBDCM

The proposed digital servo amplifier based on a highly integrated MC73110 motor control IC provides various teaching components to enhance the electric machine control and/or power electronics drive courses. Possible teaching topics and their brief explanations are listed below:

Power Circuit and Gate Drive Circuit: The MC73110 IC

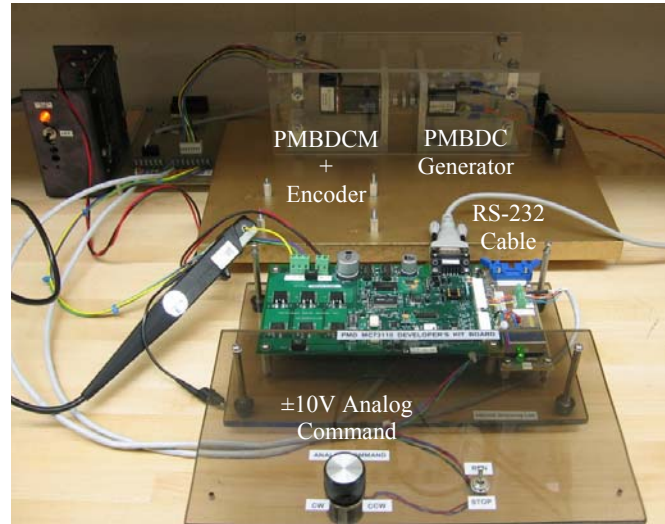


Figure 11. Experimental setup with the MC73110-based PMBDCM drive

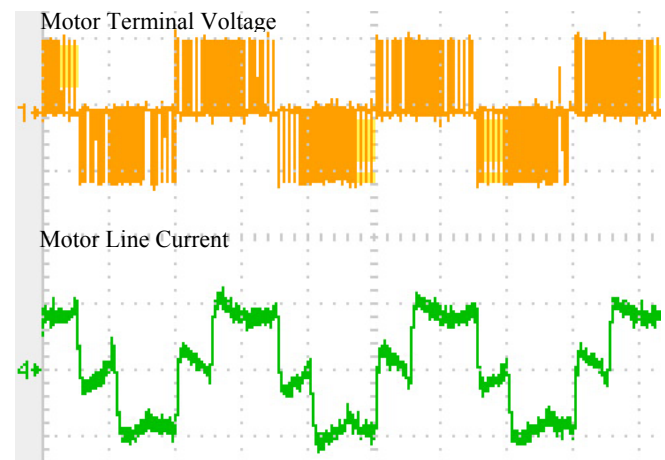


Figure 12. PMBDCM terminal voltage (V_{AB}) and Phase A line current with trapezoidal commutation (Vertical: CH1: 25V/div, CH4: 0.1A/div, Horizontal: 5ms/div)

Table 2. Specifications of the PMBDCM and PMDCM under testing

PMBDCM (Maxon EC-Max 30, 272769)		PMDCM (Moog)	
Nominal Voltage, V	36.0	Nominal Voltage, V	26.0
No Load Speed, r/min	9160	No Load Speed, r/min	10346
No Load Current, mA	73.20	Peak Torque, oz-in	50
Nominal Speed, r/min	7080	Continuous Torque, oz-in	7.5
Nominal Current, mA	97.60	Torque Sensitivity, oz-in/A	3.42
Torque Constant, mNm/A	36.8	Back-EMF, V/rad/s	0.024
Speed Constant, r/min/V	259		
Mechanical Time Constant, ms	6.98		

supports not only conventional three-phase full-bridge power circuits with six power switching devices but also three-phase half-bridge power circuits with three power switching devices. Further, a three-phase half-bridge power circuit can be applied to the switched reluctance motor

(SRM) drive with Hall position feedback sensors. In this case, the motor winding of SRM or PMBDCM is preferably Y-connection with the center point accessible. Usually, the half-wave power circuit produces less output power than the full-wave power circuit [7].

The gate drive for the high-side switching devices requires isolation when an N-type metal-oxide field effect transistor (MOSFET) device is used. By using a P-type MOSFET device, the free of isolation of gate drive is possible.

The various aspects of the types of power switching devices and gate drive selection will be attractive topics to be discussed in detail. The method of the heat-sinking of power switching devices should be addressed with power circuit topologies.

PWM Method: The various PWM strategies to generate PWM gate signals to drive three-phase power circuits can be introduced. Among them, the symmetric three-phase PWM method is implemented in the MC73110 IC.

Back-EMF Types and Commutation Method: Two types of commutation strategy can be introduced: six-step (trapezoidal) and sinusoidal. Six-step commutation can be implemented with Hall position feedback sensors only. It is suitable to the PMBDCM that has trapezoidal back-EMF waveform.

On the other hand, the sinusoidal commutation needs a quadrature encoder in addition to Hall position sensors. This method is applied to the PMSM with sinusoidal back-EMF waveform. But the different effects can be investigated when both commutation methods are applied to the PMBDCM.

Control Loop Closure: The velocity and torque loops are embedded on the MC73110. The basic open-loop and closed-loop control systems can be demonstrated to the class. The observation of effects when closing either or both control loops will be an interesting task for students. Also, the effects of the various proportional (P) and integral (I) gain values in the control loop can be observed through experiment.

Because of the lack of graphical representation capability in Pro-Motion setup software, the continuous monitoring of various control variables is not possible. Instead, as an example, the GetLoopError instruction makes monitoring of discrete velocity and torque loop error values possible. To implement a position servo controller, a position loop can be added externally to the velocity command. It can be realized with few external analog components or with a tiny microcontroller. The velocity loop must be disabled to accommodate an external position loop.

RS-232 Serial Communication: Serial communication is an industry standard means of transmitting and receiving data between a computer and a peripheral device. It is one of the most popular communication methods because the RS-232 serial port is installed on most computers.

It should be noted that the MC73110-based servo amplifier could be configured as a standalone unit. In this case, the necessary control parameters should be downloaded into an on-chip flash memory in the MC73110 IC.

Current Sensing Circuit: To close the current loop, the MC73110 requires two motor phase currents' (phases A and B) information. The phase C current is generated internally by combining those currents. Various current sensing techniques can be discussed: the passive way with a current sensor resistor and Hall sensor based current sensing IC.

The different implementation methods of the analog signal processing circuit need to be discussed along with the current sensing circuitry. The analog signal processing circuit for the current sensor varies widely depending on the current sensing technique.

The following topics are relevant to broaden the coverage further:

IC Packaging Type: Various package types of modern surface mount devices (SMDs) can be introduced to the class. The MC73110 IC is built on a 64-pin TQFP. Some of the IC package types that may be found on the MC73110 development board are small-outline package (SOP), small-outline integrated circuit (SOIC), thin shrink small-outline package (TSSOP), and discrete packaging (D²PAK) for power switching devices.

Protection of the Dc Voltage Polarity Reversal: The required voltage type for the MC73110 development kit is dc. The addition of the protection circuit against the dc polarity reversal is a must for practical application.

Regenerative Braking Circuit: A regenerative braking circuit should be included for the four-quadrant operation of the servo amplifier to dissipate the regenerative energy flows back to the bus when the PMBDCM operates in regeneration mode.

It can be easily implemented with a comparator with the bus voltage sensing circuit, a power-switching device (N-type MOSFET), and a power resistor to dissipate the regenerated energy.

Level Shift Circuit: The MC73110 is powered with 3.3V. Therefore, the various higher input signal levels, such as 5V and 10V, should be converted into 3.3V. A level shift circuit

with an operational amplifier can be addressed as an example of a real-world application of an operational amplifier.

Electromagnetic Interference (EMI) or Radio Frequency Interference (RFI): The EMI/RFI issue directly relates to the clock and PWM frequency in the proposed servo amplifier. The proper management of the printed circuit board (PCB) design is required to minimize the EMI/RFI effect. It is important to address this issue and examine the PCB design. The grounding technique, the use of power and ground planes in multilayer PCB design, and the elimination of ground loop may be worthy topics for discussion.

Conclusion

This paper addresses the feasibility of employing the digital PMBDCM drive in electric machine control and/or power electronics drive courses. The low cost and time-saving way to develop a software-configurable digital servo amplifier for the PMBDCM drive was confirmed with a velocity servo drive example. The MC73110 developer's kit is extremely useful in implementing a software-configurable digital servo amplifier without spending high development costs and time.

The attainable teaching components with the proposed PMBDCM digital servo amplifier are the characteristics of the PMBDCM, the distinction between sinusoidal and trapezoidal drive, and the uniqueness of Hall-sensor and encoder-based commutation methods. The difference between three-phase full- and half-bridge power circuits, the assorted gate drive circuitry, a variety of current sensing methods, the aspects of velocity and current PI controllers, and the various analog signal conditioning methods are also suitable.

References

- [1] Rui Hong Chu, Dylan Dah-Chuan Lu, and S. Sathiakumar, "Project-Based Lab Teaching for Power Electronics and Drives," *IEEE Trans. on Education*, Vol. 51, No. 1, Feb. 2008, pp. 108–113.
- [2] Jon Titus, "Kits Jump Start: Motor Applications," *Design News*, August 13, 2007.
- [3] Performance Motion Devices, Inc., "MC73110 Advanced 3-phase Motor Control IC Product Manual," Revision 1.4, October 2004.
- [4] Performance Motion Devices, Inc., "MC73110 Advanced 3-phase Motor Control IC Developer's Kit Manual," Revision 1.4, August 2005.
- [5] Róbert S. Balog et al., "Modern Laboratory-Based Education for Power Electronics and Electric Machines," *IEEE Trans. on Power Systems*, Vol. 20, No. 2, May 2005, pp. 538–547.

- [6] Joshua M. Williams et al., "Versatile Hardware and Software Tools for Educating Students in Power Electronics," *IEEE Trans. on Education*, Vol. 47, No. 4, Nov. 2004, pp. 436–445.
- [7] R. Krishnan, "Electric Motor Drives: Modeling, Analysis and Control," Prentice Hall, 2001.

Biography

SHIYOUNG LEE is currently an Assistant Professor of Engineering Technology at Pennsylvania State University Berks Campus, Reading, PA. He received the B.S. degree in Electrical Engineering from the Inha University, Incheon, Korea, M.E.E.E. degree from the Stevens Institute of Technology, Hoboken, NJ, and the Ph.D. degree in Electrical Engineering from the Virginia Polytechnic Institute and State University, Blacksburg, VA, respectively. He teaches Programmable Logic Controller (PLC), Electro-Mechanical Project Design, Linear Electronics, and Electric Circuits Laboratory courses. His research interest is digital control of motor drives and power converters. He is a senior member of IEEE and a member of ASEE. Dr. Lee may be reached at sul28@psu.edu.

DESIGN AND TESTING OF A PERMANENT MAGNET AXIAL FLUX WIND POWER GENERATOR

Garrison F. Price, Penn State Altoona; Todd D. Batzel, Penn State Altoona;
Mihai Comanescu, Penn State Altoona; Bruce A. Muller, Penn State Altoona

Abstract

The axial flux permanent magnet (PM) machine is an attractive alternative to radial flux machines in wind turbine applications. The axial flux configuration is amenable to the low-speed, high-torque operation of a direct drive wind energy system. Direct drive wind energy conversion tends to decrease the system size, weight, and noise, while increasing overall efficiency and reliability.

When computing the magnetic field in axial field electric machines for machine design purposes, a 3-D electromagnetic finite element analysis (FEA) is generally required. However, FEA typically requires long computation time, especially for 3-D computations. Therefore, an analytical model of the axial field machine that facilitates expeditious machine design and modeling is desirable. In this paper, the magnetic field distribution in a two-rotor, permanent magnet, ironless stator axial field generator for direct-drive wind energy conversion is studied. The goal is to develop the analytical model for the machine that will facilitate timely design trade-off studies and support an overall electro-mechanical model of wind energy conversion systems.

With the analytic solution for magnetic field strength in the airgap, other quantities of interest may be evaluated, such as back emf, its harmonic content, and, consequently, the machine torque. Thus, it is possible to analyze the entire electro-mechanical system, simulating rotation, quickly calculating magnetic fields, torques, and voltages for specified electrical loading conditions. Based on this approach, an experimental micro-wind generator is constructed. The predicted performance metrics from the analytical model are then compared with experimentally measured quantities to evaluate the effectiveness of the analytical approach.

Introduction

Design of permanent magnet machines, such as the permanent magnet axial flux generator, is a procedure involving iterative computations based on performance requirements and trade-offs. Typically, empirical relations or simplified models are used in the early stages of the design, followed by finite element analysis (FEA) in the later stages. In either case, calculation of the airgap magnetic field is of utmost importance because it is required for the calculation of per-

formance metrics, such as torque constant, torque ripple, back emf constant, and back emf waveshape.

Calculation of the airgap magnetic field using FEA is quite time consuming, especially for an axial flux permanent magnet machine, since 3-D FEA is generally required. As a result, analytical methods to obtain magnetic field solutions have been presented in the literature for permanent magnet synchronous machines of radial flux [1, 2], linear [3, 4], and axial flux configuration [5, 6, 7]. However, solutions proposed for axial flux machines [8, 9, 10] use a mean radius approach, which limits the accuracy of the solution for machines whose relative magnet width or stator coil width is a function of stator radius.

In this paper, the magnetic field distribution in a two-rotor, permanent magnet, ironless stator axial field generator for direct-drive wind energy conversion is studied. The goal is to develop the analytical model for the machine that will facilitate timely design trade-off studies and support an overall electro-mechanical model of an energy conversion system. The model will also consider machine designs where magnet and coil width relative to the pole pitch varies with the machine radius. Analytical results will be validated through a combination of finite element analysis (FEA) and a series of experiments to demonstrate the usefulness of the proposed method.

PM Axial Flux Machines

Axial flux machines are formed by a rotor disc carrying magnets that produce an axial flux and a stator disc containing the phase windings. Many variations in this basic design are possible, including single-sided [11], double-sided [12], torus [13, 14], and multi-disc designs [15]. This paper focuses on the two-rotor, one stator topology, where a single stator is placed between two permanent magnet (PM) rotor discs, as shown in Figure 1. This figure shows a view looking inward radially. Figure 2 shows rotor and stator views looking in the axial direction.

The two disc shaped rotors of Figure 1 carry axially magnetized, surface mounted NDFeB magnets on their inner surfaces. The magnets on opposing rotor discs are arranged so that a North pole on one rotor faces a South pole on the other, resulting in an axial magnetic field so that stator yoke

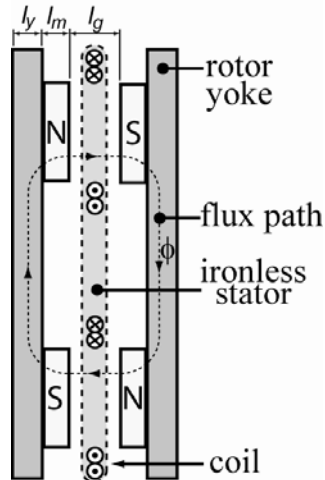


Figure 1. Construction of dual-rotor axial PM generator (looking inward radially)

is not required (stator is required for N-N facing magnets). In the absence of stator iron, three-phase coils are typically potted in a resin. This construction has several advantages over other topologies, such as ease of manufacture, reduced iron losses, and no cogging torque. The double-rotor, single stator axial flux machine also has relatively high moment of inertia, allowing energy to be stored in the rotating machine to help smooth power output during transients.

Axial PM Machine Analytical Model

To analyze the magnetic field in the airgap of the axial PM machine, computations based on the work in reference [6] are applied. However, the analytic model presented in reference [6] assumes the presence of stator iron and that the field intensity in circumferential direction is zero at all iron boundaries (stator and rotor). In the case of the ironless stator studied in this paper, the only two iron boundaries are the rotor yokes. Thus, the equations developed in [6] are modified by applying superposition; that is, the field is determined by summing the fields resulting from the magnets of each rotor side acting individually and the armature reaction field. Although superposition does not apply if saturation occurs, ironless armature machines would not normally be operating in the saturation condition due to the relatively large airgap in such machines.

While previous analytical studies of the axial PM machine have typically used the mean radius to analyze the axial gap machine in 2-D, a more precise method of dividing the machine into radial slices (quasi-3-D) is applied here. Using this approach, the magnetic field is calculated over a range of radii (or slices), assuming no radial component of magnetic field. This assumption is reasonable for a non-saturated operation because an ironless stator machine is not normally

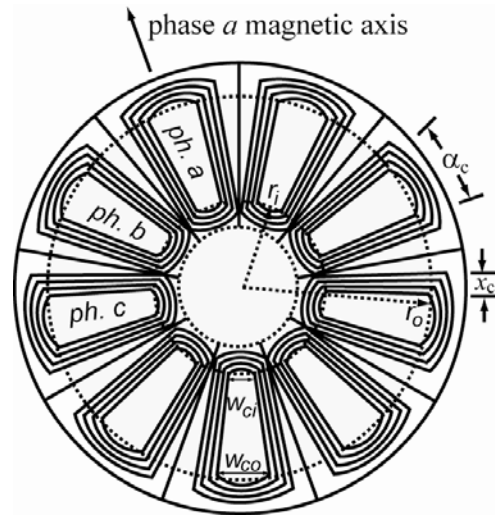
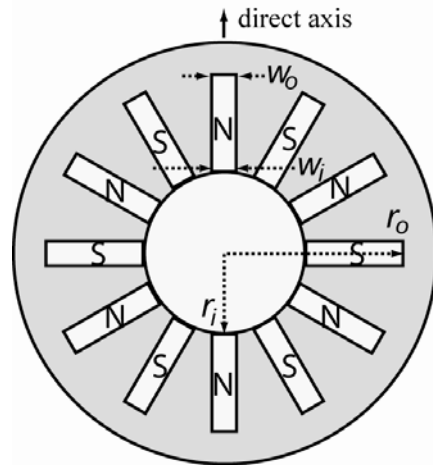


Figure 2. Construction of dual-rotor axial PM generator: rotor (top) and stator (bottom)

operating in a saturated condition. The quasi-3-D approach is expected to improve accuracy as compared with the mean radius approach—especially in cases where the relative magnet width varies with the machine radius.

Magnetic Field Due to Permanent Magnets

In this section, an analytic expression for airgap magnetic flux density is determined using the coordinate system shown in Figure 3, which is a cross-sectional view of the machine looking inward radially. The x and y coordinates in Figure 3 represent the circumferential and axial directions, respectively. Following the analytical method presented in reference [6], with appropriate modifications as described previously, the space harmonic (indicated by subscript n) flux densities at position y due to the magnets on rotors 1 and 2 are found to be, respectively,

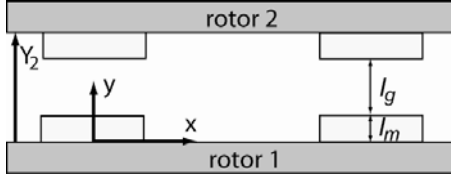


Figure 3. Model and coordinate system for magnetic flux density distribution

$$B_{ym1}(x) = \left(\frac{\hat{J}_n \mu_0 \sinh(u_n l_m)}{u_n \sinh(u_n Y_2)} \cosh(u_n (Y_2 - y)) \right) \cos(u_n x) \quad (1)$$

$$B_{ym2}(x) = \left(\frac{\hat{J}_n \mu_0 \sinh(u_n l_m)}{u_n \sinh(u_n Y_2)} \cosh(u_n (y)) \right) \cos(u_n x) \quad (2)$$

where

$$Y_2 = l_g + 2l_m \quad (3)$$

$$u_n = 2\pi n / \lambda ; \lambda = 2\pi R_m / p . \quad (4)$$

Also, p represents the number of pole pairs, R_m is mean core radius for the radial slice under consideration, and \hat{J}_n is the equivalent current sheet due to magnets 1 or 2. The total flux density for each slice of the machine is determined by the superposition of equation (1) and equation (2). The magnets for each radial slice are modeled as an equivalent current sheet:

$$\hat{J}_n = \frac{4B_r}{\tau_p \mu_0 \mu_{rec}} \sin\left(\frac{n\pi\tau_m}{2\tau_p}\right) \quad (5)$$

where τ_m and τ_p are the magnet and pole pitches, respectively, for the radial slice under consideration. The terms B_r and μ_{rec} are the remanant flux density and permeability, respectively, of the permanent magnet. The total flux densities due to magnets on rotors 1 and 2 for a single radial slice are the sum of space harmonics:

$$B_{y1}(x) = \sum_{n=1} B_{ym1}(x) ; B_{y2}(x) = \sum_{n=1} B_{ym2}(x) . \quad (6)$$

Magnetic Field Due to Armature Reaction

The analytic expression for magnetic field due to armature reaction, not including contributions due to the rotor permanent magnets, will be developed in this section. The model and coordinate system used to develop the analytic expressions is shown in the cross-sectional view of Figure 4. The approach developed in reference [6] is once again applied with modification for the armature reaction analysis. In this case, the armature conductors are represented by a current sheet K , whereas in the previous section, it was the permanent magnets that were modeled as a current density J . Ar-

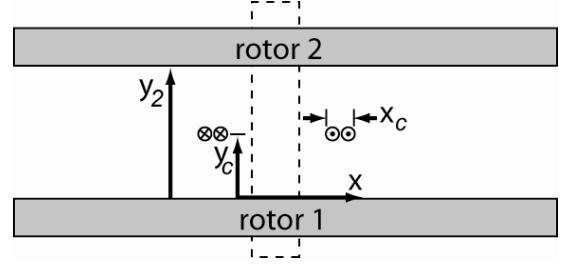


Figure 4. Model and coordinate system for armature (looking inward radially)

mature coils are represented by a current sheet with a peak value \hat{K} located at the mean axial position $y_c = \frac{Y_2}{2}$. The flux density at the mean axial position using Fourier analysis is

$$B_{n-arm}(x) = \hat{K}_n \mu_0 \left(\frac{\cosh(u_n Y_c)}{\sinh(u_n Y_2)} \cosh(u_n (Y_2 - y)) \right) \cos(u_n x), \quad (7)$$

where the linear current density function is

$$K(x) = \sum \hat{K}_n \sin(u_n x). \quad (8)$$

The peak current density is

$$\hat{K}_n = \frac{Ni}{x_c} \frac{4}{n\pi} \sin\left(\frac{n\alpha_c}{2}\right) \sin\left(\frac{nx_c P}{4R_m}\right), \quad (9)$$

where N is the number of turns per coil, i is the current in each individual conductor in the coil; x_c is the coil conductor bundle width in the circumferential direction; and α_c is the average coil span in electrical radians. The Fourier coefficients corresponding to the current sheet density can be plugged directly into equation (7) to calculate the flux density due to the armature conductors.

Note that the coil span may vary with radius for certain types of coil design. For this reason, the armature reaction is evaluated for several radial slices, as described previously, to determine the armature reaction field at various radii. The total flux density due to armature reaction for a single slice is the sum of the space harmonic components:

$$B_{arm}(x) = \sum_{n=1} B_{n-arm}(x). \quad (10)$$

Finally, the net airgap flux density per radial slice can be calculated using superposition by adding the contributions of both magnet sides (equations 1 and 2) with the armature reaction contribution (equation 10).

Computation of Generator Parameters

Once the net field solution is obtained (due to rotor field and armature reaction), other quantities of interest may be evaluated, such as back emf, the machine torque, and torque ripple. With this approach, it is possible to analyze the entire

electro-mechanical system for any specified operating condition and simulating rotation, as well as to quickly calculate magnetic fields, torques, armature currents, and voltages.

To determine the back emf, the flux linking each coil can be determined from the solution for net airgap flux density. The magnetic flux linking a coil in a single radial slice of the machine is a function of the rotor angle θ and can be expressed as

$$\lambda_{slice}(\theta) = N \iint_S B \cdot dS, \quad (11)$$

where S is the surface inside the coil for the radial slice under consideration. Numerically, this is calculated using the cross-sectional area enclosed by the coil slice. The total flux linking the entire coil is then determined by summing the flux linking each radial slice,

$$\lambda_{coil}(\theta) = \sum_1^{slices} \lambda_{slice}(\theta). \quad (12)$$

By carrying out the magnetic field calculations in a time-stepping fashion with a changing rotor angle θ , the flux linking each coil can be determined at each time step. The induced emf in the coil is determined by Faraday's Law:

$$e_{coil}(t) = \frac{\Delta \lambda_{coil}}{\Delta t}. \quad (13)$$

Since a phase winding is comprised of a combination of series or parallel coils whose induced voltages are in phase with one another, the total per phase induced emf e_{phase} is determined by multiplying the coil emf by the total number of series coils per phase:

$$e_{phase}(t) = \sum_1^{series\ coils} e_{coil}(t). \quad (14)$$

The computation of the electromechanical torque developed by the generator may then be determined by using the instantaneous phase voltages and armature currents, where armature currents depend on the electrical loading of the generator:

$$T(t) = \frac{1}{\omega_m} \sum_1^m e_{phase}(t) i_{phase}(t). \quad (15)$$

Here, m is the number of generator phases, and ω_m is the shaft speed (rad./s).

Axial PM Design and Analysis

In this section, the analytical approach described in the preceding section is applied to a representative axial flux wind generator that was constructed and tested in a laboratory setting. The experimental results are compared with those obtained analytically to evaluate the effectiveness of the proposed analytical model. The results may be used to optimize the generator design for its intended application.

The rotor and stator are constructed as shown in Figure 2, with magnet and coil dimensions given in Table 1. This ini-

tial design was chosen because it contains readily available, low-cost components. The dimensions were obtained from a commercially available small-scale wind turbine rated at 750 W for a turbine speed of 600 RPM. This generator design is suited for charging a 12-volt battery system with the rectified generator output voltage at speeds down to 140 RPM. There are nine identical coils with 36 series turns, each with rated current capacity of approximately 10 A rms. Three series coils per phase are arranged, as indicated in Figure 2, and the phases are connected in the Y configuration. The windings are short-pitch, concentrated coils, which are widely used due to ease of construction. As indicated in Figure 2, three armature coils occupy the same circumferential area as four permanent magnet poles. Note also that the airgap length (l_g) is approximately equal to the effective magnet height ($2l_m$) so that the permanent magnet operating point is near the maximum power product [10].

Magnetic Field in Generator at No Load

The analytic magnetic field computations described in equations (1) and (2) are now used to determine the no-load airgap flux density in the experimental machine. As a baseline, these analytic results are compared to magnetic FEA solutions.

Figure 5 shows the flux density determined by the analytical method compared with FEA results for both the innermost slice (smallest radius) and outermost slice (largest radius). From the figure, it is clear that the analytic result closely matches the FEA computation. It should also be noted that the flux density at the outer slice has a more pronounced peak than the inner radius, since the relative magnet width per pole pitch varies with radius. This feature is not captured using the mean radius approach of other analytic solutions.

Table 1. Dimensions of experimental PM generator

Dimension	Value
l_m	.0127 m
l_g	.01905 m
l_y	.00635 m
r_o	.1524 m
r_i	.1016 m
w_o	.0254 m
w_i	.0254 m
w_{ci}	.02032 m
w_{co}	.0254 m

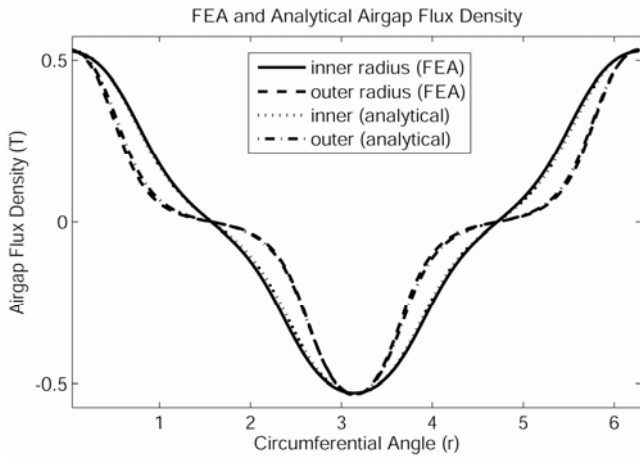


Figure 5. Analytical vs. FEA flux density

In Figure 6, analytically calculated flux density over a magnetic pole pair is mapped versus the axial machine radius. This mapping was generated by calculating the field at 10 discrete radial slices and using those results to form the 2-D result shown in the figure. The figure illustrates the importance of the magnet shape because the peaks shown in the map closely resemble the rectangular magnet dimensions.

The variation of airgap flux density in a single slice versus axial distance from the permanent magnet surface is shown in Figure 7. The first plot compares flux densities at the magnet surface and at the airgap midpoint. The second plot shows a mapping of flux density over a pole pair versus the axial distance from the magnet surface. This mapping demonstrates how the flux spreads near the center of the airgap.

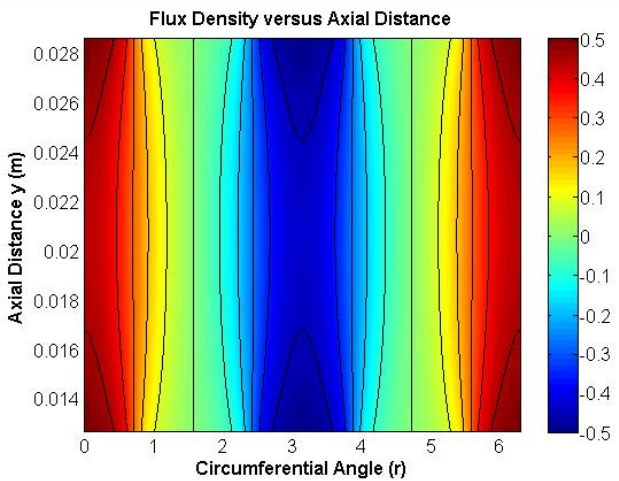
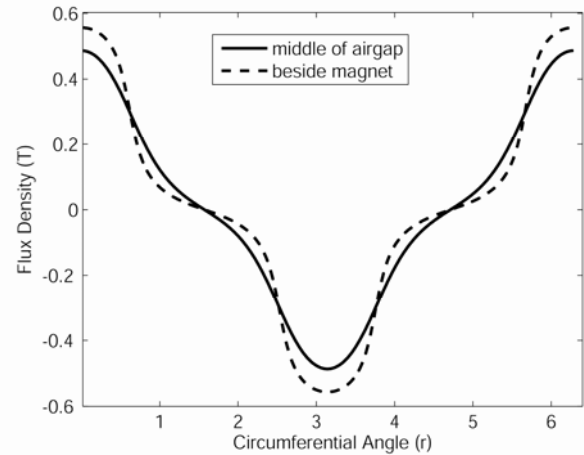


Figure 7. Airgap flux density versus axial position (y)

Magnetic Field in Generator Under Load

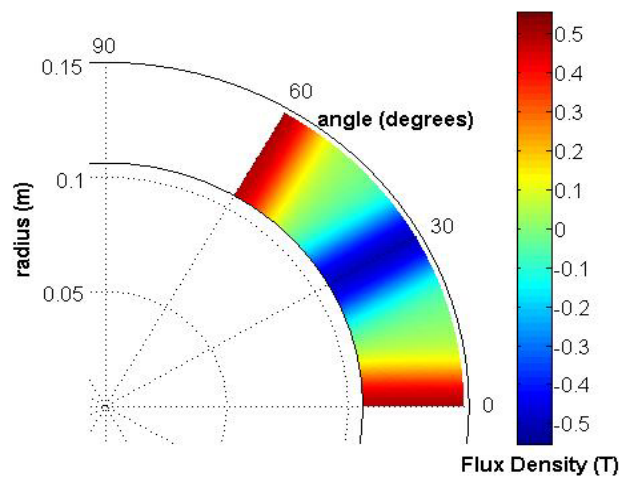


Figure 6. Airgap flux density over one pole pair vs. radius

In this section, the analytic armature reaction magnetic field computation of equation (7) is applied to the experimental machine. To demonstrate the results, analysis is performed at rated maximum current of 10 A rms in the phase a winding and -5 A in the other two phases to satisfy the zero sequence current requirement of a Y-connected armature. The corresponding current sheet for this armature operating condition is shown in Figure 8.

After calculating the Fourier coefficients corresponding to the current sheet, equation (7) is used to find the airgap flux density due to the armature currents. The armature reaction field under the phase a coil for rated current is shown in Figure 9. The figure shows peaks near the edge of the phase band and an average value of .004 Tesla. Comparing Figure 9 with Figure 5, it is clear that the armature reaction field is significantly smaller than the field produced by the permanent magnets. This is a characteristic of the slotless, ironless core machine and was confirmed in [16]. Since the average magnitude of the armature reaction is insignificant compared

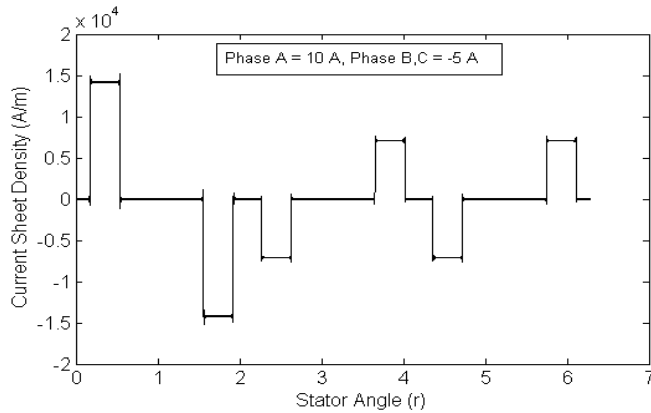


Figure 8. Current sheet density over a stator magnetic cycle

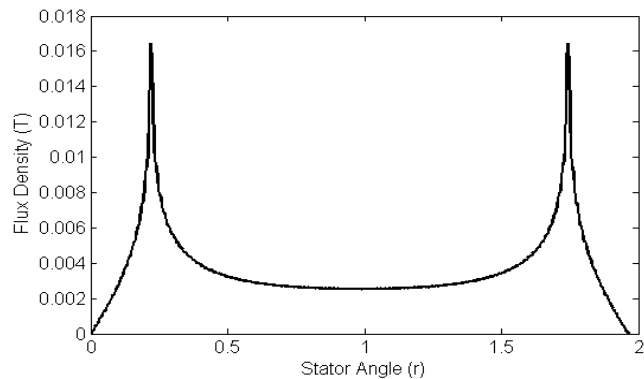


Figure 9. Armature reaction field distribution for rated current in a single phase

to the permanent magnet field, it is reasonable to neglect armature reaction to simplify remaining calculations of machine performance.

Induced Phase Voltage

Given the analytical solutions for airgap flux density, the induced back emf per phase may now be predicted using equation (14). Using the time-stepping approach described previously and a rotational speed of 600 RPM, the airgap fields were calculated for each rotational position. The resulting back emf prediction is shown in Figure 10. In this figure, the trapezoidal coil, whose dimensions are included in Table 1, are compared with a rectangular coil to demonstrate the importance of coil shape in the generator design.

Experimental Results

The analytically predicted values of the generator performance are now verified experimentally. Although the

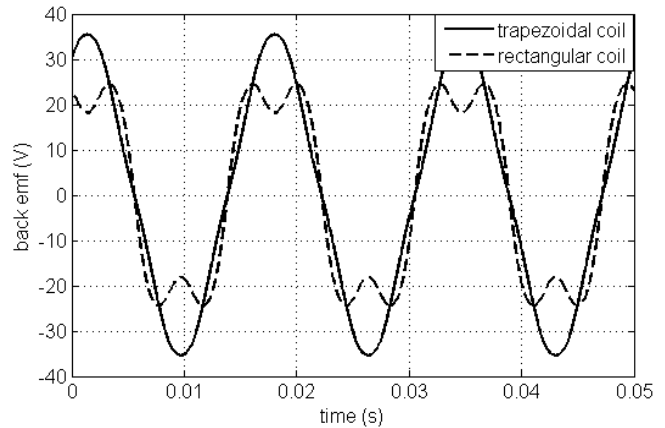


Figure 10. Predicted back emf at 600 RPM for two coil shapes

magnetic field solutions cannot easily be verified experimentally, they have been favorably compared with a magnetic FEA solution. Similarly, torque ripple is not easily measurable. Therefore, the focus here is on comparison of predicted back emf and torque (amplitude and wave shape) with the directly measured values.

To experimentally measure the back emf, the setup shown in Figure 11 is used. The apparatus includes the constructed axial flux generator (at the left) coupled with a prime mover through a belt arrangement. The prime mover is a variable speed DC motor, which is at the far right in the figure. The steady state shaft torque is obtained by the product of prime mover current and torque constant.

With the prime mover rotating the generator shaft at 600 RPM, the no-load per-phase back emf, shown in Figure 12, was obtained. The waveform is sinusoidal with a peak value of 37 volts. This compares favorably with the predicted back emf value of 35.5 volts for the trapezoidal coil (which is



Figure 11. Laboratory setup for wind generator experiments

used in the laboratory experiment) shown in Figure 10. Although not shown here, a second generator that uses a more rectangular coil design was shown experimentally to generate a back emf waveform that closely resembles the predicted voltage shown in Figure 10 for the rectangular coil. This convincing comparison helps to confirm the value of the analytical method.

To verify the analytical prediction that armature reaction effects are negligible, the generator was loaded electrically to rated current at unity power factor and a speed of 500 RPM. Figure 13 shows the comparison between the no-load back emf at 500 RPM and the rated load emf at the same speed. The figure shows no noticeable difference between the voltage waveforms at no-load and rated load (for purpose of display, the dc offset was added to the oscilloscope so that the two waveforms were separated).

The measured average shaft torque at 500 RPM and rated

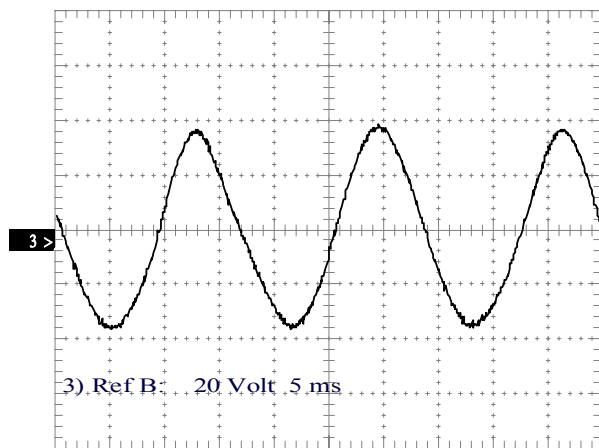


Figure 12. Single-phase back emf at 600 RPM, no load

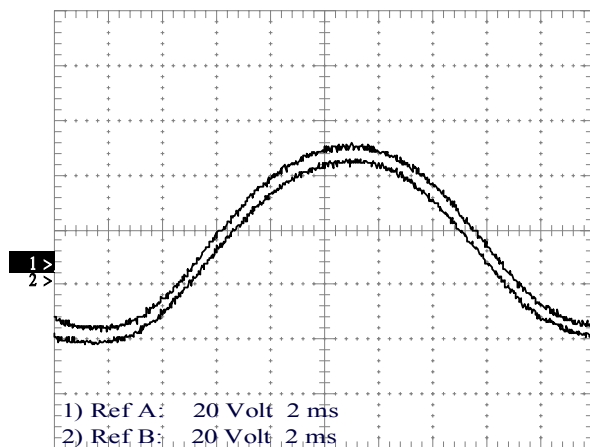


Figure 13. No-load vs. full-load back emf at 500 RPM

load current was 12.6 n-m, which compares favorably with the analytically predicted torque of 12.8 n-m, shown in Figure 14, for the trapezoidal coil design. Note that the predicted torque ripple is rather low (1.1 percent) for the trapezoidal coil design carrying sinusoidal current as used in the laboratory experiments. The torque predictions for the rectangular coil in Figure 14 assume rectangular phase current and yield higher-than-average torque at the expense of increased torque ripple. The actual torque ripple could not be experimentally ascertained.

Conclusion

An analytical approach for the calculation of airgap magnetic fields in an ironless stator axial flux permanent magnet machine has been developed. The proposed analysis is carried out using radial slices, rather than a mean radius approach, so that increased accuracy is possible for machines whose relative magnet or coil width varies with radius. From the magnetic field solutions, which are validated by comparison with FEA results, techniques for predicting generator performance features such as torque, torque ripple, and back emf waveshape have been developed. The accuracy of the proposed approach is analyzed by comparing analytical predictions with experimentally measured results on an axial flux permanent magnet generator. The predicted emf amplitude and waveshape agrees with the emf measured on the actual generator for several coil shapes. The analytically predicted steady state torque is also consistent with the experimental measurements. The close correlation of predicted generator performance and experimental results suggests that the proposed analytical method is a viable alternative to time-consuming FEA analysis for the early stages of ironless stator PM axial flux machine design.

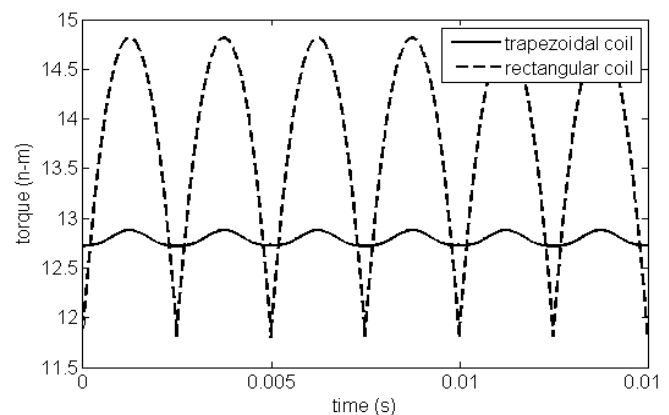


Figure 14. Predicted instantaneous torque at 500 RPM full load for two coil shapes

References

- [1] A. Proca, A. Keyhani, A. El-Antably, W. Lu, and M. Dai, "Analytical model for permanent magnet motors with surface mounted magnets," *IEEE Trans. On Energy Conv.*, vol. 18, no. 3, Sept. 2003, pp. 386–391.
- [2] M. Rosu, A. Arkkio, T. Jokinen, J. Mantere, and J. Westerlund, "Prediction of airgap magnetic field distribution in large output power permanent magnet synchronous motor," *Electromotion '99 - 3rd International Symposium on Advanced Electromechanical Motion Systems*, vol. 1, July 1999, pp. 179–184.
- [3] S. Jung, J. Chun, and H. Jung, "Performance evaluation of slotless permanent magnet linear synchronous motor energized by partially excited primary current," *IEEE Trans. On Magnetics*, vol. 37, no. 5, Sept. 2001, pp. 3757–3761.
- [4] P. Virtic and B. Stumberger, "Analytical analysis of magnetic field and force calculation in a slotless-type permanent magnet linear synchronous machine; verification with numerical analysis," *IEEE International Electric Machines & Drives Conference*, vol. 2, May 2007, pp. 963–968.
- [5] H.P. Furlani, "Computing the field in permanent-magnet axial-field motors," *IEEE Trans. on Magnetics*, vol. 30, no. 5, Sept 1994, pp. 3660–3663.
- [6] J.R. Bumby, R. Martin, M. Mueller, E. Spooner, N. Brown and B.J. Chalmers, "Electromagnetic design of axial-flux permanent magnet machines," *IEEE Proc. on Power Apps.*, vol. 151, n. 2, pp. 151–160, March 2004.
- [7] T.F. Chan and L.L. Lai, "An axial-flux permanent-magnet synchronous generator for a direct-coupled wind-turbine system," *IEEE Trans. on Energy Conv.*, vol. 22, no. 1, March 2007, pp. 86–94.
- [8] Y. Zhang, S. Ho, H. Wong and G. Xie, "Analytical prediction of armature-reaction field in disc-type permanent magnet generators," *IEEE Trans. on Energy Conv.*, vol. 14, no. 4, Dec. 1999, pp. 1385–1390.
- [9] T. Chan, S. Xie and L.L. Lai, "Computation of no-load and armature reaction fields of an axial-flux permanent-magnet synchronous generator," *IEEE International Electric Machines & Drives Conference*, vol. 1, July 2007, pp. 1–6.
- [10] J.F. Gieras, R. Wang, and M.J. Kamper, "Axial flux permanent magnet brushless machines," Kluwer Academic Publishers, 2004.
- [11] D. Patterson and R. Spee, "The design and development of an axial flux permanent magnet brushless DC motor for a wheel drive in a solar powered vehicle," *Proc. IEEE Ind. Apps. Society Conf.*, Denver, 1994, vol. 1, pp. 188–195.
- [12] N. Brown, L. Haydock and J.R. Bumby, "Foresight vehicle: A toroidal, axial flux generator for hybrid IC engine/battery electric vehicle applications." *Proc. SAE Conf. paper 2002-01-089*, Detroit, March 2002.
- [13] E. Spooner and B.J. Chalmers, "TORUS: A slotless, toroidal-stator permanent magnet generator," *IEE Proc. Electr. Power Appl.*, Nov. 1992, pp. 497–506.
- [14] S. Huang, M. Aydin and T.A. Lipo, "TORUS concept machines: pre-prototyping design assessment for two major topologies," *2001 IEEE Industry Apps. Conf.*, vol. 3, no. 30, Sept. 2001, pp. 1619–125.
- [15] R. Kessinger and S. Robinson, "SEMA-based permanent magnet electric motors for high torque, high performance," *Naval Symposium on Electric Machines*, Newport, RI, 1997, pp. 151–155.
- [16] J. Azzouzi, G. Barakat and B. Dayko, "Quasi-3D analytical modeling of the magnetic field of an axial flux permanent-magnet synchronous machine," *IEEE Trans. On Energy Conv.*, vol. 20, no. 4, Dec. 2005, pp. 746–752.

Biographies

GARRISON F. PRICE received a BS in Electro-Mechanical Engineering Technology from Penn State Altoona in 2008. He is presently an electrical engineer at Clipper Windpower, Denver, CO. He can be reached at gprice@clipperwind.com

TODD D. BATZEL received a BS in Electrical Engineering from the Pennsylvania State University in 1984, an MS in Electrical Engineering from the University of Pittsburgh in 1989, and a PhD in Electrical Engineering in 2000 from the Pennsylvania State University. He is currently an Associate Professor of Electrical Engineering at Penn State Altoona. His research interests include machine controls, electric drives, artificial intelligence, and distributed computing. Dr. Batzel may be reached at tdb120@psu.edu

MIHAI COMANESCU received his BSEE from Bucharest Polytechnic University in 1992 and his MS and PhD from the Ohio State University in 2001 and 2005, respectively. He is currently an Assistant Professor of Electrical Engineering at Penn State Altoona.

BRUCE A. MULLER received his BSME from Rutgers University in 1978 and his M. Eng. in Industrial Engineering in 1986 from the Pennsylvania State University. He is currently a senior instructor in Engineering at Penn State Altoona.

A DETERMINISTIC AND STOCHASTIC MODEL FOR PRODUCTION LOT SIZE AS A FUNCTION OF STORAGE COST

Ahmad R. Sarfaraz, California State University, Northridge

Abstract

This paper was motivated by the operational problems of a small manufacturing company for which the original economic production quantity (EPQ) model could not be implemented because of the complexity of estimating the holding cost. Therefore, the paper modifies the original EPQ model based on a situation in which the inventory holding costs are divided into two parts: an inventory carrying charge proportional to the average dollar investment in inventory, and a storage cost proportional to the maximum inventory. Realizing the practical significance of the problem, two models including deterministic and stochastic formulations are presented.

Introduction

Several research papers have been published on inventory control and production planning since Harris presented the well-known economic order quantity (EOQ) formula in 1915. In general, the EOQ model mathematically determines optimal decisions in terms of the order size and frequency based on minimizing costs. Because these decisions are so critical to an organization's success, many manufacturing firms have adapted the Just-In-Time (JIT) inventory methodology. Despite the success of JIT, many companies still use the EOQ model to determine their purchase orders. This is particularly true for small manufacturing firms that cannot effectively implement JIT [1, 2]. As reported by two research papers [3, 4], the EOQ model is still a basic starting point in the development of many inventory models.

As the EOQ model assumes a linear holding cost for units held and a fixed ordering cost each time an order is placed, several papers have modified the model by considering different variations of ordering and holding cost components. With respect to ordering cost components, a number of researchers, including Affisco et al.[5], Nasri and Paknejad [6], Kim et al. [7], Hong et al. [7, 8], and Hong and Hayya [9], revised the EOQ model to better fit JIT manufacturing models. The second cost component of the EOQ model is the holding cost. Given the linear relationship between the holding cost and units held in stock, many other researchers studied and modified the EOQ model to fit various inventory

systems. Among these researchers, Subba and Bahari-Kashani [10] developed a model that employs a fixed cost component and a linear variable cost for the holding cost. Love [11] described piecewise concave storage costs and Brown et al. [12] utilized a non-linear holding cost. Muhlemann and Valtis-Sponopoulos [13] altered the EOQ model with a variable holding cost that is expressed as a percentage of the average value of capital invested in stock. Weiss [14] studied the traditional EOQ model, but with a holding cost as a function of the length of time an item is held in stock. Baker and Urban [15] and Datta and Pal [16] studied a deterministic inventory system with an inventory level-dependent demand rate and with the holding cost held at a constraint rate of per unit time. Goh [17] treated the holding cost as a polynomial function of the length of time spent in holding and as a functional form of the amount of on-hand stock. Thus, it is evident from the literature that different variations in holding costs are estimated more accurately for appropriate applications of the EOQ model.

Importance of Holding Cost Estimation

To calculate the inventory holding cost, manufacturing companies usually take the total cost associated with storing inventory and divide it by the average inventory to determine the inventory carrying charge. Jones [18] stated that most manufacturers ignore some relevant and important costs associated with the holding cost, and thus do not calculate EOQ lot sizes correctly. This is particularly true for small manufacturing firms that cannot effectively implement JIT purchasing [1]. Jones [18] concluded that correct use of the EOQ model results in lot sizes that closely approximate JIT lot sizes. Germain and Dröge [19] also reported that the use of relevant costs associated with the EOQ model could result in determination of the order size and frequency that has a direct and critical impact on any organization's distribution and logistic systems. Despite the importance of estimating the holding cost, it is generally taken to include the capital cost, together with other costs that can be thought of as being proportional to the average value of the inventory. As the present work identifies a proper way to consider the relevant costs, it modifies the EOQ model to fit well the needs of manufacturing and purchasing agencies.

Problem Statement

This paper was motivated by the operational problems faced by a small manufacturing company in the southwestern US in which the original EOQ model could not be implemented owing to the complexity of estimating of the holding cost. The company faces a high inventory of finished goods and also has limited storage space. To overcome the problem of limited space, the company rents out additional space from a neighboring warehouse based on square feet. The management introduced the problem to us in the hope of identifying an economic production quantity (EPQ) for one of their product lines. Despite considering various alternatives for the holding cost, none of them included the situation facing this company. After analyzing the problem, steps were taken to consider the relevant costs associated with the holding cost. Given this new problem, the inventory holding costs were divided into two parts: an inventory carrying charge proportional to the average dollar investment in inventory, and a storage cost proportional to the maximum inventory. It should be noted that the storage cost increases proportionally to the maximum inventory, while the inventory carrying charge increases as the average value of the inventory increases. Because this is a manufacturing company, the EPQ model is more appropriate for this study. Furthermore, the demand for the item in question is uncertain. Therefore, the inventory control problem on which the discussion of an equivalent formulation is based is of a probabilistic continuous-review EPQ model. The results presented here have applications beyond the company in question, because many other small companies may be facing the same problem. Realizing the practical significance of such problems, equivalent EPQ formulations for both deterministic and stochastic cases are presented.

The paper is organized as follows. In the next section, we establish the underlying assumptions and notations used for the modified EPQ model. The following section then presents a mathematical formulation of the problem for both deterministic and probabilistic cases. The objective in both cases is to minimize the total cost function, based on the modified inventory carrying cost.

Assumptions

The model presented here utilizes the assumptions of the basic EPQ model. It is therefore assumed that the manufacturing set-up cost is fixed for each set-up; the holding cost for the inventory item is constant on a per unit basis; the storage cost for the inventory item is constant on a per unit basis; the total carrying cost is linearly related to the average quantity held in inventory; the total storage cost is linearly related to the maximum quantity held in inventory; and the

annual demand and production for the item are known and constant [20]. These assumptions are consistent with those used by Jamal et al. [21] in developing an algorithm to identify the optimal batch sizes for manufacturing and for purchasing raw materials in a JIT environment.

Case 1. Deterministic Formulation

We use the same basic set of total annual cost EOQ that are employed by three papers [10, 22, 23, 24]. The total annual cost (TC) of an item under an EPQ model is the sum of the costs of the actual units manufactured, manufacturing set-up costs, inventory carrying costs, and storage cost:

$$TC = DC + AD/Q + Q(P - D)H/2P + WQ(P - D)/P, \quad (1)$$

where A is the cost of manufacturing set-up, D is the annual demand for the item, Q is the production quantity, H is the annual cost of carrying one unit of inventory in stock, W is the annual storage cost of one unit of inventory in stock, P is the annual production for the item, and C is the manufacturing cost per unit. In Equation (1) the first term is the annual manufacturing cost, the second term is the annual set-up costs, the third term is the annual inventory carrying cost, and the last term is the annual storage cost component. The other cost components, such as safety stock, will be added to Equation (1) when the probabilistic case is considered in the next section.

During a production run, the net addition to inventory is at the rate of $P - D$ per unit time. Note that the average inventory level, $Q(P - D)/2P$, is used to determine the total holding cost and the maximum inventory level, $Q(P - D)/P$, is used to calculate the total storage cost. Whenever the inventory on hand falls below the reorder point r , a new production run of size Q is scheduled. In this model, inventory is built up over time and is depleted and replenished at the same time. This is common practice in many manufacturing firms, whereby a component is produced and consumed simultaneously.

By taking the first derivative with respect to Q of Equation (1) and setting it equal to zero, we can solve the optimum order quantity (Q^*). This results in a total annual minimum cost and optimal production run size:

$$\frac{\delta(TC)}{\delta Q} = 0 = -AD/Q^2 + (P - D)/2P + W(P - D)/P \quad (2)$$

$$Q^* = \sqrt{\frac{2DAP}{(P - D)(H + 2W)}} \quad (3)$$

$$TC = DC + \sqrt{\frac{2DAP(H + 2W)(P - D)}{P}}. \quad (4)$$

Case 2. Probabilistic Formulation

The deterministic model developed in the previous section does not account for risk and uncertainty. An increasing number of situations, as identified by Wemmerlov [25], require lot-sizing studies undertaken in stochastic environments that at least imitate the real world problems. Similar concerns have been expressed by Silver [26] that decision-makers should not necessarily employ a deterministic lot-sizing rule when significant uncertainty exists. Therefore, a more appropriate strategy might be some form of probabilistic modeling that mirrors real world applications. The involvement of uncertainty can be expressed in the form of a probability distribution. When the demand is probabilistic, it is necessary to minimize the expected cost rather than total costs [27]. Depending on whether the random variable is discrete or continuous, there are two approaches to minimize the expected cost. If the random variable is discrete, the expected cost is obtained by adding the different costs for some selected demand level and then selecting the demand level that results in the lowest expected cost. If the random variable is continuous, the minimum expected cost expression is obtained by taking the derivative of the expected cost with respect to the random variable and then setting it equal to zero.

General Stochastic Model Framework

Safety stocks are usually maintained because of inaccurate demand forecasts or suppliers who sometimes fail to deliver goods on time. Thus, safety stocks serve to protect against the risk of these two situations. Either or both of these situations can lead to a stockout, but the level of safety stock for uncertain demand is much higher than for uncertain lead-time. In a study for the Hewlett-Packard Company, Davis [28] reported that 60% of inventory investment is due to demand uncertainty. For a manufacturing company, demand uncertainty is a problem during the production set-up time. It is during this time that demand variations cause stockouts or higher stock levels. Brown and Gerson [29] developed three models for multi-item stochastic inventory systems with budget constraints. They used a sum of expected annual ordering and shortage costs in the objective function, but not the inventory holding cost. Parker [30] determined optimal order quantities when demand is uncertain. Hadley and Whitin [31] presented a continuous inventory model for a single product with stochastic demand and allowable shortages.

The inventory control problem for which discussion of an equivalent formulation is presented in this section is based on the approximation of Hadley and Whitin [31]. It is assumed that the demand in any given interval of time is a

random variable for which a probability distribution can be expressed. Since production set-up is the usual period of concern, attention is focused on the distribution of demand during this time. The production set-up time is denoted by T and is assumed to be constant. Two approaches can be used to determine the safety stock for a system with a fixed production batch size. The first approach deals with known stockout costs, where the unsatisfied demand is backlogged. The second approach deals with unknown stockout costs, where all shortages result in lost sales. The first case is considered in this paper.

Total Annual Expected Cost

Expected values are needed for the formulation of probabilistic models. By utilizing the expected values for the number of shortages and the inventory level, it is possible to derive an approximate expression for the total annual expected cost. The total annual expected cost (TEC) of an item under an EPQ model is the sum of the cost of the actual units manufactured, the manufacturing set-up cost, the inventory carrying cost, the storage cost, and the stockout cost. The following section presents a general formulation for each of TEC components.

Expected Shortage Cost

Let x denote the demand random variable, $f(x)$ denote its probability distribution, and r denote the reorder point. The expected average demand is:

$$\bar{x} = \int_0^{\infty} f(x) dx. \quad (5)$$

A shortage can occur only if demand during the set-up time exceeds the reorder point, that is:

$$E(x > r) = \int_r^{\infty} (x - r) f(x) dx. \quad (6)$$

The expected shortage cost per period will be the shortage cost per unit per period (π) multiplied by the expected number of units per period:

$$E(x > r) = \pi \int_r^{\infty} (x - r) f(x) dx. \quad (7)$$

In an annual period, the number of periods during which a stockout could occur is D/Q , where D is the average annual demand for the item and Q is the production batch size.

Thus, the expected annual shortage cost is:

$$E(x > r) = D\pi/Q \int_r^{\infty} (x - r) f(x) dx. \quad (8)$$

Expected Inventory Holding Cost

Inventory is at a minimum level before a new run is set up and is at a maximum level when the production period is

over. The expected inventory level at the minimum point is simply the expected safety stock, denoted by S . Thus, safety stock is the amount by which the reorder point exceeds the average usage during the production set-up time, that is:

$$S = \int_r^\infty (r-x)f(x)dx = r \int_0^\infty f(x)dx - \int_0^r xf(x)dx = r - \bar{x} \quad (9)$$

The expected inventory level at the maximum point is:

$$\frac{Q(P-D)}{P} + r - \bar{x}, \quad (10)$$

where $Q(P-D)/P$ is the maximum inventory level and $r - \bar{x}$ is the expected safety stock.

To calculate the expected annual holding cost, the expected average inventory is needed. This is accomplished by averaging the inventory at its maximum and minimum levels, that is:

$$\frac{Q(P-D)}{2P} + r - \bar{x}. \quad (11)$$

Thus, the expected annual holding cost is:

$$H \left[\frac{Q(P-D)}{2P} + r - \bar{x} \right], \quad (12)$$

where H is the annual cost of carrying one unit of inventory in stock.

Expected Annual Storage Cost

To formulate the expected annual storage cost, we multiply the maximum expected inventory level by the storage cost per unit per year (W):

$$W \left[\frac{Q(P-D)}{P} + r - \bar{x} \right]. \quad (13)$$

Therefore, the expected total annual system cost will be a summation of the five cost components developed above, which may be expressed as:

$$TEC = DC + \frac{DA}{Q} + H \left[\frac{Q(P-D)}{2P} + r - \bar{x} \right] + W \left[\frac{Q(P-D)}{P} + r - \bar{x} \right] + \frac{\pi D}{Q} \int_r^\infty (x-r)f(x)dx. \quad (14)$$

The major decision here is to determine the size of the production run and the level of the reorder point. To obtain the optimum values for Q and r , we take partial derivatives of the total expected annual cost with respect to Q and r and set them equal to zero.

$$0 = -\frac{DA}{Q^2} + H \left[\frac{(P-D)}{2P} + W \left[\frac{(P-D)}{P} \right] \right] - \frac{\pi D}{Q^2} \int_r^\infty (x-r)f(x)dx \quad (15)$$

$$0 = -\frac{D\pi}{Q} \int_r^\infty (x-r)f(x)dx + H + W \quad (16)$$

$$0 = -\frac{D\pi}{Q} \int_r^\infty (x-r)f(x)dx + H + W. \quad (17)$$

From the first derivative, we obtain the optimal production quantity:

$$Q^* = \sqrt{\frac{2DP[A + \pi \int_r^\infty (x-r)f(x)dx]}{(H + 2W)(P-D)}}. \quad (18)$$

After substituting Equation (6) in the numerator and simplifying, the Q^* is:

$$Q^* = \sqrt{\frac{2DP[A + \pi E(x>r)]}{(H + 2W)(P-D)}}. \quad (19)$$

From the second derivative, we obtain the following optimizing relationship:

$$\int_r^\infty f(x)dx = \frac{Q(H+W)}{\pi D}, \quad (20)$$

where $\int_r^\infty f(x)dx$ is the probability of the stockout. Hence:

$$P(x>r) = \frac{Q(H+W)}{\pi D}. \quad (21)$$

Equation (21) gives the optimum probability of a stockout. It can be applied to both discrete and continuous probability distributions of lead time demand. To obtain the optimum values for the production run size (Q) and the reorder point (r), the following iterative procedure [32] converges to the optimum solution:

- Step 1. Assume the expected number of shortages is zero and then solve for Q in Equation (19).
- Step 2. Use Equation (21) to calculate $P(x>r)$ and r .
- Step 3. Calculate the expected number of shortages using the most recent value of r .
- Step 4. Repeat steps 2 and 3 until convergence occurs for the most recent two successive values of Q^* , unless most computed values of Q are sufficiently close together.

Applying the above procedure is a cumbersome but simple task, and usually convergence is obtained in a few iterations [32]. A simple numerical example can best illustrate the above procedure.

A Numerical Example

To illustrate the results developed in this paper, let us apply the proposed method to solve the following numerical examples. Suppose that an item has the following characteristics. $D=2000$ units/year, $P=10,000$ unit/year, $A=\$200$ /set-up, $H=\$2$ /unit/year, $W=\$2$ /unit/year, $\pi=\$8$ /unit, and demand during the set-up time is shown in Table 1.

To use the procedure outlined above, we first compute Q^* with $E(x>r)=0$.

$$Q^* = \sqrt{\frac{2DPA}{(H + 2W)(P-D)}} = \sqrt{\frac{(2)(2000)(10000)(200)}{(2+2)(10000-2000)}} = 500. \quad (22)$$

Table 1. Lead Time Demand During the Setup Time

Lead Time Demand, x	Probability, P(x)	Probability of Stockout, P(x>r)
148	0.02	0.98
149	0.03	0.95
150	0.06	0.89
151	0.07	0.82
152	0.20	0.62
153	0.24	0.38
154	0.20	0.18
155	0.07	0.11
156	0.06	0.05
157	0.03	0.02
158	0.02	0.00

Knowing the value of Q*, we can use Equation (21) to compute the probability of stockout, P(r>x),

$$P(x > r) = \frac{Q(H + W)}{\pi D} = \frac{(500)(2 + 2)}{(8)(2000)} = 0.125. \quad (23)$$

By consulting Table 1 for P(x>r)=0.125, we observe that the computed value is between 0.11 and 0.05. Selecting the smaller value, a reorder point of 155 will be obtained. The next step is to compute the expected stockout, E(x>r). Given a discrete probability distribution of demand during the setup time, the expected stockout is computed as follows:

$$E(x > r) = \sum_{x=r+1}^{(r)Max} (x - r)P(x) = (156 - 155)(0.06) + (157 - 155)(0.03) + (158 - 155)(0.02) = 0.18. \quad (24)$$

The next step is to recalculate the Q* using the new value of E(x>r) as follows:

$$Q^* = \sqrt{\frac{2DP[A + \pi E(x > r)]}{(H + 2W)(P - D)}} = \sqrt{\frac{(2)(2000)(10000)[200 + (8)(0.18)]}{(2 + 2)(10000 - 2000)}} = 501.8. \quad (25)$$

Having the value of Q*, again we can use Equation (21) to compute the probability of stockout as follow:

$$P(x > r) = \frac{Q(H + W)}{\pi D} = \frac{(502)(2 + 2)}{(8)(2000)} = 0.1255. \quad (26)$$

By using Table 1 for P(x>r)=0.1255, again we observe that the reorder point of 155 will be obtained. Convergence has been obtained, since the reorder point has not changed. Therefore, the optimum production run size is Q*=502 and r=155.

Summary

The EPQ model continues to be a basic starting point in the development of many inventory models. As the present work identifies a proper way to consider the relevant costs, it modifies the EPQ model to fit well the needs of manufacturing and purchasing agencies. It is assumed that the inventory

carrying costs are made up of two parts: an investment charge proportional to the average dollar investment in inventory, and a storage cost proportional to the maximum inventory. Realizing the practical significance of the problem, two models including deterministic and stochastic formulations are presented.

References

- [1] C. Temponi, C., S.Y. Pandya, "Implementation of two JIT elements in small-sized manufacturing firms" *Production and Inventory Management Journal*, Vol. 36, No. 3, 23–30, 1995.
- [2] W. Min, L. S. Pheng, "EOQ, JIT and fixed costs in the ready-mixed concrete industry" *International Journal of Production Economics*, Vol. 102, Iss. 1, 167-172, 2006.
- [3] T. Charabarty, B.C. Giri, K.S. Chaudhuri, "An EOQ model for items with Weibull distribution deterioration, shortages and trended demand: an extension of Philip's model" *Computers & Operations Research*, Vol. 25, No. 7/8, 649–658, 1998.
- [4] R. J. Chaudhuri, K. S. Chaudhuri, "An EOQ model with stock-dependent demand, shortage, inflation, and time discounting" *International Journal of Production Economics*, Vol. 53, No. 2, 171–181, 1997.
- [5] J. Affisco, J., M. Paknejad, F. Nasri, "Quality improvement and setup reduction in the joint economic lot size model" *European Journal of Operational Research*, Vol. 142, No. 3, 497–506, 2002.
- [6] F. Nasri, M.J. Paknejad, "Flexibility improvement in continuous-review (s,Q) systems" *Omega*, Vol. 20, No. 3, 408–420, 1992.
- [7] S. L. Kim, J. C. Hayya, J. D. Hong, "Setup reduction in the economic production quantity model" *Decision Sciences* Vol. 23, No. 2, 500–509, 1992.
- [8] J. D. Hong, J. C. Hayya, S. L. Kim, 1992 "JIT purchasing and setup reduction in an integrated inventory model" *International Journal of Production Research*, Vol. 30, No. 2, 255–266, 1992.
- [9] J. D. Hong, J. C. Hayya, J.C. "Dynamic lot sizing with setup reduction" *Computers & Industrial Engineering*, Vol. 24, No. 2, 209–219, 1993.
- [10] R. S. Subba., H. Bahari-Kashani, "Economic order quantity and storage size-some considerations" *Engineering Costs and Production Economics*, Vol. 19, No. 1–3, 201–205, 1990.
- [11] S. F. Love, "Bounded production and inventory models with piecewise concave costs" *Management Science*, Vol. 20, No. 3, 313–323, 1973.
- [12] R. M. Brown, T. E. Conine, M. Tamarkin, "A note on costs and lot size errors", *Decision Science*, Vol. 17, No. 4, 603–610, 1986.

-
- [13] A. P. Muhlemann., N. P. Valtis-Spanopoulos “A variable holding cost rate EOQ model” *European Journal of Operational Research*, Vol. 4, No. 2, 132-136, 1980.
- [14] H. J. Weiss, “Economic order quantity with nonlinear holding costs” *European Journal of Operational Research*, Vol. 9, No. 1, 56–61, 1982.
- [15] R. Baker, T. Urban T. “A deterministic inventory system with an inventory-level-dependent rate” *The Journal of the Operational Research Society*, Vol. 39, No. 9, 823–832, 1988.
- [16] T. K. Datta, A. K. Pal, “A note on an inventory model with inventory-level-dependent demand rate” *The Journal of the Operational Research Society*, Vol. 4, No. 10, 971–976, 1990.
- [17] M. Goh, “Some results for inventory models having inventory level dependent demand rate” *International Journal of Production Economics*, Vol. 27, No. 2, 155–161, 1992.
- [18] D. J. Jones, D.J. “JIT and EOQ model: odd couple no more” *Management Accounting*, Vol. 72, No. 8, 54–57, 1991.
- [19] R. Germain, C. Dröge., “An empirical study of impact of just-in-time task scope versus just-in-time workflow integration on organizational design” *Decision Sciences*, Vol. 28, 615–636, 1997.
- [20] N. Gaither, *Production and Operations Management*, Duxbury Press.
- [21] A. M. Jamal, M. Sarker, R. Bhaba, “An optimal batch size for a production system operating under a just-in-time delivery system” *International Journal of Production Economics*, Vol. 32, No. 2, 255–261, 1993.
- [22] F. Fazel, “A comparative analysis of inventory costs of JIT and EOQ purchasing” *International Journal of Physical Distribution & Logistics Management*, Vol. 27, No. 8, 496–503, 1997.
- [23] M. Goh., “EOQ models with general demand and holding cost function” *European Journal of Operational Research*, Vol. 73, No. 1, 50–55, 1994.
- [24] H. J. Weiss, “Economic order quantity with nonlinear holding costs” *European Journal of Operational Research*, Vol. 9, No. 1, 56–61, 1982.
- [25] U. Wemmerlov, “The behavior of lot-sizing procedures in the presence of forecast errors” *Journal of Operations Management*, Vol. 8, No. 1, 37-48, 1989.
- [26] E. A. Silver, R. Peterson, *Decision Systems for Inventory Management and Production Planning*, Wiley, New York.
- [27] R. Askin, R., “A procedure for production lot-sizing with probabilistic dynamic demand” *AIIE Transactions* 13, 132–137, 1981.
- [28] T. Davis, “Effective supply chain management” *Sloan Management Review*, Vol. 34, 35–46, 1993.
- [29] R. G. Brown, G. Gerson G., *Decision Rules for Inventory Management*, Rinehart and Winston.
- [30] L. L. Parker, “Economical reorder quantities and reorder points with uncertain demand” *Naval Research Logistics Quarterly*, Vol. 1, No. 4, 351–358, 1964.
- [31] G. Hadley, T. M. Within, *Analysis of Inventory Systems*, Prentice-Hall.
- [32] L.A. Johnson, D.C. Montgomery, *Operations Research in Production Planning, Scheduling, and Inventory Control*, Wiley.

Biography

AHMAD R. SARFARAZ received the B.S. degree in Industrial and Management Science from Tehran, Iran, in 1977, the M.S. degree in MIS from the Middle Tennessee State University, Murfreesboro, TN, in 1980, M.A. degree in Economics from the Middle Tennessee State University, Murfreesboro, TN, in 1981, and the Ph.D. degree in Industrial Engineering from the West Virginia University, Morgantown, WV, 1988, respectively. Currently, he is an associate Professor of Manufacturing Systems Engineering and Management at California state University, Northridge. His teaching and research areas include operations research, AHP, facilities layout and location, and economic analysis. He is director of MSEM Solutions Center and Facilities-VEDC community service learning. Dr. Ahmad R. Sarfaraz may be reached at sarfaraz@csun.edu.

SOFTWARE REVIEW

LOCALIZATION OF TOPOGRAPHIC GPS SURVEYS WITH TOPSURV PC

Reviewed by Tarig Ali and Ali Mehrabian, University of Central Florida

Abstract

Localization (also known as site calibration) is a procedure performed when a topographic survey is carried out with GPS to fit the observed GPS positions to the local datum. Mathematically, site calibration is a coordinate transformation between global and local coordinate systems. Site calibration adjusts the observed GPS ellipsoid elevations to the local vertical datum considering geoid undulations. This procedure uses a set of 3D coordinates of control points in both WGS-84 and the local coordinate system. It can be performed in the field or at the network adjustment stage, depending on the size of project area and the type of the adopted GPS hardware and/or software. The quality of calibration is measured by the maximum values of horizontal and vertical residuals, and it depends on the accuracy of the GPS-derived coordinates of the points. This article presents the general framework of performing site calibration using TopSurv PC, a Topcon ® GPS software that is commonly used with Topcon ® GPS hardware.

Localization with TopSurv

Survey Parameters:

From the TopSurv main menu, select localization under “Survey.” This will bring up the localization wizard screen allowing for adding control points, which are supposed to be known in the two local and global coordinate systems. The localization wizard (Figure 1) allows for adding these points along with the residuals and the survey control parameters, which show the transformation solution type (Fix only; Fix and Float; or Fix, Float, and DGPS), the horizontal and vertical precisions, and the automatic topographic methods (by Time, Horizontal Distance, or Slope Distance).

Adding localization points:

The “Add localization point” allows for adding the coordinate of the control points in local and global coordinate systems. A local/global point can be added through map or file interfaces (Figure 2). The local/global point field contains the coordinates of the point in the local/global coordinate system. Here the name of the control point may be set, and whether the point is to be used for “horizontal or “vertical” localization should be specified. The Epoch Count field

shows the number of the accepted epochs from the GPS data file. The addition of control points for localization is done one by one and as soon as each point is saved, the localization screen will display the newly added point.

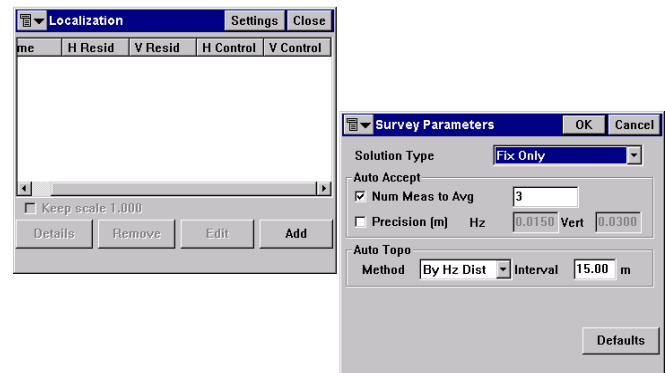


Figure 1. Localization & Survey Parameters wizards

Topo and Auto Topo screens:

The “Topo” screen, which contains four tabs (Topo, Data, Map, Offsets) enables the user to start a static GPS survey (Figure 3). Static GPS survey was the first method of GPS surveying used in the field and it continues to be the primary technique today because of its high accuracy, however it is slow. Relative static positioning involves several stationary receivers’ simultaneously collecting data from at least four satellites during observation sessions that usually last from 30 minutes to 2 hours. A typical application of this method would be the determination of vectors, or baselines as they are called, between several static receivers to accuracies from 1 ppm to 0.1 ppm over tens of kilometers. The determination of the data collection session’s duration depends “mainly” on the length of the baseline and the GPS satellites geometry.

The “Topo” screen contains the preliminary survey data and duplicates the information on the Status screen. The “data” tab contains the station information of the last point recorded since this screen was launched. The “map” tab shows the recorded points graphically and the “offsets” tab allows for setting the offset point for the survey measurement. The offset can be off a “line” or a “point”, which can be completed through the “azimuth-distance-height” screen.

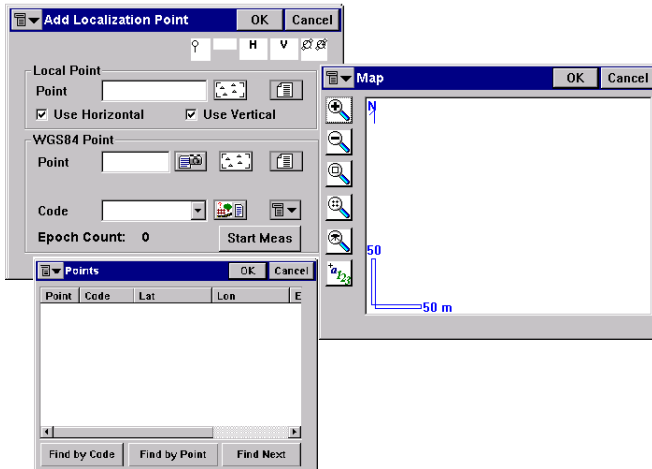


Figure 2. Add localization point wizard and map and file interfaces

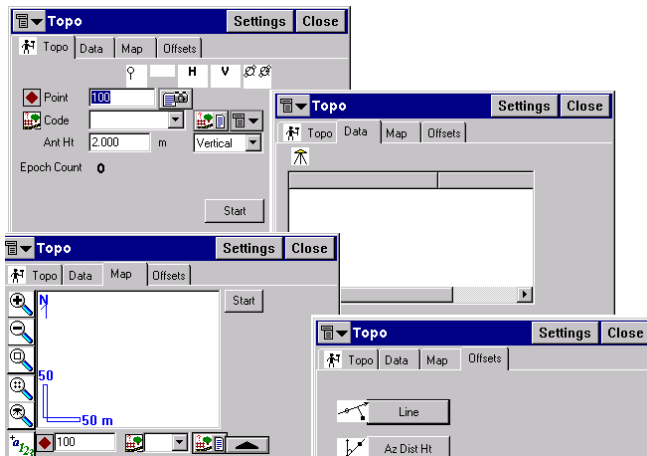


Figure 3. The “Topo” screen and the data, map, and offsets tabs

The “Auto Topo” screen enables for starting a dynamic GPS survey. The term dynamic, widely known as kinematic, is applied to GPS surveys where GPS receivers are in continuous motion. However, for relative positioning the more typical arrangement is a stop-and-go technique, a method that involves the use of at least one stationary reference receiver and at least one rover. This technique is similar to static GPS in that all the receivers observe the same satellites simultaneously, and the reference receivers occupy the same control points throughout the survey. The kinematic method differs from static GPS in the movement of the rovers from point to point across the survey points network. They stop momentarily at each new point, usually very briefly, and their data eventually provide vectors between themselves and the reference receivers.

Like the “Topo,” the “Auto Topo” screen contains four tabs, namely Topo, Data, Map, and Offsets. It enables the user to start a dynamic GPS survey (Figure 4).

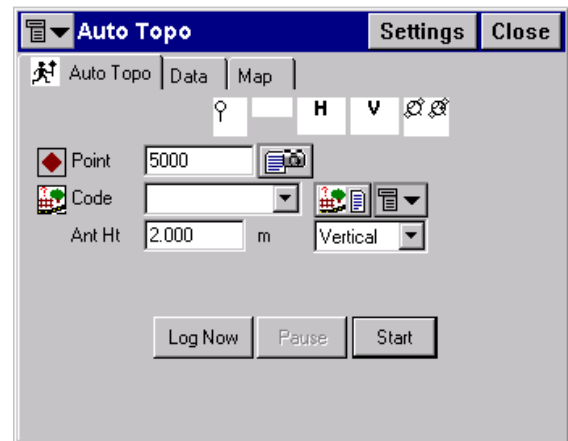


Figure 4. The “Auto Topo” screen

Conclusion and Remarks

The quality of localization is affected by the accuracy and consistency of the GPS coordinates of the control points. The localization computation results are typically examined including the horizontal positioning and the maximum horizontal and vertical residuals. When performing localization especially when vertical site calibration is sought, relying on a published geoid model is not recommended. Instead, connection of the survey with existing control is always encouraged to refine the localization model. GPS software must be able to compensate for (a) the variations in the geoid model and (b) the variations in the established control benchmarks. In order to accomplish this, GPS observations need to be connected between fixed benchmarks (vertical control points). TopSurv PC robustly enables for compensating for both variations mentioned above.

BOOK REVIEW

FUNDAMENTALS OF NANOTECHNOLOGY

GABOR HORNYAK; JOHN MOORE; HARRY TIBBALS; JOYDEEP DUTTA;
CRC PRESS/TAYLOR AND FRANCIS GROUP

Reviewed by Sohail Anwar, Pennsylvania State University, Altoona College

Book Review

This textbook projects nanotechnology as the realization of nanoscience, focusing primarily on applications. The book explores the physical fundamentals of nanomechanics, thin films, nanocomposites, nanoelectronics, and nanomedicine. This book also covers topical areas such as nanometrology, quantum metrology, and its associated standards. This textbook explores a wide range of nanomaterials and describes applications in several industrial sectors such as electronics, optics, magnetism, and nanobiotechnology. The first chapter of this book focuses on the business of nanotechnology.

This textbook features excellent color illustrations, numerous chapter examples, solved equations, and review problems at the end of several chapters. Enough scientific background is presented in order to understand the principles behind the technology.

The textbook is divided into five general divisions:

- 1) Perspectives
- 2) Electromagnetic Nanoengineering
- 3) Mechanical Nanoengineering
- 4) Chemical Nanoengineering
- 5) Biological and Environmental Nanoengineering

The “Perspectives” division comprises two chapters. The first chapter provides essential definitions, discusses the impact of nanotechnology, and presents information regarding commercialization of nanoproducts. The second chapter in this division addresses the nanometrology concepts. The “Electromagnetic Nanoengineering division consists of three chapters that address electronics, optics, and magnetic, respectively. The third division of this book is titled “Mechanical Nanoengineering”. This division addresses the conceptual fundamentals and applications of nanostructures and nanocomposite thin films. The “Chemical Nanoengineering” division comprises two chapters. The first one deals with nanocatalysis and the second one focuses on nanocomposites and fibers. Finally, the “Biological and Environmental Nanoengineering division covers biological, medical, and environmental aspects of nanotechnology. Topics, such as, natural and synthetic biotechnology systems, biometrics,

nanoencapsulated pharmaceuticals, and medical imaging are addressed in the fifth division of this book.

The purpose of this book is to serve as a one-semester generalized text in nanotechnology at the upper undergraduate level. With its unique pedagogical approach and concise treatment of nanomaterials, devices, and components, this textbook provides a complete and integrated introduction to the nanotechnology applications.

INSTRUCTIONS FOR AUTHORS

MANUSCRIPT REQUIREMENTS

THE INTERNATIONAL JOURNAL OF MODERN ENGINEERING is an online publication, specifically for the Engineering, Engineering Technology, and Industrial Technology professionals. Submissions to this journal, such as an article submission, peer-review of submitted documents, requested editing changes, notification of acceptance or rejection, and final publication of the accepted manuscript will be handled electronically.

All manuscripts must be submitted electronically. Manuscripts submitted to the International Journal of Modern Engineering must be prepared in Microsoft Word 98 or higher (.doc) with all pictures, jpg's, gif's, pdf's included in the body of the paper. All communications must be conducted via e-mail to the manuscript editor at fattarzadeh@central.uh.edu and a copy must be sent to the editor at editor@ijme.us

The editorial staff of the International Journal of Modern Engineering reserves the right to format any submitted word document in order to present submissions in an acceptance PDF format in the online journal. All submitted work content will not be changed without express written consent from the author(s).

1. Word Document Page Setup: Top = 1", Bottom = 1", Left=1.25", and Right = 1.25". This is the default setting for Microsoft Word. Do Not Use Headers or Footers
2. Text Justification: Submit all text as "LEFT JUSTIFIED" with No Paragraph Indentation.
3. Page Breaks: No page breaks are to be inserted in your document.
4. Font Style: Use 11-point Times New Roman throughout the paper except where indicated otherwise.
5. Image Resolution: Images should 96 dpi, and not larger than 460 X 345 Pixels.
6. Images: All images should be included in the body of the paper. (.jpg or .gif format preferred)
7. Paper Title: Center at the top with 18-point Times New Roman (Bold).
8. Author and Affiliation: Use 12-point Times New Roman. Leave one blank line between the Title and the "Author and Affiliation" section. List on consecutive lines: the Author's name and the Author's Affiliation. If there are two authors follow the above guidelines by adding one space below the first listed author and repeat the process. If there are more than two authors, add on line below the last listed author and repeat the same procedure. Do not create a table or text box and place the "Author and Affiliation" information horizontally.
9. Body of the Paper: Use 11-point Times New Roman. Leave one blank line between the "Author's Affiliation" section and the body of the paper. Use a one-column format with left justification. Please do not use space between paragraphs and use 0.5 indentation as break between paragraphs.
10. Abstracts: Abstracts are required. Use 11-point Times New Roman Italic. Limit abstracts to 250 words or less.
11. Headings: Headings are not required but can be included. Use 11-point Times New Roman (ALL CAPS AND BOLD). Leave one blank line between the heading and body of the paper.
12. Page Numbering: The pages should not be numbered.
13. Bibliographical Information: Leave one blank line between the body of the paper and the bibliographical information. The referencing preference is to list and number each reference when referring to them in the text (e.g. [2]), type the corresponding reference number inside of bracket [1]. Consider each citation as a separate paragraph, using a standard paragraph break between each citation. Do not use the End-Page Reference utility in Microsoft Word. You must manually place references in the body of the text. Use font size 11 Times New Roman.
14. Tables and Figures: Center all tables with the caption placed one space above the table and centered. Center all figures with the caption placed one space below the figure and centered.
15. Page limit: Submitted article should not be more than 15 page.

College of Engineering, Technology, and Architecture

University of Hartford



For more information please visit us at
www.hartford.edu/ceta

For more information on undergraduate programs please contact Kelly Cofiell at cetainfo@hartford.edu.

For more information on Graduate programs please contact Laurie Grandstrand at grandstran@hartford.edu.

Toll Free: 1-800-766-4024
Fax: 1-800-768-5073



DEGREES OFFERED :

ENGINEERING UNDERGRADUATE

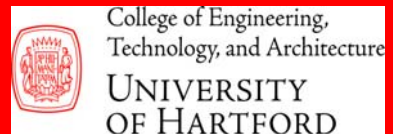
Acoustical Engineering and Music (B.S.E)
Biomedical Engineering (B.S.E)
Civil Engineering (B.S.C.E)
-Environmental Engineering Concentration
Environment Engineering (B.S.E)
Computer Engineering (B.S.Comp.E.)
Electrical Engineering (B.S.E.E.)
Mechanical Engineering (B.S.M.E.)
- Concentrations in Acoustics and
- Concentrations in Manufacturing

TECHNOLOGY UNDERGRADUATE

Architectural Engineering Technology (B.S.)
Audio Engineering Technology (B.S.)
Computer Engineering Technology (B.S.)
Electronic Engineering Technology (B.S.)
-Concentrations in Networking/
Communications and Mechatronics
Mechanical Engineering Technology (B.S.)

GRADUATE

Master of Architecture (M.Arch)
Master of Engineering (M.Eng)
• Civil Engineering
• Electrical Engineering
• Environmental Engineering
• Mechanical Engineering
- Manufacturing Engineering
- Turbomachinery
3+2 Program (Bachelor of Science and
Master of Engineering Degrees)
E²M Program (Master of Engineering and
Master of Business Administration)



IJME NOW SEEKS SPONSORS

**IJME IS NOW THE OFFICAL AND FLAGSHIP JOURNAL OF
INTERNATIONAL ASSOCIATION OF JOURNALS AND CONFERENCE (IAJC)**

WWW.iajc.org



The International Journal of Modern Engineering (IJME) is a highly-selective (acceptance rate of 10-20%), peer-reviewed journal covering topics that appeal to a broad readership of various branches of engineering and related technologies.

IJME is steered by IAJC distinguished board of directors and is supported by an international review board consisting of prominent individuals representing many well-known universities, colleges, and corporations in the United States and abroad.

IJME Contact Information

General questions or inquiry about sponsorship of the journal should be directed to:

Mark Rajai, Ph.D.

Editor-In-Chief

Office: (818) 677-2167

Email: editor@ijme.us

Department of Manufacturing Systems Engineering & Management

California State University-Northridge

1811 Nordhoff St.

Northridge, CA 91330